FLOW-FIELD STRUCTURE

IN

WIDE-ANGLED DIFFUSERS

Karanja Kibicho

Thesis submitted for the degree of
DOCTOR OF PHILOSOPHY
in the Department of Mechanical Engineering
at the
UNIVERSITY OF CAPE TOWN

MAY 2006

Flow-Field Structure in Wide-Angled Two-Dimensional Diffusers

Typeset using PDFLaTeX as implemented in MIKTeX.
Printed in South Africa at:
University of Cape Town,
Private Bag,
7700, Rondebosch.
Cape Town.

To

Wangari

and

Muthoni, Kibicho, Nyawira

Declaration

I declare that the work presented in this thesis is my original work. I also affirm that this work has not been presented in this, or any other university for examination, or for any other purposes.

Signature removed

KARANJA KIBICHO

MAY 2006

Abstract

The difficulties in understanding severely asymmetrical flows in wide-angled diffusers are associated with a lack of sufficient experimental data and accurate flow prediction methods. The results presented in this thesis address this inadequacy. The first objective of this study was to provide a reliable data bank contribution, whereby the complete velocity and static pressure fields, and pressure recovery data for unvaned wide-angled diffusers in the fully stalled flow regime are experimentally measured. The measurements were carried out at Reynolds numbers between 1.07×10^5 and 2.14×10^5 based on inlet hydraulic diameter and centreline velocity for diffusers whose divergence angles were between 30° and 50°. Variation of Reynolds number did not significantly affect the velocity profiles. By increasing the velocity from 10 m/s to 20 m/s, the static pressure recovery increased by 8.31%. However, as the divergence angle was increased, a similar increase in the Reynolds number resulted in a higher percentage increase in pressure recovery.

Due to the adverse pressure gradient along the diffuser walls in wide-angled diffusers, the attached flow separates from one diverging wall and remains attached permanently to the other wall. This process is called 'stalling'. Tests performed to determine the wall to which the flow remained attached led to the conclusion that the wall of preference in both the physical and computational models was totally random. Experimental results showed that regardless of the wall to which the flow was attached, both the velocity

and pressure fields were replicated with discrepancies below 2%.

The second objective of the study was to introduce inlet vanes to the diffuser and investigate the change in the pressure recovery data due to this inclusion. There was a marked improvement in the pressure recovery while operating in this high loss regime of the fully developed stall, with the pressure recovery coefficients increasing by more than 75% in all cases.

The third objective of the study was to numerically model all the physical flows with and without the vanes. Other diffuser geometries whose pressure recovery data are available in the literature were included for comparison. In total, ten diffuser geometries were modeled. Four eddy viscosity models that are known to give reasonable predictions for flows in adverse pressure gradients were used, namely; the standard $k-\epsilon$, realizable $k-\epsilon$, Wilcox $k-\omega$ and Menter shear stress transport (SST) $k-\omega$ models.

In all the four models, computations were performed using the finite volume commercial code, FLUENT. Solution of the modeled equations was carried out using the segregated numerical scheme approach with the governing equations being implicitly linearized. Discretization of the transport equations was done by use of the QUICK discretization scheme. Grid convergence was achieved when the number of cells in the computational domain were 229,440.

All four models showed comparable performance in the prediction of the velocity profiles. The $k-\epsilon$ models however consistently over-predicted wall static pressures by more than 200% and failed to predict the separation bubble that was experimentally observed on the unstalled wall near the diffuser entry. The Wilcox $k-\omega$ model under-predicted the wall static pressure by 14.66%. The SST $k-\omega$ model emerged as the best overall model in predicting these very strong adverse pressure gradient flows.

The maximum error in predicting the static pressure recovery data and velocity fields with the SST $k-\omega$ model was 4%. The lateral velocity and static pressure profiles were predicted within 1% and 0.15% error, respectively. For constant inlet aspect and diffuser length to width ratios, the maximum pressure recovery in unvaned diffuser was predicted to occur when the divergence angle was 11°. The error in predicting the improvement of pressure recovery with the vanes installed was 3.56% when compared with the experimental results.

Finally, a simple correlation for determining the effective flow areas for fully stalled diffusers has been proposed and was found to predict the geometries of those areas to within 6% of those measured experimentally.

Acknowledgement

Every time I think about how far I have come in this research, one question always come to my mind.

What would I have done, without you?

I begin by registering my appreciation for the patience and understanding displayed by my supervisor, Prof. Anthony Sayers from the very beginning of the program *when everything sounded Greek to me.* You have provided me with good guidance and borne the burden of making me understand the philosophy of fluid dynamics experimentation, modeling, and research in general. Thank you for always bringing me back on track whenever I seemed to drift away from my objectives. Thank you for all the research reading materials that you provided and for always being there whenever I needed you.

I am indebted to my sponsors, Universities Science, Humanities, Engineering Partnership in Africa (USHEPiA) for financing the program. Your enthusiasm to sort out all my financial needs and helping me settle in South Africa was great. *Thanks Nan, Carol, Zubaida for the many USHEPiA lunches!* At the Department, I salute Mrs. Clare Bloomer for wonderfully managing the research fund and taking all the trouble of booking my numerous flights.

I am grateful to Dr. Chris Meyer for allowing me to sit in the CFD and Boundary Layer classes. I acknowledge the inspiration you have always given me in the CFD work and answering the many questions I have always had. *At least now I can differentiate between a node and a cell.*

I acknowledge the assistance provided by the Mechanical Engineering Workshop staff, Messrs. Glen, Len and Peter. In particular, I acknowledge all the assistance given to me by Mr. Horst Emrich in fabricating my experimental rig and being available on the spot whenever there was a need to modify the rig. Many thanks also go to Hubert and Julian for helping me with the instrumentation and making the data acquisition possible.

To my wife, Wangari, and my children, Muthoni, Kibicho, and Nyawira, for having allowed me to leave them and stay away for the period of the program. Your encouragement, love, and understanding throughout this period will forever remind me of how important it is to have you in my life. Anthony Mwangi Ngare, I thank you most sincerely for carrying the burden of sorting out the utility bills for my family.

Thanks to Wanjiku wa Mumenya, Kanuthu wa Kaberere, and Wangeci wa Macheru for always being there for me and for the many times you have had to reassure me to have faith in myself and fight on. And lastly, to Stanley for teaching me a bit of Xhosa language. Especially the statement: '*Lixesha lokugoduka!*', (It is time to go back home!).

To the many others who contributed in any way towards the completion of this work, I hereby register my deepest gratitude.

Contents

Dedication iii

Declaration iv

Abstract v

Acknowledgement viii

Contents x

List of figures xiv

List of tables xviii

Notation xix

1 Introduction 1

1.1 Overview 1

1.2 Review of experimental work 6

1.3 Review of numerical work 11

1.3.1 Theoretical modeling of diffuser flows 11

1.3.2 Turbulence models in APG and separated flows 15

1.4 Summary of the review 19

1.5 Strategy and summary of the objectives 20

2 Theoretical Treatment **21**

2.1 Governing equations 21

2.1.1 Navier-Stokes equations 22

2.1.2 Reynolds averaged equations 23

2.1.3 Closure of the RANS equations 24

2.2 Turbulence models 30

2.2.1 Reynolds stress model 31

2.2.2 Standard $k-\epsilon$ model 31

2.2.3 Realizable $k-\epsilon$ model 31

2.2.4 Standard $k-\omega$ model 33

2.2.5 SST $k-\omega$ model 35

2.2.6 Near wall modeling 37

3 Apparatus and Instrumentation **39**

3.1 Fan test facility 39

3.2 The cluster of inlet vanes 48

3.3 Instrumentation 49

3.3.1 Pressure measurements 49

3.3.2 Inlet velocity measurements 55

3.4 Probe steady state calibration 56

3.5 Data acquisition 59

3.5.1 Analogue to digital conversion 59

3.5.2 Data acquisition software 59

4 Numerical Solutions **62**

4.1 Finite volume approach 62

4.2 Numerical treatment 65

4.3 Computational domain 66

4.4 Boundary conditions 70

5 Pressure Coefficients and Uncertainties 71

5.1 Pressure recovery 71

5.2 Statement of uncertainties 74

5.2.1 Instrumentation random errors 74

5.2.2 Experimental random errors 75

6 Results and Discussion 76

6.1 Tunnel qualification 76

6.1.1 Inlet channel flow 76

6.1.2 Reproducibility and replication 81

6.1.3 Reynolds number dependence 86

6.1.4 Two-dimensionality 89

6.2 Data bank contribution 92

6.3 Computational models: Convergence 93

6.3.1 Grid convergence test 94

6.3.2 Discretization scheme 95

6.3.3 Models' comparison 97

6.3.4 Reynolds number independence 101

6.4 Summary: Experiments vs CFD results 102

6.5 Prediction of C_{pr} in unvaned diffusers 104

6.6 Prediction of C_{pr} in vaned diffusers 107

6.7 Prediction of the effective flow geometry 108

7 Conclusions 115

8 Future Outlook 119

References **121**

Appendices **131**

A Data bank contribution **133**

A.1 Wall C_p distribution on both walls 133

A.2 C_p distribution on unstalled wall 135

A.3 Axial velocity profiles 136

A.4 Lateral velocity profiles 137

A.5 Static pressure profiles 138

A.6 Velocity profiles on the normalized scale 139

A.7 Skin friction coefficient, C_{fx} 144

B Calibration of instruments and data acquisition **149**

B.1 Pressure Transducer 149

B.2 Scanivalve 151

B.3 Yaw meter steady state calibration 152

B.4 Constant temperature anemometer 158

B.5 Data acquisition 160

B.6 LabVIEW coding 161

List of Figures

1.1 Flow regimes in two-dimensional diffusers 2
1.2 Relationship between flow regimes and pressure recovery . . . 3

3.1 Line layout of the experimental apparatus 40
3.2 Pictorial view of the experimental apparatus 41
3.3 Entry corner assembly details 42
3.4 Geometry of the diffuser roof and convention for the diffuser . 47
3.5 Notation for the vane design 49
3.6 Facility with vanes installed 50
3.7 The 3-tube yaw meter 52
3.8 Yaw meter orientation mechanism 54
3.9 Flow facility with yaw meters 55
3.10 Data acquisition flow logic 60

4.1 The basic mesh configuration 67
4.2 The optimized mesh configuration 67
4.3 The mesh for the vaned diffuser 69

5.1 Idealized flow in diffusers 72

6.1 Inlet axial velocity profiles in the 50° diffuser 77
6.2 Turbulence intensity at $x/W_1 = -2.35$ for the 30° diffuser . . . 80

6.3 Intermittency of stalling between diffuser diverging walls . . . 81
6.4 Streamline contours for the 50° diffuser 81
6.5 Reproducibility of C_p for the 30° diffuser 83
6.6 Reproducibility of velocity profiles for the 30° diffuser 83
6.7 Replication of velocity profiles for the 30° diffuser 84
6.8 Mirror replication of velocity profiles for the 30° diffuser . . . 84
6.9 Replication of C_p for the 30° diffuser 85
6.10 Influence of Re on C_p for the 30° diffuser 87
6.11 Influence of Re on velocity profiles for the 30° diffuser 88
6.12 Standard deviation of C_p data due to change in Re 88
6.13 Two-dimensionality test for a 30° diffuser 90
6.14 Discrepancies in the velocity profiles between planes 91
6.15 Tuft flow visualization on the side walls 92
6.16 Grid convergence test on velocity profiles 94
6.17 Grid convergence test on C_p 95
6.18 The y^+ values for the 50° diffuser 96
6.19 Discretization scheme convergence for velocity profiles 96
6.20 Discretization scheme convergence for C_p 97
6.21 Performance of eddy viscosity models in predicting C_p 98
6.22 Performance of eddy viscosity models in predicting velocity profiles 99
6.23 Reynolds number dependence test for the velocity profiles . . . 101
6.24 Reynolds number dependence test for C_p 102
6.25 Axial velocity profiles for the 50° diffuser 102
6.26 Pressure recovery coefficient for the 50° diffuser 103
6.27 Lateral velocity profiles for the 50° diffuser 103
6.28 Static pressure coefficient profiles for the 50° diffuser 104

6.29 Coefficient of pressure recovery data 105
6.30 Experimental wall C_p for all angles 106
6.31 Velocity vectors for the 30° and 40° diffusers 106
6.32 Coefficient of pressure recovery data for vaned diffusers 107
6.33 Velocity vectors and contours for the 50° diffuser 109
6.34 Normalized velocity profiles for the 50° diffuser 110
6.35 Reversal points ξ_r for diffusers 111
6.36 Effective flow-field for wide angled diffusers 112
6.37 Separation bubble on the unstalled wall 112
6.38 x-shear stress coefficient for the 50° diffuser 113
6.39 x-shear stress coefficient for the 15° diffuser 114

A.1 Coefficient of static pressure for the 30° diffuser 133
A.2 Coefficient of static pressure for the 40° diffuser 134
A.3 Coefficient of static pressure for the 50° diffuser 134
A.4 Experimental and numerical C_p data for the 30° diffuser . . . 135
A.5 Experimental and numerical C_p data for the 40° diffuser . . . 135
A.6 Axial velocity profiles for the 30° diffuser 136
A.7 Axial velocity profiles for the 40° diffuser 136
A.8 Lateral velocity profiles for the 30° diffuser 137
A.9 Lateral velocity profiles for the 40° diffuser 137
A.10 Static pressure coefficient profiles for the 30° diffuser 138
A.11 Static pressure coefficient profiles for the 40° diffuser 138
A.12 Normalized velocity profiles for the 42° diffuser 139
A.13 Normalized velocity profiles for the 40° diffuser 139
A.14 Normalized velocity profiles for the 30° diffuser 140
A.15 Normalized velocity profiles for the 28° diffuser 140
A.16 Normalized velocity profiles for the 20° diffuser 141

A.17 Normalized velocity profiles for the 15° diffuser 141
A.18 Normalized velocity profiles for the 10° diffuser 142
A.19 Normalized velocity profiles for the 7° diffuser 142
A.20 Normalized velocity profiles for the 4° diffuser 143
A.21 Skin friction coefficient C_{fx} for the 42° diffuser 144
A.22 Skin friction coefficient C_{fx} for the 40° diffuser 144
A.23 Skin friction coefficient C_{fx} for the 30° diffuser 145
A.24 Skin friction coefficient C_{fx} for the 28° diffuser 145
A.25 Skin friction coefficient C_{fx} for the 20° diffuser 146
A.26 Skin friction coefficient C_{fx} for the 15° diffuser 146
A.27 Skin friction coefficient C_{fx} for the 10° diffuser 147
A.28 Skin friction coefficient C_{fx} for the 7° diffuser 147
A.29 Skin friction coefficient C_{fx} for the 4° diffuser 148

B.1 Pressure transducer calibration curve 151
B.2 Yaw angle calibration parameter $f(\psi)$ for $-120° \leq \psi \leq 120°$. 154
B.3 Yaw angle calibration parameter $f(\psi)$ for $-45° \leq \psi \leq 45°$ . . 155
B.4 Yaw angle calibration parameter $f(\psi)$ for $-45° \leq \psi \leq 45°$ . . 156
B.5 Yaw angle calibration parameter $f(\psi)$ for $-45° \leq \psi \leq 45°$ . . 156
B.6 The L-shaped hot-wire probe 159
B.7 CTA linearizer calibration curve 160

List of Tables

1.1 Numerical work on asymmetric diffusers 14

1.2 Numerical work in APG and separated boundary layer flows . 18

3.1 Dimensions for corner assembly side plates 43

3.2 Location of static pressure holes 46

3.3 Dimensions for the vane clusters 48

4.1 Exit Hydraulic diameters and mass flow rates 66

4.2 Specification for the meshes 68

6.1 Non-uniformity, λ (%), of inlet flow with diffuser 77

6.2 Non-uniformity, λ (%), of flow at $x/W_1 = -2.35$ 78

6.3 Diffuser inlet blockage factors and turbulence intensities 79

6.4 Reproducibility and replication of diffuser flows 85

6.5 Performance of turbulence models 100

6.6 Prediction of % errors in diffusers 104

6.7 Mapping of the flow-field 114

B.1 Testing for the accuracy of the yaw meter probe 158

Notation

This section includes the most commonly used notation in this thesis. In order to avoid departing too much from conventions normally used in literature on turbulence modeling and general fluid mechanics, a few symbols denote more than one quantity.

English symbols

A	Local cross-sectional area, m^2
AR	Area Ratio $A_2/A_1 = W_2/W_1$
AS	Aspect ratio b/W_1
b	Distance between parallel walls of the diffuser, m
B	Total blockage factor, the ratio $2\delta^*/W_1$
C_f	Skin-friction coefficient based on freestream velocity
C_p	Coefficient of static pressure recovery at any wall location
C_{pr}	Overall coefficient of static pressure recovery
C^*_{pr}	Maximum coefficient of static pressure recovery for $N/W_1 =$ constant
D	Transport of turbulent properties by diffusion
D_h	Hydraulic diameter, m
E_{lin}	CTA linearizer output, volts
f_β	Vortex stretching function

f_{β^*}	Cross diffusion function
$f(v)$	Yaw meter calibration parameter
F_1, F_2	Turbulence model blending functions
g	Acceleration due to gravity, m/s^2
L	Length of diffuser side plates, m
k	Turbulent kinetic energy, m^2/s^2
k_s^+	Dimensionless roughness constant
N	Diffuser total axial length, m
$\tilde{p}$	Instantaneous pressure, N/m^2
P	Mean static pressure, N/m^2
	Production of turbulent properties,
	Wetted perimeter, m
P_{atm}	Atmospheric pressure, N/m^2
P_D	Dynamic pressure, N/m^2
P_r	Static pressure rise in diffuser, N/m^2
P_t	Total pressure, N/m^2
P_x	Static pressure at any location, N/m^2
q	Flow velocity in an arbitrary direction, m/s
Q	Volumetric flow-rate, m^3/s
Q_p	Yaw meter dynamic pressure calibration parameter
Re	Reynolds number
Re_t	Turbulence Reynolds number
Re_y	Near-Wall turbulence Reynolds number
S	Modulus of the mean rate-of-strain
S_{ij}	Mean strain rate tensor
S_p	Yaw meter total pressure calibration parameter
t	Time, s

u, v, w	Velocities in x, y, z directions, m/s
u'	Root mean square fluctuating velocity in x direction, m/s
u^*	Shear stress velocity, m/s
u^+	Dimensionless near wall velocity
$\tilde{u}_i$	Instantaneous velocity in x_i direction, m/s
U_i	Mean velocity in x_i direction, m/s
U_{ref}	Mean velocity at diffuser reference location in x direction, m/s
V	Volume of a cell, m^3
V_{tra}	Transducer voltage output, volts
x	Axial distance of measurement locations from the diffuser inlet, m
x, y, z	Rectangular cartesian coordinates
y	Normal distance from diffuser wall, m
y^+	Dimensionless distance from the wall
W	Width of the diffuser, m

Greek symbols

α, β	Closure coefficients
γ_s	Intermittency of stalling between diffuser diverging walls, %
δ	Boundary layer thickness, m
δ^*	Boundary layer displacement thickness, m
δ_{ij}	Kronecker delta
ϵ	Turbulent kinetic energy dissipation rate, m^2/s^3
ϵ_{ijk}	Alternating tensor
ξ	Non-dimensional coordinate normal to the axial (x) direction
θ	Half angle of the diffuser between diverging walls, °
	Boundary layer momentum thickness, m

ι	The coordinate of distance measured along diffuser walls
κ	Von Karman universal constant
λ	Measure of inlet flow non-uniformity
μ	Molecular viscosity, kg/ms
μ_t	Turbulent eddy viscosity, kg/ms
Π	Transport of turbulent properties by pressure-strain relationship
ρ	Mass density of the fluid, kg/m^3
σ_k	Turbulent Prandtl numbers for k
σ_ω	Turbulent Prandtl numbers for ω
σ_ϵ	Turbulent Prandtl numbers for ϵ
τ_{ij}	Reynolds shear stress tensor
υ	Kinematic molecular viscosity, m^2/s
υ_t	Kinematic turbulent eddy viscosity, m^2/s
ϕ	Dissipation of turbulent properties
	Arbitrary transport property
χ_k	Dimensionless cross diffusion parameter
χ_ω	Dimensionless vortex stretching parameter
ψ	Velocity vector angle, $^\circ$
ω	Specific dissipation rate, s^{-1}
ω^+	Normalized specific dissipation rate
Ω_{ij}	Mean rate-of-rotation tensor, s^{-1}

Abbreviations

AFOSR	Air Force Office of Scientific Research
AMG	Algebraic multigrid method
APG	Adverse pressure gradient
CAD	Computer aided design

CFD	Computational fluid dynamics
CTA	Constant temperature anemometer
DAQ	Data acquisition
DNS	Direct numerical simulations
ERCOFTAC	European research community on flow, turbulence and combustion
HTTM	Heat Transfer and Turbulence Mechanics
LES	Large eddy simulations
PCI	Peripheral component interconnect
QUICK	Quadratic upstream interpolation for convective kinetics
RANS	Reynolds averaged Navier-Stokes equations
RSM	Reynolds stress model
SIMPLEC	Semi-implicit method for pressure linked equations-consistent
SST	Shear stress transport model
UIM	Unified integral method

Others

∂	Partial derivative
D/Dt	Total derivative
ℓ	Length scale of turbulence
∇	Gradient
Γ	Diffusion coefficient

Subscripts/superscripts

e	Equivalent
f	Face of a cell
k	Transport terms of turbulent kinetic energy
l, r, c	Left, right, center
m	Mean, average
n	Normal, perpendicular
nb	Neighboring cells
t	Total
w	Conditions at the wall
ϵ	Transport terms of turbulent kinetic energy dissipation rate
τ_{ij}	Transport terms of Reynolds stresses
ω	Transport terms of turbulent kinetic energy specific dissipation rate
1	Diffuser entrance
2	Diffuser exit

Convention and frame of reference

The notation and the frame of reference for the two-dimensional diffusers in this research are based on the figure below.

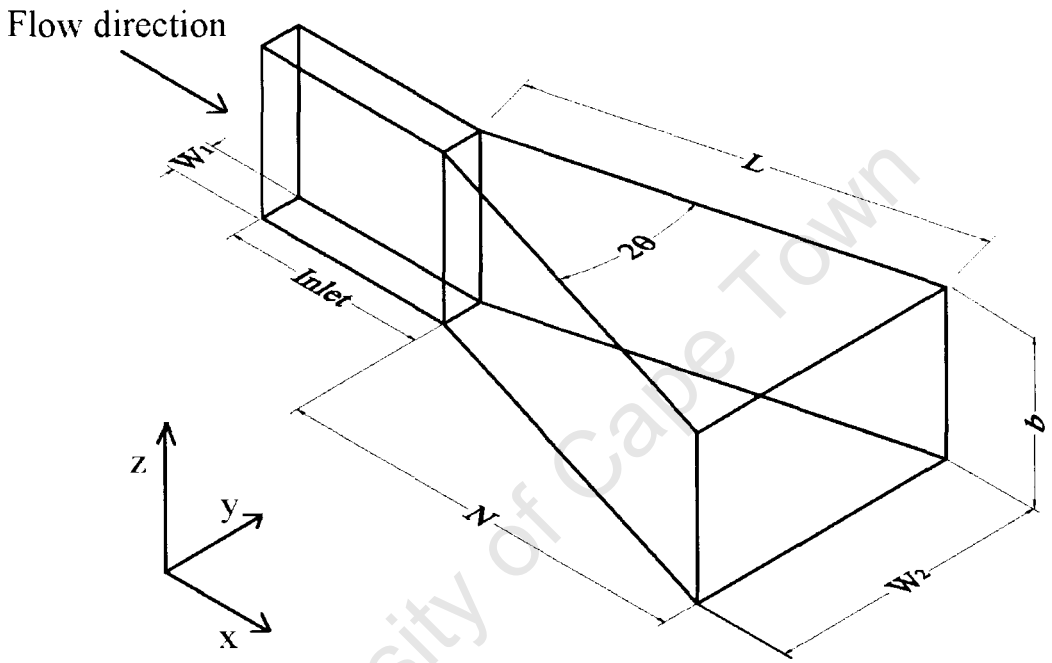

Chapter 1

Introduction

1.1 Overview

Diffusers are found in many fluid-flow systems, such as turbo machines, flow meters, noise suppressors, air-conditioning ducting, wind tunnels, etc. While the improvement of pressure recovery in a diffuser without regard to dimensional limitations is obviously desirable, the most welcome improvement from a designer's viewpoint would be the reduction of a diffuser's length without sacrificing its performance. In order to meet some design constraints such as the overall size of a fluid-flow system, wide-angled diffusers with severe flow separation and poor efficiency, are often tolerated. The flow separation is caused mainly by the adverse pressure gradient along the walls of the diffuser, causing a back-flow, in a process known as 'stalling'. The back-flow behavior of stalled diffusers is uniquely related to the diffuser geometry as described in the flow regime chart of Fox and Kline [1], shown in figure 1.1.

Whenever stalling in a diffuser flow occurs, regions of the stalled flow block the normal flow causing poor pressure recovery and severe asymmetry of the flow. Even though the diffuser performance, as characterized by the pressure recovery, is dependent on more parameters than just the geometry, figure 1.2 represents the general relationship between the flow regimes and

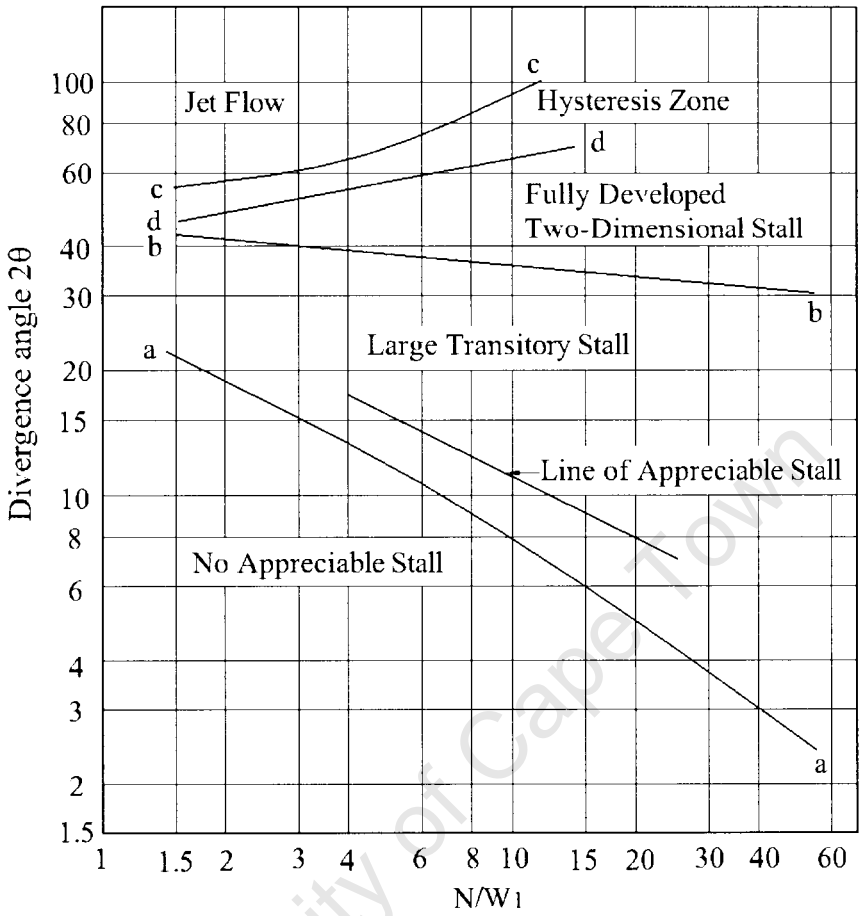

Figure 1.1: Flow regimes in two-dimensional diffusers

the geometry. Ashjaee and Johnston [2], among others, have indeed shown that the maximum pressure recovery, C^*_{pr}, in a diffuser is attained when there is an appreciable stall in the diffuser, (see figure 1.2), and occurs when the total divergence angle is between $7° - 10°$.

As will be illustrated in the literature survey in this chapter, the difficulties in understanding the physics of the flow in severely asymmetrical flows in wide-angled diffuser are associated with a lack of adequate experimental data and accurate flow prediction methods. The studies carried out in this research address this inadequacy. The first objective of this research was to

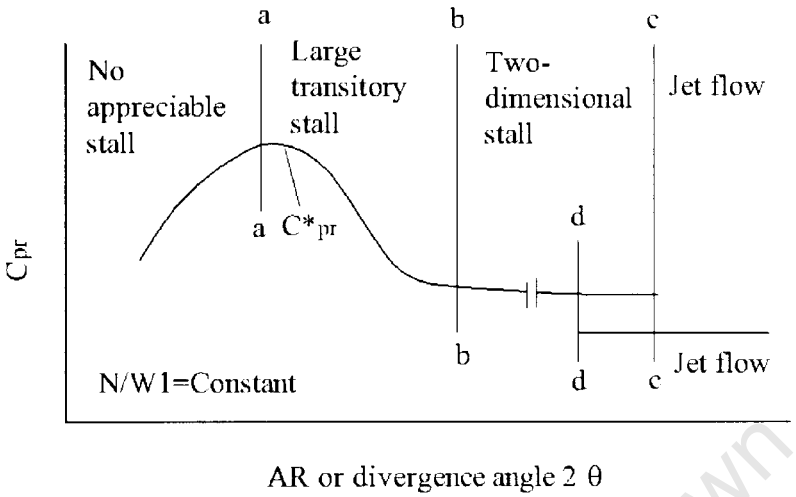

Figure 1.2: Relationship between flow regimes and pressure recovery

provide a reliable data bank contribution, whereby the complete flow-field data for unvaned wide-angled diffusers in the fully stalled flow regime were experimentally measured. The flow-field data included the axial and lateral velocity profiles, static pressure profiles, and pressure recovery coefficients, measured in diffusers whose total divergence angles were 30°, 40° and 50°. The measurements were carried out at Reynolds numbers between 1.07×10^5 and 2.14×10^5 based on the inlet hydraulic diameter and centreline velocity.

To minimize the influence of diffuser geometry at the inlet and achieve a fully developed inlet flow, the aspect ratio at the inlet and the normalized inlet duct length were chosen to be 4, and $N/W_1 = 10$, respectively. The resulting inlet blockage factor B, obtained from preliminary tests was approximately 0.015. The measured recovery and mapping data was then compared with the data of Reneau et al. [3] for $B = 0.015$. For each diffuser, the influence of Reynolds number on the flow-field, the influence of change of the wall to which the flow becomes attached after stalling, and the two-dimensionality of the flow were investigated.

The second objective was to investigate the change in the pressure recovery due to the placement of inlet vanes in the three diffusers as suggested by Cochran and Kline [4], Moore and Kline [5], and Feil [6]. Cochran and Kline have shown that the vanes' geometries play an important role in enhancing the pressure recovery. The design criteria of the vanes was based on their results.

The third objective was to numerically solve for the flows in the three wide-angled diffusers when they are both unvaned and vaned. To give a complete picture of all the flow regimes, diffusers that are in the unstalled, large-transitory and fully developed two-dimensional stall regimes, were included in order to compare the pressure recovery mapping data with that of Reneau et al. [3]. In this respect, 10 diffusers of total divergence angles, 4°, 7°, 10°, 15°, 20°, 28°, 30°, 40°, 42°, and 50° were modeled. Four eddy viscosity models that are known to give reasonable prediction for flows in adverse pressure gradients were used, namely; the standard $k-\epsilon$, realizable $k-\epsilon$, Wilcox $k-\omega$ and Menter SST $k-\omega$ models. Model comparison was performed by simulating flows in the 50° diffuser because it provided the most stringent flow conditions. The best overall model was then extended to predict flows in all the other diffusers. The predicted results were then compared with the experimental results obtained from this research and also those from published literature.

Previous experimental and numerical work relating to separated flows in diffusers is reviewed in this chapter. While reviewing the numerical work, performance of the common turbulence models in separated and adverse pressure gradient flows are discussed. The objectives of this research are summarized at the end of the chapter.

Chapter 2 gives a 'thumbnail' sketch of the Reynolds-averaged Navier-

Stokes (RANS) equations that are used to develop the turbulence models used in this research and are summarized towards the end of that chapter. No attempt is made to discuss the physics behind their derivations, but the physical interpretation of each term that arises from the Reynolds averaging of the Navier-Stokes equations is discussed.

The experimental apparatus and instrumentation for the data acquisition are discussed in chapter 3. Since the calibration of the instruments was done following the standard procedures, the calibration data has been omitted from this chapter. The calibration procedures, curves and charts are instead given in appendix B.

In chapter 4, the numerical treatment of the diffuser flows is outlined by a discussion of the solution and the meshing techniques used. A brief introduction to the finite volume solution technique is also given.

The primary purpose of a diffuser is to obtain pressure recovery. When diffusers with different geometries are to be compared. non-dimensional pressure recovery coefficients are used. Due to the differences in the literature in defining the reference pressure against which pressure recovery is measured, it was found necessary to define the pressure coefficients as they are used in this research. These coefficients, together with a short mention of the error analysis techniques adopted in this research are presented in chapter 5.

Both the experimental and numerical results are presented, discussed and compared in chapter 6. In order to avoid repetition of graphical results that give similar trends here, the overall observations are summarized in the form of tables when discussing the results. The remaining graphs are then given as a data bank contribution in appendix A. The important conclusions that can be drawn from this study are presented in chapter 7.

1.2 Review of experimental work

The early research on diffusers, as reported by Reid [7], is associated with the water table diffuser experiments of Professor A. H. Gibson in 1913. Despite some shortcomings of his techniques as seen from the modern view point, his results indicated that diffuser flows were characterized by sharply defined minimum pressure losses which occurred at divergence angles of between 5.5° and 11°. He demonstrated that for divergence angles beyond this range, flow separated from diffuser walls, leading to poor pressure recovery. While Gibson's work suggested that diffuser performance was affected by the geometry of the diffusing passage, there seemed to be no systematic research on these types of flows because of a lack of suitable measuring techniques for recirculating flows. A review of the status of early research on diffusers is well covered by Reid [7].

Through flow visualization experiments, most researchers had observed that the flow patterns in diffusers depended heavily on the diffuser geometry, distinguished by the unique flow behavior of the four regimes shown in figure 1.1 and briefly described below. Detailed descriptions of these flow regimes are given by Fox and Kline [1, 8].

(i) Appreciable stall regimes are where distinguishable regions of back flow separation bubble formation of the order of magnitude of the boundary layer thickness are observed, but are washed downstream by the main flow before forming again.

(ii) Large transitory stall regimes are where the entire flow region is characterized by large, low frequency stalls that are formed and washed away in a transitory pattern that persists indefinitely. The flow is thus very unsteady and experimental measurements in this region are somewhat

difficult. The time scale of transitory stall behavior appears to be a strong function of throat Reynolds number [9, 10].

(iii) Fully developed two-dimensional stall regimes are where the flow is asymmetric, fully developed and steady, and attaches itself to one wall. The wall onto which the stall attaches itself is arbitrary and is suspected to be caused by small flow instabilities upstream of the diffuser.

(iv) Jet flow is a relatively steady flow, with the flow symmetrically separating from both walls.

The demarcation of these flow regimes is very weakly dependent on Reynolds number over the range from 6×10^3 to 3×10^5. However, the performance of a diffuser, measured in terms of static pressure recovery, and the flow field are affected by many parameters. Primary among them are; the Reynolds number, the inlet boundary-layer conditions, the level of turbulence at the inlet, and the diffuser geometry. Indeed, there is a strong relationship between inlet boundary layer conditions (characterized by inlet free-stream turbulence and boundary layer thickness) and the diffuser performance, as Waitman et al. [11] showed.

An understanding of the relationships between these parameters and their effects on the diffuser performance leads to a rational basis for diffuser design and the use of experimental data to develop and validate numerical codes. In trying to experimentally relate each of these parameters to diffuser performance, a fertile ground for most researchers was formed. This review does not in any way attempt to cover all the contributions made in trying to achieve such objectives, but instead highlights some of the major conclusions that can be drawn from previous research.

The relationship between diffuser geometry and performance is mainly

covered by Reneau et al. [3], Kline et al. [12], and Sagi and Johnston [13], among others. Firstly, they paid attention to the variations that gave the best diffusing angle corresponding to the maximum effectiveness, C_{pr}^{*}, for a given length to width ratio, N/W_1. Secondly, they determined the best ratio N/W_1 for a given area ratio between inlet and outlet A_2/A_1, that gave the maximum effectiveness. They concluded that the optimum effectiveness is achieved when the total divergence angle of the diffuser is approximately 7° and the ratio N/W_1 not exceeding 25. They further reported that at high divergence angles, the area ratio became less significant as a variable for determining pressure recovery. At such angles, the important parameters are the ratio N/W_1, the inlet conditions, and the geometry of any downstream tailpipe. Even though their work did not address the flow-structure within the diffusers, and instead covered only the pressure recovery between the inlet and the outlet of the diffusers, the work of Reneau et al. [3] is widely used in the design and mapping of two-dimensional diffusers.

Experimentally, the boundary layer thickness can be adjusted so that the relationship between diffuser performance and the boundary layer characteristics can be understood. One technique for instance, that was used by Norbury [14], and Johnston and Powars [15] to vary the inlet blockage factor was the artificial placement of thin rods on the walls upstream of the diffuser inlet. The important conclusion that was drawn from their research was that for a fixed geometry and Reynolds number, pressure recovery usually decreases as the inlet blockage increases. Their research further showed that for aspect ratios $b/W_1 > 4$, the influence of the aspect ratio on performance is negligible for a uniform diffuser inlet flow.

However, uniform flow at the inlet of the diffuser is not always achieved in practice, since various upstream flow conditions like obstructions due to

blades, struts, etc. may shed wakes. In any case, it is known that the introduction of the wide-angled diffuser causes severe non-uniformity in the upstream inlet channel. McMillan and Johnston [16] have argued that a uniform velocity profile carries the minimum momentum flux possible at a given flow rate, so transformation of a distorted profile to a more uniform one, even in a constant area duct, can result in an increase in static pressure (a process that occurs in diffuser tail pipes). Based on this understanding therefore, the inlet core-flow velocity profile distortions can cause a significant change in the pressure-recovery performance and, by implication, the flow regimes.

Indeed, Wolf and Johnston [17], and Kaiser and McDonald [18] introduced a non-uniformity to the boundary layer at the inlet and found that the onset of stall occurred at a lower value of area ratio for fixed length to width ratio for wake type inlet profiles than diffusers with irrotational inlet core velocity profiles. Thus line $a - a$ and $b - b$ of figure 1.1 are appreciably shifted downwards. Even though they did not obtain pressure recovery data, their results suggested that a slightly distorted wake type inlet velocity profile may be beneficial to performance. But the creation of a wake as a remedy to poor performance is unfavorable, due to other losses associated with this.

Many researchers, among them, Reneau et al. [3], and Sagi and Johnston [13] have shown that at low Mach numbers, performance is quite insensitive to Reynolds number. Recently, Kibicho et al. [19], and Kibicho and Sayers [20] in fact confirmed this insensitivity and demonstrated that the velocity field within the wide-angled diffuser, is little influenced by Reynolds number. Most of this experimental work was carried out at inlet Mach numbers below 0.2. Runstadler and Dean [21] have investigated the effect of varying the

diffuser inlet Mach number on both the flow regimes and the performance. Variation of Mach number at low flow Mach numbers marginally influenced the performance, while in supersonic flow regimes, there was little gain in performance as the Mach number was raised.

If the basic mechanisms that control diffuser performance can be understood, then, this will lead to the design of systems which employ techniques that utilize these mechanisms in improving the efficiency of fluid machines. Once the separation of the flow from the walls in adverse pressure gradients is prevented by any method, then, that method can be applied to design an efficient diffuser with a large divergence angle and a shorter length. Hoffman [22] has argued that if such a method can enhance the transfer of free stream turbulent energy to the diffuser walls, then this transfer of energy will decrease the distortion of the velocity profiles within the diffuser and delay the onset of separation. As one means of facilitating this energy transfer, Furuya et al. [23,24] applied boundary layer suction to the low momentum fluid at the diffuser walls, and succeeded in improving the performance in both conical and two dimensional diffusers of high divergence angles. Energization of the boundary layer fluid by the use of vortex generator as another method of improving efficiency has successfully been tried by Senoo and Nishi [25].

Other tried techniques for reducing the velocity profile distortion are, the inclusion of entry guide vanes [4,6], and change of local pressure gradients by change of wall shape [26]. Recently, Raghunathan and Cooper [27] have tried to improve the diffuser performance by controlling the boundary layer growth by use of wall slots on the diverging walls of two-dimensional diffusers. The slots produced a modest improvement in pressure recovery but considerably raised the angle at which stall in two dimensional diffusers began.

Clearly, a guideline on the design of diffusers using any of these perfor-

mance improvement techniques is obviously desirable. This is so because, even though these auxiliary devices may eliminate stall, they are themselves sources of loss of performance since they introduce obstruction to the flow passages.

1.3 Review of numerical work

1.3.1 Theoretical modeling of diffuser flows

The role played by the inlet boundary layer in the structure of diffuser flows, as has been demonstrated in the foregoing review, suggests the use of boundary layer theory in performance analysis. However, observation of the actual flow patterns and the local pressure distributions in the stalled diffusers precludes the use of the established boundary layer techniques in all but the most extra ordinary unstalled simple situations. In the fully-developed, two-dimensional stall regime, which is the study case of this research, the flow becomes asymmetric because it is deflected over to one diverging wall by the stall whose size and shape cannot be predicted in advance. This stall causes unpredictable and different pressure distributions to be imposed on the different diffuser walls. Without a method for predicting the wall pressure distributions, no boundary layer growth and stall predictions can be made by the use of boundary layer techniques alone.

Once a diffuser flow is stalled therefore, most theoretical work relies on correlations of actual experimental data and on the semi-empirical performance prediction methods derived from these data. A combination of boundary layer theory and such correlations have been used with some success by Reneau et al. [28] and Mcmillan and Johnston [29] to map and predict the performance of narrow angle diffusers in the transitory stall regime.

In an attempt to provide an understanding, and a computational pro-

cedure of engineering utility for wide angle diffuser flows, containing large regions of separation, Wooley and Kline [30] developed what they called a zonal model. They divided the flow field into four zones for the sake of modeling, namely;

(i) attached boundary layer (on the unstalled side),

(ii) effective flow channel (effective area of flow),

(iii) free shear layer, and

(iv) the stall zone.

They used the experimental data of Chui and Kline [31] to determine these regions. Their diffuser had a sharp corner so that the location of the detachment, known beforehand, occurred at the corner. A similar zonal model approach for steady flows, where the pressure gradient and conditions for detachment are predefined, has been used to predict optimum pressure recovery by Ghose and Kline [32], Wysocki and Kazimierski [33], and Vujilic and Crnojevic in [34, 35].

The work by Wooley and Kline [30] was successful in modeling diffusers operating in the two-dimensional, fully stalled regime, while Ghose and Kline [32] succeeded in developing a numerical scheme that predicted diffuser performance in the unstalled and the incipient (appreciable) stall regime. Bardina et al. [36] combined these two schemes to produce a prediction method that covered the first three regimes in the chart of Fox and Kline (see figure 1.1), i.e., unstalled flow, transitory stall, and fully stalled flow. The success of this approach known as the 'unified integral method', (UIM) are well documented in a review carried out by Johnston [37].

In a typical diffuser design problem, the prescribed pressure distribution data necessary for this solution technique, is usually not available, since the

pressure distribution must form part of the solution. Thus, even though all these authors report success in their methods, the application of their models is limited to their study cases only, and are not suitable for general use.

Separated flows in wide-angled diffusers of practical engineering use are inherently turbulent. Due to the absence of reliable turbulence data for wide-angled diffusers, the prediction methods available in the literature for such flows are mainly based on the one-dimensional zonal models. Some attempts made by Pope [38] to compute stalled diffuser flows using the time-averaged Navier-Stokes equations and the two-equation $k-\epsilon$ turbulence model were not particularly encouraging. Pope considered a diffuser connected smoothly to a long parallel inlet and outlet channel for which symmetric boundary conditions at both inlet and outlet were applied. The solution had a symmetrical stall pattern along the diverging walls contrary to the well observed asymmetrical stall patterns found in practice. Further numerical trials of the $k-\epsilon$ model in wide-angled diffusers have been tried by Habib and Whitelaw [39] who have transformed the transport equation for $k-\epsilon$ model from their usual cartesian to the curvilinear coordinates in order to solve for conical diffuser flows in the fully stalled regime. Even though there cannot be a direct incorporation of their technique into the current study case, they reported success in the prediction of the general features of the flow field in diffusers and provided a promising future for the modeling of flows in severe adverse pressure gradients.

The reason why there is scarce numerical work on wide-angled diffusers is because reliable experimental data and especially data that covers the velocity flow-field is lacking. Of the available data in literature, only the pressure recovery and diffuser mapping information is given. Contrary to this, flows in narrow plane asymmetric diffusers have been extensively stud-

ied experimentally by many researchers, among them, Obi et al. [40], Buice and Eaton [41], and Gullman et al. [42]. These flow cases are considered suitable for the fundamental studies of separation because they consist of fully developed upstream channel flows, separation bubbles due to adverse pressure gradient (APG) and downstream-reattached flows. These experimental data have been used in validating numerical schemes by numerous authors, some of whom are listed in table 1.1. However, none of the models tested are

Table 1.1: Numerical work on asymmetric diffusers

Researcher(s)/Reference	**Model(s)**	**Year**
Gullman [43]	Modified $k-\omega$	2004
Lim and Choi [44]	LES, $k-\epsilon-v^2-f$	2004
Kibicho and Sayers [45]	Wilcox $k-\omega$	2004
Ohta et al. [46]	DNS	2003
Jungsoo [47]	LES	2002
Skote and Henningson [48]	DNS	2002
Apsley and Leschziner [49]	Wilcox $k-\omega, k-\epsilon$, SST $k-\omega$	2000
Kaltenbach et al. [50]	LES	1999
Kaltenbach [51]	LES	1998
Fatica et al. [52]	LES	1997
Fatica and Mittal [53]	LES	1996

capable of resolving all the flow features in the asymmetric diffusers. Indeed, in an ERCOFTAC workshop [54], different numerical approaches with varying turbulence models were tested and compared to the Buice and Eaton [41] data-set. In this workshop, the performances of the $k-\epsilon$, the $k-\omega$, the SST and the Reynolds stress models, and the large eddy simulations in APG flows were tested. In order to strike a balance between the complexities of

the numerical codes and the computational costs, it was observed that the two-equation models gave results that were comparable to the more complex Reynolds stress and LES models of these types of flows.

Overall, the SST model gives a good prediction of the separation point compared to all the other models, even though it predicts a flow recovery (reattachment) length that is larger than observed in the experiments [55].

The plane asymmetric diffuser of Buice and Eaton [41] has also been used as a test case for commercial codes. The investigation performed by Iaccarino [56] and aimed at finding the versatility of some commercial codes in this complex flow, overwhelmingly concluded that regardless of the commercial code used, the $k-\epsilon$ model is unable to capture the recirculation zone and performs poorly in APG flows.

On the understanding that the main features of flows in the narrow asymmetric diffusers are mainly caused by the adverse pressure gradients, then any good numerical modeling scheme of such flows will provide a good guideline when considering flows in severe adverse pressure gradients.

1.3.2 Turbulence models in APG and separated flows

Adverse pressure gradient shear layers are of great practical interest, as they occur in aerofoil flows, turbo-machinery blading, in diffusers, etc, and sometimes involve flow separation. Turbulence models have been used over the past several decades to predict these types of flows. The $k-\epsilon$ model has emerged as the most popular two-equation turbulence model, mainly because, ϵ, the rate of dissipation of the turbulent kinetic energy, appears naturally in the k-equation and can be derived from the averaged Navier-Stokes equations without introducing additional variables. The dissipation rate, ϵ, thus becomes the obvious choice for the second turbulent quantity in the formulation

for turbulent isotropic eddy viscosity, ν_t, required when the eddy viscosity models are to be used [57].

Another well known two-equation turbulence model is the Wilcox $k-\omega$ model [58]. It has the advantage that it does not require damping functions in the viscous sub-layer since it solves the exact equations for k and ω in the near wall region making the equations in this region less stiff. Several comparisons of performance of the popular turbulence models in equilibrium APG boundary layer and separated flows have shown that the Wilcox $k-\omega$ model gives better prediction in the logarithmic region [59–62]. However, when applied to the free shear layers, it is found that results from the $k-\omega$ model have a strong dependency on the free-stream value of ω [63, 64]. To circumvent the freestream dependency of the Wilcox $k-\omega$ model, Menter created a new model called the shear stress transport, (SST) $k-\omega$ model [65], that blends the $k-\epsilon$ and the $k-\omega$ models. It utilizes the $k-\omega$ model in the wall region, where the exact transport equations are solved, and gradually switches to the $k-\epsilon$ model away from the wall, to benefit from the freestream dissipation rate dependency of the $k-\epsilon$ model.

The wisdom of the widespread use of the $k-\epsilon$ model was raised first by Chambers and Wilcox [66] as early as 1977, by demonstrating two serious flaws in its application to wall-bounded flows. Firstly, they showed that its equations can be integrated through the viscous sub-layer only with the aid of viscous damping functions and this makes the equations very stiff. Besides, the lack of universality of the wall functions has been frequently criticized, with Lai and So [67] clearly demonstrating the inadequacy of the wall functions approximations and the need to correct for pressure gradient effects when such functions are used. Secondly, they demonstrated that it is very inaccurate for APG flows.

Analysis based on direct numerical simulation (DNS) data have shown that at the walls, ϵ is non-zero, finite, and not known in advance. Numerically, this is an awkward situation since a boundary condition for ϵ is required at the walls. A remedy to this problem has been to solve for the reduced dissipation rate, $\tilde{\epsilon}$, and include an additional term in the k-equation (see e.g. Launder and Sharma [68]). Another possible solution to this deficiency is to solve for an alternative quantity to ϵ. An example of such a quantity relevant to this study is ω, whose well-posed wall boundary condition, $\omega_w \approx y^{-2}$, has been shown to have a numerically stabilizing effect. In fact, a study on the performance of eddy viscosity models by Huang and Bradshaw [60], concluded that the optimum choice for the length scale determining equation for APG flows, is the specific dissipation rate, $\omega = \epsilon/k$.

The main effect of interchanging ϵ with ω in the $k-\epsilon$ model, is the introduction of a turbulent cross diffusion term in the ω-equation [69–71]. The role played by this term depends on the sign of the gradients for both k and ω, and is usually limited to the region close to the wall. In general, this term reduces ω and enhances k near the wall, since the gradients are usually of opposite signs. The addition of this term helps to improve the $k-\omega$ model performance in the separated recirculating region and in APG flows, where turbulent kinetic energy is usually under-predicted by the $k-\epsilon$ model. It is disturbing to see the now widely used $k-\epsilon$ turbulence model being seriously in error for relatively simple APG equilibrium boundary layers. As was observed in the 1980-81 AFOSR-HTTM-Stanford Conference on Complex Turbulent Flows [72,73], the differences between this model and the existing data manifest themselves mainly in the consistently over-predicted skin friction values and the tendency of the calculated flow to remain attached where experiments indicate separation.

Numerous researchers have tested most of the popular turbulence models in APG boundary layer flows and compared the results with reliable experimental data available in the literature such as the data from Samuel and Jourbert [74]. Table 1.2 gives a summary of some of the recent numerical work in such flows.

Table 1.2: Numerical work in APG and separated boundary layer flows

Researcher(s)/Reference	**Model(s)**	**Year**
Yorke & Coleman [62]	BL, SA, $k-\epsilon$, SST	2004
Tong et al. [75]	$k-\omega$, SST	2003
Bredberg et al. [69]	Modified $k-\omega$, $k-\epsilon-v^2-f$, Wilcox $k-\omega$	2002
Mohammad & Hukam [76]	$k-\epsilon$, $k-\omega$, SST	1999
Rao & Hassan [77]	Modified $k-\omega$, Wilcox $k-\omega$	1998
Peng et al. [78]	Modified $k-\omega$, $k-\epsilon$	1997
Wilcox [79]	Variants of Wilcox $k-\omega$ and standard $k-\epsilon$	1993
Menter [59]	BL, JK, BB, Wilcox $k-\omega$	1992

KEY

BL Baldin-Lomax Zero-equation model [80]
JK Johnson-King Half-equation model [81]
BB Baldwin-Barth One-equation model [82]
SA Spalart-Allamaras One-equation model [83]

On reviewing the results from these researchers, the general view taken by the current author, is that the Menter SST $k-\omega$ model performs well at locating the separation point for APG, and that it gives the best overall agreement with DNS and experimental data in predicting the mean flow properties in APG and recirculating flows. In the current research, only the Wilcox $k-\omega$, the $k-\epsilon$ and its variants, and the SST will be considered, since

much lower computational effort is required to achieve results comparable to those of the DNS, the RSM, and the LES models in APG flows.

1.4 Summary of the review

From the foregoing review, three salient observations can be made. Firstly, little reliable experimental data for wide-angled diffuser flows is available, while of the available literature, only static pressure recovery data, and flow regime mapping data is provided. Moreover, even though the literature shows that there are several techniques for eliminating stall and improving diffuser efficiency, such as entry vanes, very little systematic research has been carried out. Consequently, careful and systematic data for flows in wide-angled diffusers are required to solve this long standing, but still important diffuser flow problem.

Secondly, there are no successful a-priori theoretical or numerical methods, short of CFD simulations that exist for diffuser flows which are stalled. All the tried theoretical models are based on one dimensional zonal models and rely heavily on semi-empirical relations derived from experimental data. Thirdly, compared to the most popular eddy viscosity turbulence models, that have been shown to perform dismally in APG flows, the Menter SST $k-\omega$ model has emerged as the best model in predicting the APG and recirculating flows.

It is against this background that the experimental and numerical measurements in unvaned and vaned wide-angled diffusers in this research were obtained.

1.5 Strategy and summary of the objectives

This research was carried out in three phases. The first phase involved the design, and manufacture of both unvaned and vaned diffusers of such geometries that comparisons of measured pressure recovery results and diffuser mapping data with those data that exist in the literature were made possible. In this phase, design and fabrication of the experimental ducting and the yaw meter for velocity measurement was also performed. Finally in this first phase, the data acquisition system and the computer data acquisition software were developed. In the second phase, the equipment used in this study was calibrated and the experimental data collected. Numerical modeling of flows in wide-angled diffusers was carried out in the third phase.

The objectives of this research were formulated so that they could address the shortcomings of the issues raised in section 1.4 in three main ways. Firstly, the complete velocity-field, static pressure, and pressure recovery fields in diffusers of total divergence angles of 30°, 40°, and 50° were experimentally measured. All the diffusers were of aspect ratio $AS = 4$, length to width ratio $N/W_1 = 10$, and an inlet blockage factor $B \approx 0.015$. Secondly, inlet vanes in the three diffusers were introduced, and the resulting changes in the pressure recovery data due to this inclusion were investigated, and compared with the experimental data of Cochran and Kline [4]. Thirdly, the flows in the three wide-angled diffusers when they are both unvaned and vaned were numerically determined. In order to compare numerical results with the experimental data of Reneau et al. [3], and to cover at least the first three flow regimes in figure 1.1, seven extra diffusers of total divergence angles, 4°, 7°, 10°, 15°, 20°, 28°, and 42° were also modeled.

Chapter 2

Theoretical Treatment

2.1 Governing equations

Most fluid flows, which are encountered in engineering applications, are turbulent. Even though there is no precise definition of what a turbulent flow is, it has a number of characteristic features such as; irregularity, diffusivity, large Reynolds number, three-dimensionality, dissipation, and consists of a large spectrum of turbulent eddies with different length scales (see Hinze [84], Tennekes and Lumley [85], and Schlichting [86]). Every turbulent flow pattern has its own unique characteristics that are associated with its initial and boundary conditions. Since turbulent flows can only be adequately described by the Navier-Stokes equations, a complete solution for such flows would then require that the Navier-Stokes equations be solved for all the length scales present, while imposing the unique initial and boundary conditions. Due to the large number of turbulent eddies present, and the uniqueness of each turbulent flow, no general solutions are therefore feasible in these types of flows. Furthermore, analytical solutions of the highly non-linear Navier-Stokes equations can only be possible after imposing a number of simplifying assumptions even for the simplest turbulent flows cases. This situation is made worse by the inherent strong pressure-velocity coupling

present in the Navier-Stokes equations. Thus, the only feasible approach to overcome this inadequacy of the analytical techniques, is the numerical approach. The treatment of the Navier-Stokes equations to facilitate the numerical solutions of the turbulent flows that are of practical engineering interest is briefly outlined in this section.

2.1.1 Navier-Stokes equations

In the absence of gravitational and other body forces, the Navier-Stokes momentum transport and continuity equations of an incompressible flow are given in Eqs.2.1 and 2.2 respectively.

$$\frac{\partial \tilde{u}_i}{\partial t} + \tilde{u}_j \frac{\partial \tilde{u}_i}{\partial x_j} = -\frac{1}{\rho}\frac{\partial \tilde{p}}{\partial x_j} + \upsilon \frac{\partial^2 \tilde{u}_i}{\partial x_j \partial x_j} \tag{2.1}$$

$$\frac{\partial \tilde{u}_i}{\partial x_i} = 0 \tag{2.2}$$

The instantaneous pressure, $\tilde{p}$, and the three instantaneous velocity components, $\tilde{u}_i$, must be evaluated if a complete description of the fluid motion is to be given. Numerically, this requires that one solves the coupled differential Navier-Stokes equations with a very fine grid to resolve all the scales for the large number of eddies present. This demands availability of immense resources in terms of computational effort and ability. Fortunately, engineers are usually not concerned with all the details of the turbulent motion, but rather with its effects on the gross properties of the flow. Consequently, there is no need to solve for the instantaneous variables if averaged variables are all that is required. There are several techniques that are used to obtain this averaged information such as; the ensemble averaging, density-weighted averaging, Reynolds averaging, etc. (see Chen and Jaw [57]). The most com-

monly used approach to approximate the mean behavior of the flow is the Reynolds averaging technique.

2.1.2 Reynolds averaged equations

By splitting the instantaneous velocities and pressure into mean and fluctuating parts, respectively (Eq.2.3),

$$\begin{aligned} \tilde{u}_i &= U_i + u_i \\ \tilde{p} &= P + p \end{aligned} \tag{2.3}$$

and then applying the Reynolds averaging technique, the Reynolds Navier-Stokes equations (RANS) and continuity equations for the mean flow are obtained (Eq.2.4 and 2.5).

$$\frac{\partial U_i}{\partial t} + U_j \frac{\partial U_i}{\partial x_j} = -\frac{1}{\rho}\frac{\partial P}{\partial x_j} + \upsilon \frac{\partial^2 U_i}{\partial x_j \partial x_j} - \rho \overline{u_i u_j} \tag{2.4}$$

$$\frac{\partial U_i}{\partial x_i} = 0 \tag{2.5}$$

The decomposition of the flow into a mean and a turbulent fluctuating flow has isolated the effects of fluctuation on the mean flow but has introduced a new term, $-\rho\overline{u_i u_j}$, into the Navier-Stokes equations (cf. Eqs.2.1 and 2.4). The term $-\rho\overline{u_i u_j}$ is known as the Reynolds stress and represents the mean transport of fluctuating momentum by turbulent velocity fluctuations. Its existence requires that u_i and u_j be correlated. The resulting tensor from the Reynolds stresses is called the Reynolds stress tensor, τ_{ij}, with nine components, only six of which are unknown due to the symmetry of the tensor. It is now required that solution for the six Reynolds stresses, pressure and the three velocity components (a total of ten variables) from the available four equations (Eqs.2.4 and 2.5) of motion be obtained if we are to fully

describe the fluid motion. The number of unknown variables are more than the number of available equations! And this, is the closure problem of turbulence. Attempts to obtain additional equations for the Reynolds stresses generate even more unknown correlation terms like, $-\rho\overline{u_i u_j u_k}$, from the non-linear inertia terms, as will be seen in section 2.1.3. This is a fairly desperate situation to be in.

The way forward then, is to try and guess a relationship between the Reynolds stress tensor, and the mean strain rate, since the function of the Reynolds stresses seem to be similar to that of the viscous stresses. The most commonly used approximation is the Boussinesq approximation, (Eq.2.6), that tends to make the turbulent Reynolds stresses imitate the behavior of laminar viscous stresses.

$$-\overline{u_i u_j} = \upsilon_t \left(\frac{\partial U_i}{\partial x_j} + \frac{\partial U_j}{\partial x_i} \right) - \frac{2}{3}\delta_{ij}k \tag{2.6}$$

Thus a coefficient of viscosity for turbulent flows, called the turbulent eddy viscosity, υ_t, and that plays a similar role to the molecular viscosity is introduced. A good guess of such relationships will ensure that the diffusion of the turbulent transport properties by turbulence will be proportional to the spatial gradients of the quantity they are meant to transport. Finally, to describe the turbulent flow behavior uniquely, it is then in order to characterize turbulent phenomenon by one turbulent scale on the basis of turbulent kinetic energy and its rate of dissipation.

2.1.3 Closure of the RANS equations

Reynolds stresses play a very dominant role in the theory of the mean momentum transfer by turbulent motion. Numerically, implementing the six additional transport equations required to close the RANS equations for the

large number of scales present in a turbulent flow will require a large additional computational effort. The use of the simple eddy-viscosity model will instead require only two transport equations, one each to determine the velocity-scale and, the length-scales of the modeled turbulence motion. The velocity-scale is commonly taken as, $\sqrt{k}$. The choice of an auxiliary length-scale-determining parameter is connected to the dissipation term in the k-equation. The most widely used is the dissipation rate, ϵ, but also the inverse of the turbulence time scale, ω, has proven appropriate. Thus, to be in a position to develop a model that describes turbulent motion and to understand the process of maintenance of a turbulent flow, it is instructive that the underlying physics governing the transport of momentum by the Reynolds stresses, the physics that govern the transfer of the turbulent kinetic energy and the physics of dissipation of the turbulent kinetic energy be understood. Details of the manipulation of the RANS equations to obtain the exact equations for $-\overline{u_i u_j}$, k, ϵ, and ω are well documented in references [57, 86, 87].

Reynolds stresses

By manipulating the exact momentum equations and applying some algebra, the exact Reynolds stress transport equations are obtained as;

$$\frac{D\overline{u_i u_j}}{Dt} = \underbrace{\frac{\partial}{\partial x_l}\left(-\overline{u_i u_j u_l} - \overline{\frac{p}{\rho}\left(\delta_{ij}u_i + \delta_{ij}u_j\right)}\right)}_{D^t_{\tau_{ij}}} + \underbrace{\frac{\partial}{\partial x_l}\left(\upsilon\frac{\partial \overline{u_i u_j}}{\partial x_l}\right)}_{D^\upsilon_{\tau_{ij}}} \underbrace{-\left(\overline{u_i u_l}\frac{\partial U_j}{\partial x_l} + \overline{u_j u_l}\frac{\partial U_i}{\partial x_l}\right)}_{P_{\tau_{ij}}} \underbrace{- 2\upsilon\overline{\frac{\partial u_i}{\partial x_l}\frac{\partial u_j}{\partial x_l}}}_{\phi_{\tau_{ij}}} + \underbrace{\overline{\frac{p}{\rho}\left(\frac{\partial u_i}{\partial x_j} + \frac{\partial u_j}{\partial x_i}\right)}}_{\Pi_{\tau_{ij}}} \tag{2.7}$$

Inspection of Eq.2.7 reveals that the molecular diffusion of the momentum, $D^\upsilon_{\tau_{ij}}$, and the the production of Reynolds stresses, $P_{\tau_{ij}}$, require no modeling

as they do not involve triple correlations of fluctuating quantities. However, the turbulent diffusion of the momentum, $D^t_{\tau_{ij}}$, the viscous dissipation of the Reynolds stresses, $\Phi_{\tau_{ij}}$, and the pressure-strain, $\Pi_{\tau_{ij}}$ terms are to be modeled and are presented in Eq.2.8 to 2.11.

$$D^t_{\tau_{ij}} = C_s \frac{\partial}{\partial x_l}\left(\left(\frac{k\overline{u_l u_k}}{\epsilon}\right)\frac{\partial \overline{u_i u_j}}{\partial x_k}\right) \tag{2.8}$$

Modeling the turbulent dissipation of momentum according to Eq.2.8 can sometimes introduce numerical instabilities [88]. It is usually simpler to use a scalar eddy diffusivity so that the turbulent dissipation of momentum becomes;

$$\left(D^t_{\tau_{ij}}\right)_m = \frac{\partial}{\partial x_l}\left(\frac{\upsilon_t}{\sigma_k}\frac{\partial \overline{u_i u_j}}{\partial x_k}\right) \tag{2.9}$$

$$\left(\phi_{\tau_{ij}}\right)_m = \frac{2}{3}\delta_{ij}\epsilon \tag{2.10}$$

The pressure strain term is given in Eq.2.11 as suggested by Launder and others in [89–92].

$$\begin{aligned}(\Pi_{ij})_m = &- C_1\frac{\epsilon}{k}\left(\overline{u_i u_j} - \frac{2}{3}\delta_{ij}k\right) - C_2\left(-\left(\overline{u_i u_j}\frac{\partial U_j}{\partial x_i} + \overline{u_i u_j}\frac{\partial U_i}{\partial x_j}\right)\right) \\ &- C_2\left(-\frac{2}{3}\delta_{ij}\left(-\overline{u_i u_j}\frac{\partial U_i}{\partial x_j}\right)\right)\end{aligned} \tag{2.11}$$

The first part of the Eq.2.11 involves only the fluctuating velocities and is known as slow distortion or slow return to isotropy. The second part involves the mean velocity gradients and is known as rapid return to isotropy. Finally, Eq.2.12 gives the modeled transport equation for $\overline{u_i u_j}$.

$$\left(\frac{D\overline{u_i u_j}}{Dt}\right)_m = \left(D^t_{\tau_{ij}}\right)_m + D^v_{\tau_{ij}} + P_{\tau_{ij}} + \left(\Pi_{\tau_{ij}}\right)_m - \left(\phi_{\tau_{ij}}\right)_m \tag{2.12}$$

Turbulent kinetic energy

Turbulent kinetic energy is defined as $k = \frac{1}{2}\overline{u_i u_i}$. Following this definition, the turbulent kinetic energy equation can be obtained by setting the value, $i = j$, in the $\overline{u_i u_j}$ equations (Eq.2.7), to get Eq.2.13.

$$\frac{Dk}{Dt} = \underbrace{\frac{\partial}{\partial x_l}\left(-\frac{1}{\rho}\overline{u_l p} - \overline{u_i u_i u_l}\right)}_{D_k^t} + \underbrace{\frac{\partial}{\partial x_l}\left(\upsilon\frac{\partial k}{\partial x_j}\right)}_{D_k^v} \underbrace{-\overline{u_i u_l}\frac{\partial U_i}{\partial x_l}}_{P_k} - \underbrace{\upsilon\overline{\frac{\partial u_i}{\partial x_l}\frac{\partial u_i}{\partial x_l}}}_{\phi_k} \quad (2.13)$$

The diffusion of turbulent kinetic energy due to viscous action, D_k^v, the production of the turbulent kinetic energy, P_k and the rate of dissipation of the turbulent kinetic energy, ϕ_k, (usually denoted as ϵ), require no modeling. The pressure strain term in Eq.2.7 disappears because of the continuity equation. The only term that requires modeling then, is the diffusion of turbulent kinetic energy due to the turbulent fluctuations term, D_k^t. Furthermore, once the $\overline{u_i u_j}$ equations have been modeled, then we do not need any further modeling for the k equation. The resulting modeled equation for D_k^t is;

$$\left(D_k^t\right)_m = \frac{\partial}{\partial x_j}\left(\frac{\upsilon_t}{\sigma_k}\frac{\partial k}{\partial x_j}\right) \quad (2.14)$$

The turbulent kinetic energy is therefore represented by Eq.2.15.

$$\left(\frac{Dk}{Dt}\right)_m = \left(D_k^t\right)_m + D_k^v + P_k - \epsilon \quad (2.15)$$

Kinetic energy dissipation rate

Before presenting the exact equation for the dissipation rate, it is important to recognize that it is one of the most important parameters since it affects the growth rate of k, and to also notice that it appears naturally in the equations for k. By applying some algebra to the turbulent momentum equation, we

can obtain the transport equation for ϵ as given in Eq.2.16.

$$\begin{aligned}\frac{D\epsilon}{Dt} = & \underbrace{\frac{\partial}{\partial x_l}\left(-\upsilon\overline{u_l\frac{\partial u_i}{\partial x_l}\frac{\partial u_i}{\partial x_l}} - \frac{2\upsilon}{\rho}\overline{\frac{\partial u_l}{\partial x_j}\frac{\partial p}{\partial x_j}}\right)}_{D_\epsilon^t} + \underbrace{\frac{\partial}{\partial x_l}\left(\upsilon\frac{\partial \epsilon}{\partial x_l}\right)}_{D_\epsilon^\upsilon} \\ & \underbrace{-2\upsilon\overline{u_l\frac{\partial u_i}{\partial x_j}}\frac{\partial^2 U_i}{\partial x_l \partial x_j} - 2\upsilon\frac{\partial U_i}{\partial x_j}\left(\overline{\frac{\partial u_l}{\partial x_i}\frac{\partial u_l}{\partial x_j}} + \overline{\frac{\partial u_i}{\partial x_l}\frac{\partial u_j}{\partial x_l}}\right)}_{P_\epsilon} \\ & \underbrace{-\left(2\upsilon\overline{\frac{\partial u_i}{\partial x_j}\frac{\partial u_i}{\partial x_l}\frac{\partial u_j}{\partial x_l}} + 2\overline{\left(\upsilon\frac{\partial^2 u_i}{\partial x_l \partial x_l}\right)^2}\right)}_{\phi_\epsilon}\end{aligned} \tag{2.16}$$

where D_ϵ^t is the turbulent diffusion of turbulent kinetic energy dissipation rate, D_ϵ^υ is the diffusion of turbulent kinetic energy dissipation rate due to viscous action, P_ϵ is the production of turbulent kinetic energy dissipation rate, and ϕ_ϵ is the destruction term of the turbulent kinetic energy dissipation rate.

Now, all the terms on the right hand side of Eq.2.16 need to be modeled. This introduces too much uncertainty in the modeled ϵ equation, presenting the first major weakness of turbulence modeling using this approach. The modeled term by term equations for ϵ according to Hanjalic and Launder [93] are given in Eqs.2.17 to 2.19.

$$\left(D_\epsilon^t\right)_m = \frac{\partial}{\partial x_j}\left(\frac{\upsilon_t}{\sigma_\epsilon}\frac{\partial \epsilon}{\partial x_j}\right) \tag{2.17}$$

$$\left(P_\epsilon\right)_m = -C_{\epsilon 1}\frac{\epsilon}{k}\overline{u_i u_j}\frac{\partial U_i}{\partial x_j} \tag{2.18}$$

$$\left(\phi_\epsilon\right)_m = C_{\epsilon 2}\frac{\epsilon^2}{k} \tag{2.19}$$

Equation 2.20 gives the modeled turbulent kinetic energy dissipation rate.

$$\left(\frac{D\epsilon}{Dt}\right)_m = \left(D_\epsilon^t\right)_m + D_\epsilon^\upsilon + \left(P_\epsilon\right)_m - \left(\phi_\epsilon\right)_m \tag{2.20}$$

Specific dissipation rate of kinetic energy

The specific rate of dissipation of kinetic energy ω, can be defined as the rate at which turbulent kinetic energy is dissipated per unit of turbulent kinetic energy, and $\omega = \epsilon/k$. By performing an ϵ to ω transformation on the ϵ equation, the exact equation for ω can be obtained. Details of this transformation can be found in [65, 69]. However, Wilcox [58] modeled the turbulence dissipation rate term directly by using the ω scale. It is known that using ω as the second scale in the two-equation models, makes the solution of the ω-equation sensitive to the free stream value of ω [64, 65]. This sensitivity has been blamed on the absence of the cross-diffusion term that would arise in the case of a direct ϵ to ω transformation. The effect of adding the cross diffusion into the turbulent diffusion terms of the ω-equation is to reduce the net production of turbulent kinetic energy. Wilcox [87] reasoned that it is more direct to remove the cross diffusion from the ω-equation and add it directly to the k-equation. This makes solutions of the resulting equations a lot easier as numerical solutions are far more difficult with the cross diffusion added. Furthermore, the cross diffusion term appears only because the transformation begins from the ϵ-equation. To argue that the cross diffusion is missing from the ω-equation as some authors have done [61,63,69,78] assumes that the modeled ϵ-equation is more fundamental than the modeled ω-equation.

The turbulent diffusion, D^t_ω, the production, P_ω, the destruction, ϕ_ω, and the viscous diffusion, D^v_ω, of the turbulent kinetic energy specific dissipation rate, as formulated by Wilcox [58], are given in Eqs.2.21 to 2.24.

$$\left(D^t_\omega\right)_m = \frac{\partial}{\partial x_j}\left(\frac{\upsilon_t}{\sigma_\omega}\frac{\partial \omega}{\partial x_j}\right) \tag{2.21}$$

$$(P_\omega) = -\alpha \frac{\omega}{k} \overline{u_i u_j} \frac{\partial U_i}{\partial x_j} \tag{2.22}$$

$$(\phi_\omega)_m = \beta \omega^2 \tag{2.23}$$

$$(D_\omega^v)_m = \frac{\partial}{\partial x_j} \left(\nu \frac{\partial \omega}{\partial x_j} \right) \tag{2.24}$$

Finally, the modeled equation for the specific turbulent kinetic energy dissipation rate is given by Eq.2.25.

$$\left(\frac{D\omega}{Dt} \right)_m = \left(D_\omega^t \right)_m + (D_\omega^v)_m + (P_\epsilon)_m - (\phi_\omega)_m \tag{2.25}$$

2.2 Turbulence models

There are two approaches to the solution of the now closed transport equations. The first approach involves direct solution of the comprehensive, modeled, second-order-averaged governing equations for $\overline{u_i u_j}$, k, and ϵ, commonly referred to as the Reynolds-stress model (RSM) approach. However, to save on the computational effort, several simplified versions of the RSM, that are devised by guessing the relationship between the Reynolds shear stresses and the strain rate, (for example, the Boussinesq eddy viscosity approximation, Prandtl mixing length model, etc.), form the second solution approach.
A summary of the selected models relevant to this study and which utilize both approaches is given in sections 2.2.1 to 2.2.5.

In addition to the continuity and the momentum transport equations given in Eq.2.4 and 2.5 respectively, all the models solve the extra equations that result from modeling of the various transport processes presented in section 2.1.

2.2.1 Reynolds stress model

The differential equations for $\overline{u_i u_j}$ and ϵ, as given in Eqs.2.12 and 2.20, respectively, are solved together with the definition of k given in Eq.2.26.

$$k = \frac{1}{2}\overline{u_i u_i} \tag{2.26}$$

Equation 2.27 gives the relationships for the turbulent eddy viscosity, and the resulting model constants obtained using the procedures in [89, 91, 94].

$$\begin{aligned} &\upsilon_t = C_\mu \frac{k^2}{\epsilon} \\ &C_\mu = 0.09, \sigma_k = 0.82, \sigma_\epsilon = 1.0, C_{\epsilon 1} = 1.44, \\ &C_{\epsilon 2} = 1.92, C_1 = 1.8, C_2 = 0.60 \end{aligned} \tag{2.27}$$

2.2.2 Standard $k - \epsilon$ model

The standard $k - \epsilon$ model as proposed by Launder and Spalding [95] is based on the solution of Eqs.2.15 and 2.20, for k and ϵ, respectively. The relationship between the Reynolds shear stresses and the velocity field is given through the first order differential Boussinesq approximation (Eq.2.6), that is much cheaper to handle in terms of computational cost. The resulting model constants that are experimentally obtained [57, 95], and the definition of eddy viscosity are given in Eq.2.28.

$$\begin{aligned} &C_\mu = 0.09, \sigma_k = 1.00, \sigma_\epsilon = 1.3, C_{\epsilon 1} = 1.44, C_{\epsilon 2} = 1.92 \\ &\upsilon_t = C_\mu \frac{k^2}{\epsilon} \end{aligned} \tag{2.28}$$

2.2.3 Realizable $k - \epsilon$ model

The standard $k - \epsilon$ model performs quite well for boundary layer flows but not so for flows with a high mean shear rate or a massive separation, because in these cases, the eddy viscosity is over-predicted by the standard eddy

viscosity formulation. In addition, the standard $k-\epsilon$ model dissipation rate equation does not always give the appropriate length scale for turbulence. In order to improve the ability of the $k-\epsilon$ model to predict complex turbulent flows, these deficiencies should be removed.

By combining the eddy viscosity model for Reynolds stresses as given in the Boussinesq approximation (Eq.2.6), and the definition of eddy viscosity as given by Eq.2.28, it is a straight forward matter to show that Eq.2.29 imposes a condition when the normal stresses $\overline{u^2}$ becomes negative.

$$\frac{k}{\epsilon}\frac{\partial U}{\partial x} > \frac{1}{3C_\mu} \approx 3.7 \tag{2.29}$$

Thus, for large mean shear strain rate, $\partial U/\partial x$, the eddy viscosity model becomes non-realizable since the normal stresses cannot have a negative value. Furthermore, the existence of the Reynolds stresses, $-\rho\overline{u_i u_j}$, require that the turbulent fluctuating velocities, u_i and u_j, be correlated. This physical requirement is expressed in the Schwarz inequality [96], which for shear stresses is given in Eq.2.30.

$$\begin{aligned} &\overline{u_i^2} \geq 0 \qquad\qquad (i = 1,2,3) \\ &\frac{\overline{u_i u_j}^2}{\overline{u_i^2 u_j^2}} \leq 1 \qquad (i = 1,2,3 \quad j = 1,2,3) \end{aligned} \tag{2.30}$$

Realizability of the conditions imposed by Eqs.2.29 and 2.30 can thus, only be met by making the model constant, C_μ, a variable that is related to the mean shear strain rate. Reynolds [97] and Shih et al. [98] have proposed a modification of the model constant, C_μ, (Eq.2.31), and the dissipation rate equations, ϵ, (Eq.2.32), to ensure physically realistic flows at all times in their realizable $k-\epsilon$ model. The k and υ_t equations are the same as those of the standard $k-\epsilon$, given in Eqs.2.15 and 2.28, respectively.

$$C_\mu = \frac{1}{A_0 + A_s U^* k/\epsilon} \tag{2.31}$$

$$\frac{D\epsilon}{Dt} = \frac{\partial}{\partial x_j}\left(\left(\frac{\upsilon_t}{\sigma_\epsilon} + \upsilon\right)\frac{\partial \epsilon}{\partial x_j}\right) + C_1 S\epsilon - C_2 \frac{\epsilon^2}{k + \sqrt{\upsilon\epsilon}} \tag{2.32}$$

The auxiliary relations and the model constants, that result from these approximations, are given in Eq.2.33.

$$\begin{aligned}
&U^* = \sqrt{S_{ij}S_{ij} + \tilde{\Omega}_{ij}\tilde{\Omega}_{ij}}, && A_s = \sqrt{6}\cos\phi \\
&\tilde{\Omega}_{ij} = \Omega_{ij} - 2\epsilon_{ijk}\omega_k, && \phi = \frac{1}{3}\cos^{-1}(\sqrt{6}W) \\
&\Omega_{ij} = \overline{\Omega}_{ij} - \epsilon_{ijk}\omega_k, && W = \frac{S_{ij}S_{jk}S_{ki}}{\tilde{S}^3} \\
&S = \sqrt{S_{ij}S_{ij}}, && C_1 = \max\left[0.43, \frac{\eta}{\eta+5}\right], \quad \eta = S\frac{k}{\epsilon}
\end{aligned} \tag{2.33}$$

$$C_2 = 1.9, \sigma_k = 1.00, \sigma_\epsilon = 1.2, C_{\epsilon 1} = 1.44, C_{\epsilon 2} = 1.92, A_0 = 4.0$$

The mean strain rate S_{ij}, and the mean rate of rotation tensor are given in Eq.2.34.

$$S_{ij} = \frac{1}{2}\left(\frac{\partial U_j}{\partial x_i} + \frac{\partial U_i}{\partial x_j}\right) \qquad \Omega_{ij} = \frac{1}{2}\left(\frac{\partial U_i}{\partial x_j} - \frac{\partial U_j}{\partial x_i}\right) \tag{2.34}$$

2.2.4 Standard $k-\omega$ model

The standard $k-\omega$ model, also known as the Wilcox $k-\omega$ model, was developed by Wilcox [58, 87, 99] basically to resolve the shortcomings of the $k-\epsilon$ model in predicting APG and separated flows, as discussed in section 1.3.2. He has recently modified the equations for ω (Eq.2.25) and k (Eq.2.36), to include the damping of the standard turbulent viscosity (Eq.2.35), for low Reynolds number flows in the viscous sub-layer through the closure coefficient α^* and β^*, respectively, as given in Eq.2.37.

$$\upsilon_t = \alpha^* \frac{k}{\omega} \tag{2.35}$$

$$\frac{Dk}{Dt} = \frac{\partial}{\partial x_j}\left(\left(\frac{\upsilon_t}{\sigma_k} + \upsilon\right)\frac{\partial k}{\partial x_j}\right) - \overline{u_i u_j}\frac{\partial U_i}{\partial x_j} - \beta^*\omega k \tag{2.36}$$

$$\alpha^* = \alpha^*_\infty \left(\frac{\alpha^*_0 + Re_t/R_k}{1 + Re_t/R_k} \right)$$
$$\beta^* = \beta^*_i f_{\beta^*} \tag{2.37}$$

Where $Re_t = \rho k/\mu\omega$, is the turbulent Reynolds number. The resulting extra relations are given in Eq.2.38

$$\alpha^*_0 = \frac{\beta_i}{3}, \qquad f_{\beta^*} = \begin{cases} 1, & \chi_k \leq 0 \\ \frac{1+680\chi_k^2}{1+400\chi_k^2}, & \chi_k > 0 \end{cases} \tag{2.38}$$
$$\beta^*_i = \beta^*_\infty \left(\frac{4/15 + (Re_t/R_\beta)^4}{1 + (Re_t/R_\beta)^4} \right), \quad \chi_k = \frac{1}{\omega^3} \frac{\partial k}{\partial x_j} \frac{\partial \omega}{\partial x_j}$$

In the ω-equation (see Eq.2.25), the low-Reynolds number correction in the production term is done through modification of the parameter α, while the vorticity in the destruction term is introduced through modification of parameter β, respectively, as given in Eq.2.39.

$$\alpha = \frac{\alpha_\infty}{\alpha^*} \left(\frac{\alpha_0 + Re_t/R_\omega}{1 + Re_t/R_\omega} \right) \qquad \beta = \beta_i f_\beta \tag{2.39}$$

Equation 2.40 gives the model constants and the supplementary relations.

$$\beta = \frac{1 + 70\chi_\omega}{1 + 80\chi_\omega} \qquad \chi_\omega \equiv \left| \frac{\Omega_{ij}\Omega_{jk}S_{ki}}{(\beta^*_\infty \omega)^3} \right|$$
$$\alpha^*_\infty = 1, R_k = 6, \beta_i = 0.072, \alpha_0 = \frac{1}{9}, \alpha_\infty = 0.52, \sigma_k = 2, \sigma_\omega = 2 \tag{2.40}$$
$$(\alpha_\infty\text{=1 at high Re}), R_\omega = 2.95, R_\beta = 8, \beta^*_\infty = 0.09,$$

The three coefficients, R_β, R_k, and R_ω control the rate at which the closure coefficients approach their fully turbulent values and are usually adjusted.

One of the major advantages of the Wilcox $k-\omega$ model is its ability to compute the k and ω transport equations in the near wall region without the use of any damping functions. The exact solution of ω in the viscous sub-layer is

$$\omega = \frac{6\upsilon}{\beta y^2} \qquad \text{for} \quad y^+ < 2.5 \tag{2.41}$$

So at the wall when $y = 0$, then ω_w goes to infinity. This is an awkward situation from a numerical view point! To by-pass this singularity problem, Wilcox [58] modified the near wall modeling of ω, (Eq.2.42), to match the asymptotic behavior of the laminar sub-layer (up to $y^+ \approx 30$), and of the logarithmic region ($y^+ > 60$), as given in Eqs.2.43 and 2.44, respectively.

$$\omega = \frac{(u^*)^2}{\nu}\omega^+ \tag{2.42}$$

$$\begin{aligned} \omega^+ &= \min\left(\omega_w^+, \frac{6}{\beta_\infty^*(y^+)^2}\right) \qquad \omega_w^+ = \begin{cases} \left(\frac{50}{k_s^+}\right)^2 & k_s^+ < 25 \\ \frac{100}{k_s^+} & k_s^+ \geq 25 \end{cases} \\ k_s^+ &= \max\left(1.0, \frac{\rho k_s u^*}{\mu}\right) \qquad k_s \text{ is the roughness height} \end{aligned} \tag{2.43}$$

$$\omega^+ = \frac{1}{\sqrt{\beta_\infty^*}}\frac{du_{\text{turb}}^+}{dy^+} \tag{2.44}$$

leading to the value of ω in the wall cell being modeled as;

$$\omega = \frac{u^*}{\sqrt{\beta_\infty^*}\kappa y} \tag{2.45}$$

The wall boundary conditions for the k-equation are treated in the same way as the k-equation in $k-\epsilon$ models using a two-layer model approach discussed in section 2.2.6.

2.2.5 SST $k-\omega$ model

The philosophy behind the SST $k-\omega$ model, developed by Menter [65], is that it blends the strengths of the $k-\epsilon$ and the $k-\omega$ models. In the near wall region, the $k-\omega$ model is used since it does not require any wall damping functions nor the computation of wall distances, and the equations are less

stiff. However, in the outer layer, the $k-\omega$ model has to be abandoned due to its sensitivity to the free-stream values of ω in favor of the $k-\epsilon$ model.

Johnson and King [81], and Driver [100] have shown that in APG flows, the important effects of the transport of the principal stresses, that are not usually considered by both the $k-\epsilon$ and the $k-\omega$ models, can effectively be accounted for by modifying the definition of turbulent eddy viscosity through a blending function F_2 (Eq.2.47). The main effect of switching from $k-\omega$ to $k-\epsilon$, is the inclusion of the cross-diffusion term in the ω equation (Eq.2.46), which it has been argued, enhances production of turbulent kinetic energy. The cross diffusion added in the ω-equation is a direct consequence of ϵ to ω transformation. This switching is facilitated by modification of the Prandtl numbers σ_k and σ_ω through the blending function F_1 as in Eq.2.48.

$$\begin{aligned}\frac{D\omega}{Dt} =& \frac{\partial}{\partial x_j}\left(\left(\frac{\upsilon_t}{\sigma_\omega}+\upsilon\right)\frac{\partial\omega}{\partial x_j}\right) - \frac{\alpha}{\upsilon_t}\overline{u_i u_j}\frac{\partial U_i}{\partial x_j} - \beta\omega^2 \\ &+ 2(1-F_1)\sigma_{\omega,2}\frac{1}{\omega}\frac{\partial k}{\partial x_j}\frac{\partial\omega}{\partial x_j}\end{aligned} \tag{2.46}$$

$$\upsilon_t = \frac{k}{\omega}\frac{1}{\max\left[\frac{1}{\alpha^*}, \frac{\Omega F_2}{a_1\omega}\right]}, \quad F_2 = \tanh\left(\phi_2^2\right), \quad \phi_2 = \max\left[2\frac{k}{0.09\omega y}, \frac{500\mu}{\rho y^2\omega}\right] \tag{2.47}$$

The invariant measure of strain rate is $\Omega = \sqrt{2\Omega_{ij}\Omega_{ij}}$ and y is the distance to the nearest wall. The blending function, F_2, is 1 for boundary layer flows, including adverse pressure gradient boundary layers, where the production of turbulent kinetic energy is much larger than its destruction, and is 0 for free shear flows.

$$\begin{aligned}&\sigma_k = \frac{1}{F_1/\sigma_{k1} + (1-F_1)/\sigma_{k2}}, \qquad \sigma_\omega = \frac{1}{F_1/\sigma_{\omega 1} + (1-F_1)/\sigma_{\omega 2}} \\ &\phi_1 = \min\left[\max\left(\frac{\sqrt{k}}{0.09\omega y}, \frac{500\mu}{\rho y^2\omega}\right), \frac{4\rho k}{\sigma_{\omega,2}D_\omega^+ y^2}\right], \quad F_1 = \tanh\left(\phi_1^4\right)\end{aligned} \tag{2.48}$$

In the sub-layer where $k-\omega$ is accurate, the blending function F_1, is designed to be 1, while in the wake region ($y^+ > 70$), where $k-\epsilon$ is accurate, it takes a value of 0. The cross diffusion into both k and ω equations of the $k-\omega$ model is introduced through the parameter D_ω^+ (Eq.2.49).

$$D_\omega^+ = \max\left[2\frac{1}{\sigma_{\omega,2}}\frac{1}{\omega}\frac{\partial k}{\partial x_j}\frac{\partial \omega}{\partial x_j}, 10^{-20}\right] \tag{2.49}$$

The production of kinetic energy, and, the production and dissipation of the specific dissipation rate, are modeled exactly the same way as in the $k-\omega$ model with the coefficients of the damping functions slightly modified according to the auxiliary relations given in Eq.2.50.

$$\begin{aligned} &f_{\beta^*} = 1, \quad \alpha_\infty = F_1\alpha_{\infty 1} + (1-F_1)\alpha_{\infty 2}, \quad \alpha_{\infty 2} = \frac{\beta_{i2}}{\beta_\infty^*} - \frac{\kappa^2}{\sigma_{\omega 2}\sqrt{\beta_\infty^*}} \\ &f_\beta = 1, \quad \alpha_{\infty 1} = \frac{\beta_{i,1}}{\beta_\infty^*} - \frac{\kappa^2}{\sigma_{\omega 1}\sqrt{\beta_\infty^*}}, \quad \beta_i = F_1\beta_{i1} + (1-F_1)\beta_{i2} \end{aligned} \tag{2.50}$$

Equation 2.51 gives the closure coefficients for the Menter SST $k-\omega$ model.

$$\begin{aligned} &\alpha_\infty^* = 1, R_k = 6, \beta_i = 0.072, \alpha_0 = \frac{1}{9}, \alpha_\infty = 0.52, R_\omega = 2.95 \\ &R_\beta = 8, \beta_\infty^* = 0.09, \sigma_{k1} = 1.176, \sigma_{\omega 1} = 2.0, \sigma_{k2} = 1.0 \\ &\sigma_{\omega 2} = 1.168, a_1 = 0.31, \beta_{i1} = 0.075, \beta_{i2} = 0.0828 \end{aligned} \tag{2.51}$$

2.2.6 Near wall modeling

For flows with severe pressure gradients leading to boundary layer separations, the wall functions approach to modeling near wall turbulence is known to perform poorly [59, 72, 79]. In such cases the traditional two-layer zonal model approach is adopted. The near-wall mesh must be fine enough to be able to resolve the laminar sub-layer (typically $y^+ \approx 1$). The viscosity-affected near-wall region is completely resolved all the way to the viscous sub-layer and the transport equations integrated such that Nikuradse's near

wall velocity distribution is reproduced [57, 87]. In this approach both the turbulent kinetic energy dissipation rate, ϵ, and the turbulent viscosity, υ_t, in the near-wall cells are specified according to the suggestions given by Wolfstein [101], and Chen and Patel [102] (see Eq.2.53). The demarcation of the viscosity-affected region and the fully-turbulent region is determined by a wall-distance-based, turbulent Reynolds number, Re_y, defined as;

$$Re_y \equiv \frac{\rho y \sqrt{k}}{\mu} \tag{2.52}$$

where y is the normal distance from the wall at the cell centers.

In the fully turbulent region ($Re_y > Re_y^*; Re_y^* = 200$), the $k-\epsilon$ models or the RSM (described in sections 2.2.1 and 2.2.2) are employed. Near the wall, in the viscosity-affected region, ($Re_y < Re_y^*$), the momentum and the k equations as described in sections 2.2.1 and 2.2.2 are retained but are solved alongside the new definition of ϵ and υ_t. This approach is applied to the solution of the momentum, and the k equations for the $k-\omega$ model in the viscous sub-layer.

$$\begin{aligned} \upsilon_t &= C_\mu \ell_\mu \sqrt{k}, & \ell_\mu &= y c_\ell \left(1 - e^{-Re_y/A_\mu}\right) \\ \epsilon &= \frac{k^{3/2}}{\ell_\epsilon}, & \ell_\epsilon &= y c_\ell \left(1 - e^{-Re_y/A_\epsilon}\right) \\ c_\ell &= \kappa C_\mu^{-3/4}, & A_\mu &= 70, \quad A_\epsilon = 2c_\ell \end{aligned} \tag{2.53}$$

Chapter 3

Apparatus and Instrumentation

3.1 Fan test facility

Stationary air was drawn from the atmosphere by an inlet radial flow fan. It was passed through a 1.9 m long, rectangular-circular transition duct, which was connected, to a 600 mm inner diameter, 3.7 m long circular duct. A 1 m long circular to rectangular transition duct transferred the air to a 400 m x 100 mm x 1 m long straight inlet duct before its entry into the diffuser proper. This inlet duct geometry was maintained constant for all the diffusers tested in this study. The transition and circular ducts were manufactured from 1.2 mm thick mild steel plates. After flowing through the diffuser, the air was discharged back into the atmosphere. The fan was powered through a 5.5kW variable speed dc motor. Figure 3.1 shows the line diagram layout of the flow facility while figure 3.2 shows a pictorial view of the facility.

The diffuser was of plane wall, two-dimensional geometry with the roof and floor walls being parallel to each other. The two sidewalls were divergent. To ensure two-dimensionality of the flow, the distance between the roof and the floor at the inlet and exit was maintained constant at 400 mm. By measuring the distance between the roof and the floor of the diffuser at several locations, the overall error in parallelism was ± 0.25 mm.

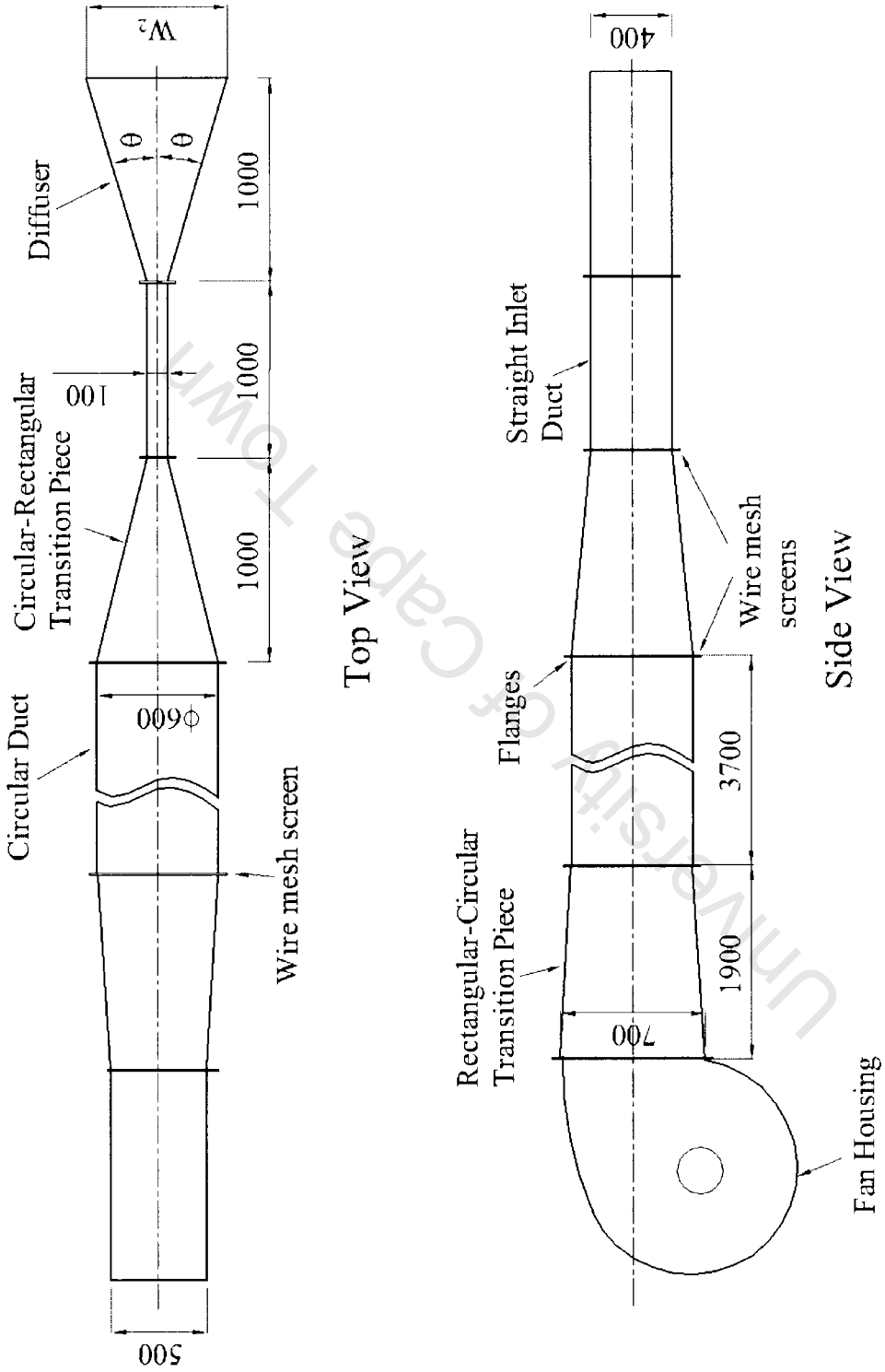

Figure 3.1: Line layout of the experimental apparatus

Figure 3.2: Pictorial view of the experimental apparatus

Further, the distances between the left and right walls at both entry and exit of the diffusers were measured. This was done at the roof, the center plane and the floor. The half divergence angles θ, based on these measurements were 24.88°, 20.3°, 14.5°. All the plates for the straight inlet duct and diffuser were machined from 10 mm thick transparent thermoplastic resin (Perspex).

At the diffuser entry, the edges of the entry duct side plate and diffuser entry side plate were machined at appropriate angles to form the required divergence angles on assembly. These side plates were joined by use of chloroform, and the sharp edges at the entry corners were smoothened very carefully using a fine file and sand paper to form the diffuser corner assembly whose details are shown in figure 3.3.

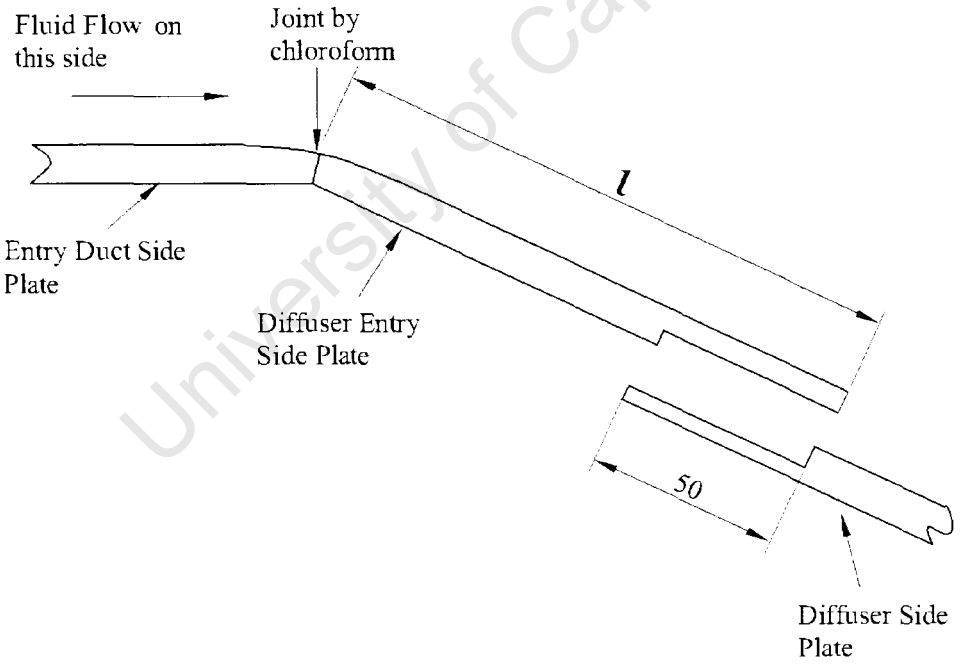

Figure 3.3: Entry corner assembly details

The edges were machined using a milling machine to an accuracy of ±0.25°. Linear accuracy for all the lengths was ±0.01 mm.

One of the main objectives of this study was to check the effect of various flow parameters due to a change in the divergence angle. In this regard, three pairs of diffuser entry side plate were machined to correspond to the various half divergence angles θ, i.e. 15°, 20° and 25°. These were then fitted in turn to the facility.

It was desired to carry out the experiments at a constant axial length of 1000 mm from the diffuser geometric entry. The lengths of the corner plates were therefore varied to maintain a constant axial length to width ratio N/W_1 of 10 for the three diffusers tested in this study. The diffuser side plate was 903 mm long. Consequently, only the length marked 'ι' in figure 3.3 needed to be varied. A summary of the geometry of the diffuser is given in table 3.1.

Table 3.1: Dimensions for corner assembly side plates

$\theta_{design}(^\circ)$	ι(mm)	N(mm)	$\theta_{actual}(^\circ)$	$\theta_{Error}(^\circ)$	N_{Error} (mm)
15	181	999.7	14.5	-0.5	-0.3
20	210	999.8	20.3	+0.3	-0.2
25	249	1000.3	24.88	-0.12	+0.3

The roof and floor plates were attached to the side plates by cap screws. Grease was applied to the edges of the side plates to ensure that no leakage took place through the interfaces after assembly. To stabilize the flow, wire mesh screens of 0.9 mm wire thickness, 3.3 mm square eye and 6 holes per square centimeter were installed at the rectangular-circular transition duct exit, circular duct-transition duct interface, and transition piece-entry duct interface. Vibration effects were isolated from the duct facility by using 12 mm foam gaskets installed between the flanges at all interfaces. Further, both the circular and transition ducts were anchored to the floor. This ensured

that, no significant vibrations from the fan were transmitted to the diffuser.

Before the diffuser was bolted to the straight inlet duct, velocity profile measurements showed that the flow at the exit of this duct was symmetrical about the x axis in both the y and z directions. However, it is known that once the diffuser is connected to the straight duct, the presence of a stall in the diffuser distorts the velocity profile at the exit of the straight duct (see figure 6.1). This distortion is dependent on the Reynolds number and the diffuser divergence angle [11, 17, 18, 26]. It was desired to measure the reference flow parameters at a location where this distortion was absent, and hence an arbitrary upstream location in the straight duct, $x/W_1 = -2.35$, where these flow conditions were met, was chosen as a suitable flow reference location. After installation of each diffuser, the velocity profiles were measured again at the reference location by use of hot-wire anemometry and were found to be uniform with an average boundary layer thickness, δ, of 5 mm corresponding to an inlet blockage factor, $B \approx 0.015$. This point is henceforth considered as the diffuser reference point upon which the reference inlet centerline velocity $U_{ref} \equiv U_1$ was measured.

At the reference point, eight static pressure holes of 1.8 mm diameter, were drilled, two on each side of the duct. Due to the manufacturing difficulties of drilling the 1.8 mm holes at the exact diffuser entry, a similar set of eight holes were drilled at a location 2 mm upstream of the diffuser entry. This is the point at which the entry static pressure, P_1, was measured. The static pressure P_1 was used as the reference inlet pressure against which pressure recovery values at points along the sidewall, $P_x - P_1$, were evaluated. Small brass tubes, 20 mm long, and of 1.8 mm and 1 mm outer and inner diameters respectively, were inserted into the static pressure holes. The tubes were completely flush with the inner surface of the side plates. This

was achieved by ensuring that they pressed against a polished flat mild steel bar held against the side plates from inside the duct. A fast setting adhesive (super glue) was used to secure the tubes in position. Air was then blown through the tubes to ensure that no blockage had taken place. The same treatment was given to all the other static pressure tubes inserted into the test section.

The static pressures at the reference location and at the diffuser entry were averaged by connecting the eight tubes, to a common ring tube through 1.5 mm flexible vinyl tubing, at each of the two locations. The output of the common ring tube at the reference point was used as the reference pressure, P_{ref}, in all the experiments while the output of the ring tube at the diffuser entry was the inlet static pressure, P_1. A port for the insertion of an L-shaped Pitot tube and the hot-wire anemometer from the sidewall was provided at the reference point for measurement of the centerline reference dynamic pressure, P_{D1}, hence U_1, and the velocity profiles. A traverse mechanism with a lead screw thread attached to the diffuser stand frame was used to move the L-shaped hot-wire anemometer probe in the lateral direction, (along y-axis).

On each side plate of the inlet duct-diffuser assembly, 60 static pressure holes, and hence a total of 120 pressure holes for both sides, were drilled. The locations of the tapings were as indicated in table 3.2. Attention was paid to the locations near the entry of the diffuser where very high pressure gradients due to separation and sudden changes of flow directions were expected. In this region, the pressure holes were spaced at 5 mm intervals. This spacing increased progressively to 10, 20 and 50 mm in the downstream direction.

A Scanivalve pressure scanner with 48 pressure ports was used to scan the static pressures on the diffuser side walls, and the total pressure at the reference point. The static pressure tubes and the output of the common ring

Table 3.2: Location of static pressure holes

Zone	Intervals (mm)	No. of holes
$-3 < x/W_1 < -0.5$	50	6
$-0.5 < x/W_1 < 0.5$	5	19
$0.5 < x/W_1 < 1$	10	5
$1 < x/W_1 < 5$	20	20
$5 < x/W_1 < 10$	50	10

tube at the diffuser entry, P_1, were connected to ports 1-47 of the scanner. This meant that three runs were required, in order to take measurements of all the 120 static pressure ports on the diffuser sidewalls for any given inlet flow Reynolds number. The total pressure Pitot tube was connected to port 48 of the scanner, and hence the dynamic pressure, P_{D1}, for any run could be established. The dynamic pressure determined from the total and static pressures measured at the flow reference point for each run was then used to normalize all the static pressures measured for that run. Therefore, any errors in the coefficient of pressure recovery that could result from changes in flow and atmospheric conditions were minimized.

The roof of the diffuser was constructed from six. 150 mm wide strips and two strips of widths 15 mm and 85 mm installed as first and last strip at the entry and exit of the diffuser respectively. Thus, the total axial length of the diffuser remained constant at 1m for all the tests carried out. The dimensions of each strip were based on its position along the diffuser axial length as shown in figure 3.4. The origin of the cartesian coordinate system used in this research was at the center of the diffuser entry plane. All the strips were made from 10 mm Perspex and were reinforced with 25 mm aluminium square tubes. A 150 mm wide Perspex probing strip was used to

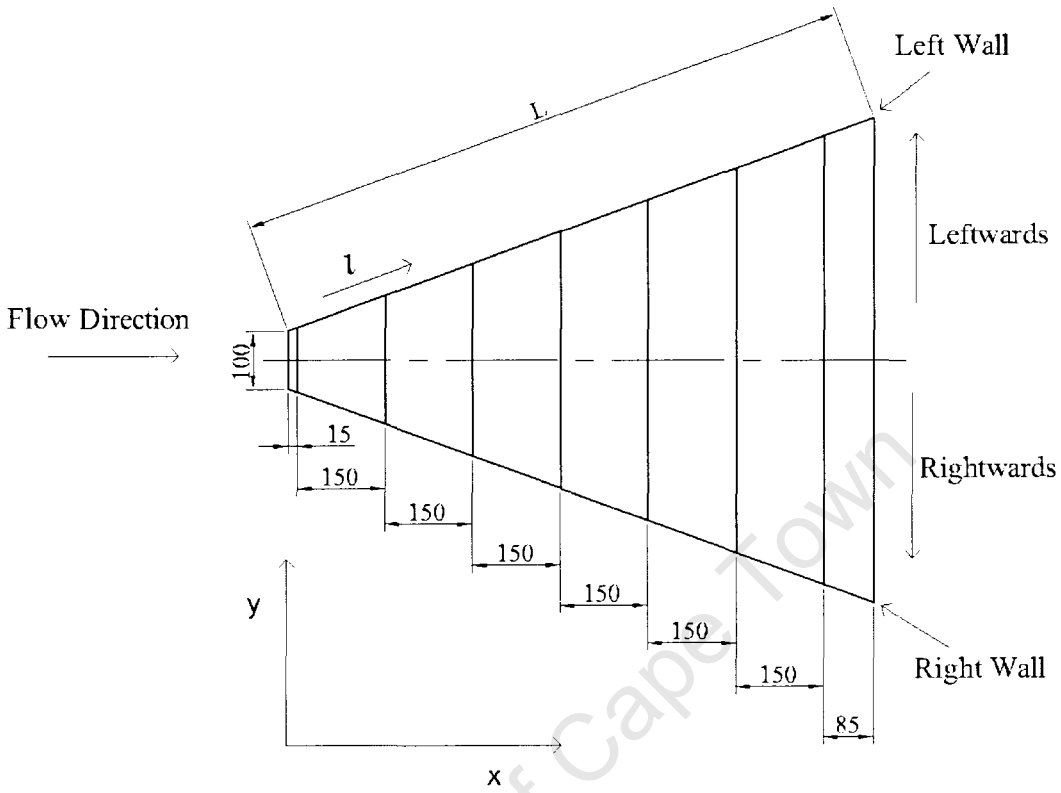

Figure 3.4: Geometry of the diffuser roof and convention for the diffuser

move a 3-tube yaw meter in the y direction for measuring the velocity profiles in the diffuser test section. This strip was 2 m long and 10 mm thick, and was also reinforced with a 25 mm aluminium square tube. The probing strip was long enough to ensure that the roof remained covered at all times, at any section, during the probing between the left and the right sidewalls. All the 150 mm roof strips were removed in turn and replaced with the probing strip. Velocity profiles were then measured at 150 mm intervals in the x direction.

A very robust mechanism was required to move the probing strip in the lateral direction. Since small spatial variations in the lateral direction, were not desired, movement of the probing strip was done manually. The yaw meter location was established by using a scale attached to the neighboring strips. All locations were measured either positive or negative relative to the

centreline when probing was to the right or left respectively. This convention was based on an observer viewing the diffuser from the entry plane along the flow as shown in figure 3.4. A lead screw on the yaw meter mechanism was used to vertically traverse the probe between the roof and floor.

3.2 The cluster of inlet vanes

The vanes were designed according to the design criteria of Cochran and Kline [4]. They were manufactured from 0.5 mm thick stainless steel plates. Each plate was of length 250 mm and width 400 mm. The passages were formed by spacing the plates at both ends along four 5 mm threaded lead screws, two on each end, such that the opening angles α, of the resulting passages were between $7.5° - 10°$. The plates were locked in position on the lead screws by use of thin lock washers from both sides of the plates. The angles of the passages and the number of vanes could thus be freely varied. The cluster of vanes was then positioned at the diffuser inlet. A tight fit between this cluster and roof/floor ensured that the vanes remained in position during experiments. Table 3.3 is a summary of the dimensions of the vanes for the different diffuser angles based on the notation given in figure 3.5.

Table 3.3: Dimensions for the vane clusters

$\theta(°)$	**No. of vanes**, n	**Length**, c (mm)	**Spacing**, a (mm)	a/b	$\alpha(°)$
15	3	250	25	1	7.5
20	4	250	20	1	8
25	4	250	20	1	10

Figure 3.6 shows the cluster of vanes installed at the diffuser entry.

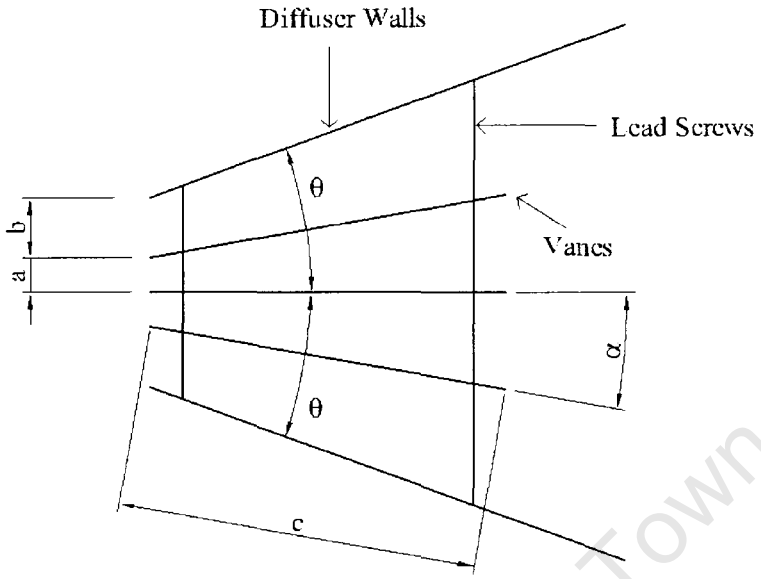

Figure 3.5: Notation for the vane design

3.3 Instrumentation

3.3.1 Pressure measurements

Pressure scanner

A 48-port Scanivalve pressure-sampling scanner was used for measuring multiple pressures in conjunction with a reluctance pressure transducer. The rotor of the Scanivalve, through which stepping of the measurement ports was achieved, was driven by a solenoid. The rotational speed of the rotor was varied through a solenoid controller. The position of the rotor was tracked using an optical emitter transmitting to an odd/even decoder whose binary digital number was displayed on a screen and also read through a computer. The maximum sampling rate for the scanner was 200 readings per second, even though data was sampled at a frequency of 0.1 Hz to allow enough settling time for the air in the thin, long vinyl pressure transmission tubes.

A portable precision pneumatic calibrator was used to check for external

Figure 3.6: Facility with vanes installed

leakages. Vinyl tubes were connected to the pneumatic connector of the Scanivalve and through the calibrator a pressure of 0.5 bar was applied for 10 minutes to each port. The maximum pressure drop corresponded to an 11.4% drop in pressure per hour. This was within the acceptable range stated by the manufacturer of 20.8% drop in pressure per hour. Leakages at the vinyl tube connections, were further checked by using a syringe to inject soapy water into the tubes and observing the formation of any bubbles. No leakages were observed and in any case, the actual experiments were conducted at pressures well below 0.1 bar.

Pressure transducer

All the pressures were measured by use of a 0-625 Pa full range reluctance pressure transducer described in appendix B. Self-contained electronics provided a conditioned linearized 0-5 Vdc output, V_{tra}. The accuracy of the transducer was specified by the manufacturer as 1.5% full scale (best fit

straight line), which included non-linearity, hysteresis and non-repeatability. The low-pressure port of the transducer was connected to the output of the common ring tube at the diffuser reference location, P_{ref}, while the high-pressure port was connected to the output of the Scanivalve pressure scanner. Calibration of the transducer, (see appendix B), was carried out in a low-turbulence intensity (0.4%) wind tunnel against an inclined alcohol manometer. The linearity of the manometer calibration was found to be within 1.1% of the manufacturer's specification. Accordingly, the calibration equation, (Eq.3.1), was used to compute all the differential pressures measured by the transducer. Data was sampled at a frequency of 100 Hz and hence 1000 readings were averaged at one pressure port before the scanner stepped to another port.

$$P_x - P_{ref} = 124.6 V_{\text{tra}} \tag{3.1}$$

Three-tube yaw meter

A yaw meter (also known as a 'cobra probe') combines the means for simultaneous measurement of total pressure, dynamic pressure, and flow direction by one instrument. It can be made of multiple tubes ranging between 3 and 7. The most common though are either a 3-tube yaw meter, for two dimensional flow measurements, or a 5-tube yaw meter, for three-dimensional measurements. For this two-dimensional flow study, a 3-tube yaw meter was used.

The method by which a yaw meter is rotated locally to determine the flow direction sensed when the off-center pressures, P_l and P_r (figure 3.7 (a)) balance out, is known as the null-reading method. At this position of pressure balance, the central total head tube, P_c, then measures the local total pressure. Achieving this null-position for the low pressure regime of this

research was extremely cumbersome. However, this experimental difficulty

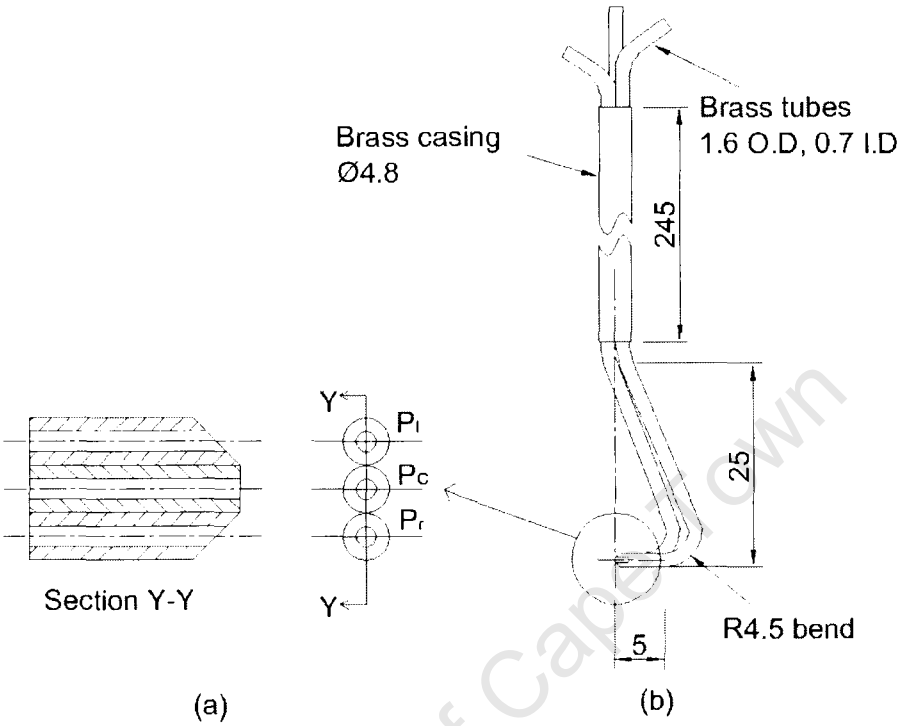

Figure 3.7: The 3-tube yaw meter

was overcome by a probe calibration method based on the determination of probe rotational sensitivity in terms of non-dimensional calibration parameters which make the calculation of local velocity components possible, therefore eliminating the need to rotate the probe at the measurement site. Furthermore, inaccuracies in probe construction, which produce errors with the null-reading technique, are accounted for by calibration. The calibration parameters could then be read off pre-mapped calibration charts given in appendix B. Considering the enormous amount of data that is required to capture the complete velocity and static pressure fields in this study, this process was made simpler by the use of calibration equations as will be discussed shortly.

The bent shape of the probe was constructed by soldering together 3

brass tubes of 0.7 mm and 1.6 mm inner and outer diameters, respectively. Bending of the tubes was done in such a manner that the tube openings were on the same plane as the vertical axis of their orientation. This design allowed up to 360° rotation of the yaw meter about the yaw axis without altering the measurement location, a design feature of particular use in this study. The probe consisted of a forward facing Pitot-tube at the center and two chamfered side tubes at a chamfer angle of 45° in the horizontal plane as shown in figure 3.7. The tubes were contained in a 4.8 mm internal diameter brass casing that was 245 mm long.

Orientation mechanism

Figure 3.8 shows the orientation mechanism used for measuring the velocity profiles. It was composed of a lead screw 335 mm long and 1.75 mm pitch. The lead screw had a central through hole along its axis to accommodate the probes in their casing. A vertical adjustment wheel with a threaded through hole was attached to the support bracket by a collar bolted to the top of the support bracket. The lead screw was held rigidly in the guide block by grub screws on one end, and to the protractor on the other end. The guide block was sandwiched between the legs of the support bracket and was able to slide along the legs. The vertical movement of the probe casing, together with the probes, was guided by three bushes. The first bush was fitted at the bottom of the lead screw, the second one in a cylindrical guide on the base plate, and the third one at the protractor pointer arm. The edge of the protractor, against which a rubber bush pressed, was straight knurled. The rubber bush pressed against the protractor through a knob held at the protractor arm. By turning this knob, the arm could be rotated around the protractor. Since the only place the probe casing was rigidly held was at the protractor arm,

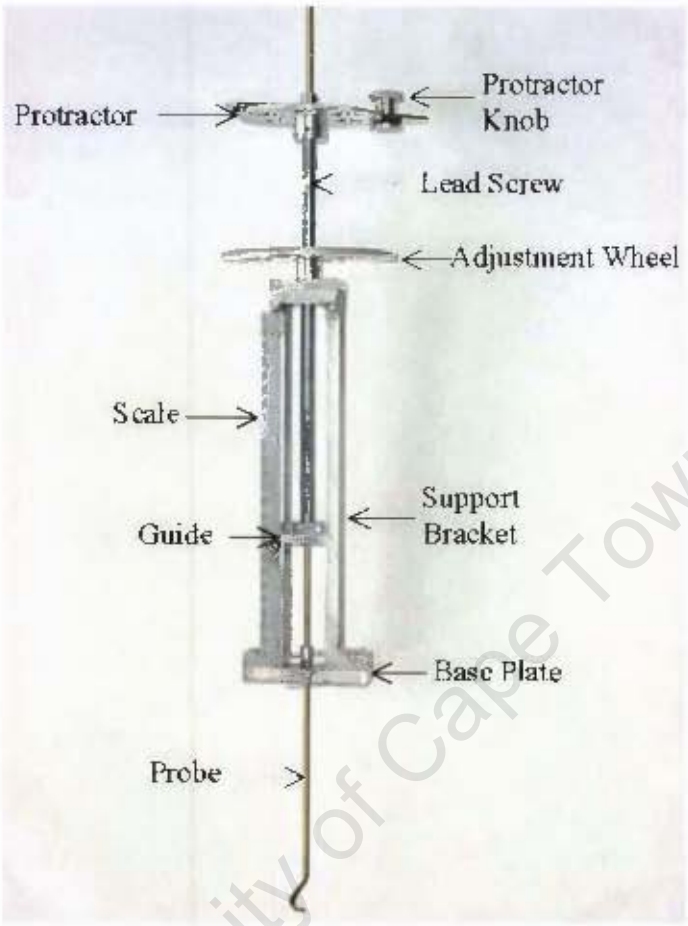

Figure 3.8: Yaw meter orientation mechanism

rotating the arm resulted in rotation of the probe.

The yaw angle given to the probe was read at the calibrated protractor. The protractor had a resolution of 1°. The yaw angle was thus read to an angular accuracy of ±0.5°. The lead screw, the guide block, the probe, the protractor and the protractor pointer arm could all be moved up or down when the vertical adjustment wheel was turned. The vertical position was determined by reading off the scale attached to the support bracket to an accuracy of ±0.5 mm. The whole assembly was attached to a base plate, which was in turn bolted to the aluminium reinforcement on the probing strip.

hence placing the orientation mechanism out of the flow field and therefore introducing no blockage effects or disturbance to the flow. Two yaw meters were manufactured to measure the flow-field, one at the diffuser reference location, and the other at the test section. Figure 3.9 shows a pictorial view of the flow facility with the the two yaw meters in place.

Figure 3.9: Flow facility with yaw meters

3.3.2 Inlet velocity measurements

Inlet velocity profiles and turbulence intensities were measured by use of a TSI constant temperature linearized anemometer (CTA). The sensor was a fine wire made of 5-micron platinum coated tungsten welded to L-shaped gold plated stainless steel needles that were mounted on a probe support. With this arrangement, the sensor was upstream of the probe to minimize upstream flow disturbance caused by the probe support. The probes were

built with a plug-type connector to fit to a probe support, thus providing an electrical connection to the anemometer electronics. The probe support was connected to the anemometer through a 1.9 m long tri-axial cable. The sensor was set to operate on a 5:1 bridge ratio with a control resistance of 64Ω. The probe support was 0.5 m long. The linearizer voltage output was accurate to within ±0.5%.

The anemometer was calibrated in a 0.4% turbulence intensity wind tunnel flow field against a Pitot-static tube connected to the reluctance pressure transducer. Equation 3.2 shows the linearized equation used for velocity measurements. Based on this equation, the calibration data was linear to within ±0.6%.

$$\tilde{u} = 3.2\tilde{E}_{\text{lin}} \tag{3.2}$$

where $\tilde{u}$ and $\tilde{E}_{lin}$ were the air instantaneous velocity and CTA linearizer outputs, respectively. The rms fluctuating velocity, u' was calculated according to Eq.3.3. Hence, the turbulence intensity could be established.

$$u' = \sqrt{\frac{1}{N}\sum_{i=1}^{N}\left(\tilde{u}_i - \frac{1}{N}\sum_{j=1}^{N}\tilde{u}_j\right)^2} \tag{3.3}$$

where N was the number of readings sampled at a frequency of 10 KHz for 3 seconds. Three sets of readings were taken in time steps of 10 seconds. The mean and the rms fluctuating velocities, and the turbulence intensities were then calculated from the resulting arrays before discarding the arrays ready for the next position.

3.4 Probe steady state calibration

The probe was calibrated against a hot-wire anemometer in a low-turbulence intensity (0.4% turbulence intensity) wind tunnel flow field. The reference

probe null-direction was selected as the direction of the centreline of the probe tip in line with the main flow direction when the pressures recorded from the off-center tubes were equal to each other. At this reference direction, $\psi = 0°$. The pressure measured at the central tube of the probe at this position was the total (stagnation) pressure of the flow, P_t, discussed earlier.

Non-dimensional calibration parameters were calculated in terms of pressures and resultant flow velocity, q, similar to those specified by Yajnik and Gupta [103], Bryer and Pankhurst [104] and Rhagava et al. [105] and given in Eqs.3.4 to 3.6.

$$f(\psi) = \frac{P_l - P_r}{P_c - P_m} \tag{3.4}$$

$$Q_p = \frac{P_c - P_m}{\rho q^2/2} \tag{3.5}$$

$$S_p = \frac{P_t - P_c}{P_c - P_m} \tag{3.6}$$

where P_l and P_r are the pressures sensed by the off-center tubes, $P_m = (P_l + P_r)/2$, is the mean pressure for the off-center pressures, P_c is the pressure measured by the central tube, and P_t is the local total pressure that would be measured by the probe if it were at the null-position. These functions can be established directly and are known to be independent of Reynolds number [106–108]. Thus, once established at one Reynolds number, they can be applied to a range of Reynolds numbers. In this research, calibration of the probe was done at 15 m/s. The resulting charts are presented in appendix B. The pressures from these tubes were recorded by use of the Scanivalve scanner in conjunction with the pressure transducers in the same manner as the wall static pressures were recorded.

For the large number of measurement points, reading the calibration parameters from the charts proved to be tedious. Consequently, the linear portions of the calibration charts were established, and polynomial descriptions of these portions developed so that analysis could be simplified by processing the parameters using a personal computer. The linear portion of the $f(\psi)$ versus ψ chart was found to be between $-1.4 < f(\psi) < 1.26$ which corresponded to $-16° < \psi < 14°$ and was described by Eq.3.7.

$$f(\psi) = 0.0295 + 0.0896\psi \tag{3.7}$$

Within this region, the dynamic pressure, Q_P, and total pressure, S_P calibration parameters both produced a one on one relationship with ψ and were curve fitted using sixth order polynomials given in Eq.3.8.

$$\begin{aligned} Q_P =& 0.6544 + (26\psi - \psi^2)\text{x}10^{-4} - (3\psi^3 - \psi^4)\text{x}10^{-6} \\ & - (7\psi^5 + 3\psi^6)\text{x}10^{-9} \\ S_P =& 0.0079 - (5\psi - 3\psi^2)\text{x}10^{-4} - (\psi^3 + 5\psi^4)\text{x}10^{-6} \\ & + (20\psi^5 + 4\psi^6)\text{x}10^{-9} \end{aligned} \tag{3.8}$$

To avoid a singularity in Eqs.3.4 and 3.6, when $P_c - P_m$ becomes zero, it was ensured that $P_c - P_m$ remained positive. This condition was monitored through the data acquisition software. Negative values of $P_c - P_m$, and hence Q_p, would describe complex imaginary values of the velocity based on Eq.3.5. Values of $f(\psi)$ were also monitored real time so that whenever they were out of range, they would be adjusted accordingly by rotating the probe in the appropriate direction. Thereafter, the flow direction and velocity were established relative to the adjusted probe direction. Finally, the calculated flow direction was transformed so that it was referenced to the geometric null-probe direction.

At a given location, Eqs.3.4 and 3.7 were used to evaluate the yaw calibration parameter, $f(\psi)$, and the yaw angle, ψ respectively. The dynamic

pressure calibration parameter, Q_P, and the local dynamic pressure were calculated from Eqs.3.5 and 3.8. Finally, the total pressure calibration parameter, S_P, and total pressure, and, hence static pressure were established from Eqs.3.6 and 3.8.

The velocity components u and v with respect to the x and y directions of the pressure probe, respectively, were calculated according to Eq.3.9.

$$\begin{aligned} u &= q\cos\psi \\ v &= q\sin\psi \end{aligned} \tag{3.9}$$

Results obtained by use of these polynomials were tested at several locations within the diffuser test section against the null-reading technique. The average error in measuring the flow angle was 0.81°. The rms error in velocity measurement was 1.37%.

3.5 Data acquisition

3.5.1 Analogue to digital conversion

In this study, the outputs of both the pressure transducer and the constant temperature anemometer were conditioned, linearized, analogue voltage signals. The signals were digitized through a plug-in 32 bit PCI data acquisition board (DAQ). The analogue input range was set at ±5 V. The board had an internal IDC40 connector for digital I/O, through which, the Scanivalve controller and odd-even decoder were interfaced with the computer.

3.5.2 Data acquisition software

Data acquisition software was developed in the National Instruments' LabVIEW Version 7.0. All the physical instruments were accessed from the LabVIEW platform according to the data flow logic shown in figure 3.10.

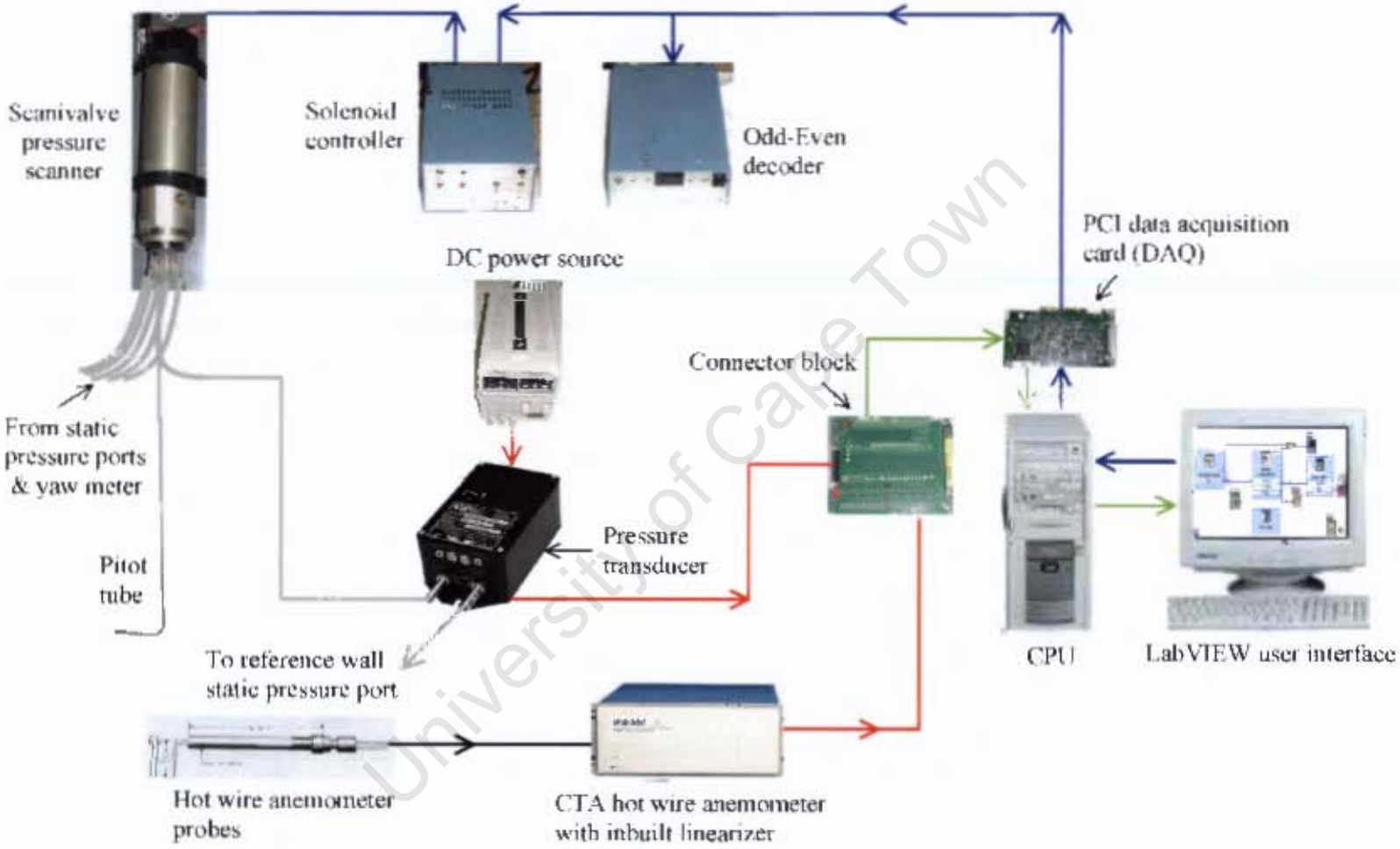

Figure 3.10: Data acquisition flow logic

For these experiments, it was established that the repeatability of the data was affected by the speed of scanning. Enough settling time had to be allowed before commencing sampling after stepping every port of the Scanivalve. This was because the response time of the static pressure in the thin vinyl tubes was fairly long. Consequently, after stepping each port, 10 seconds were allowed to pass before sampling began. Sampling was then done for 10 seconds at a frequency of 100 Hz. For each flow condition, the scanning was repeated three times. The data was processed by the LabVIEW software. before being saved in a Microsoft Excel data format to a file, ready for plotting of the curves after the experiments. A modified form of the software was used during the velocity probing experiments. Apart from the number of ports scanned, the only other slight difference was that longer integration times were used, 30 seconds for each output of the yaw meter tubes. This, and considering that very many repeatability tests were carried out, justified the main assumption of a steady flow in this research.

Chapter 4

Numerical Solutions

4.1 Finite volume approach

In chapter 2, it was shown that the transient transport by convection for any property ϕ, (for example, U_i, k, ϵ, ω, and the Reynolds stresses, $-\rho\overline{u_i u_j}$), is made up of five processes. The first two processes involve transport of this property by both turbulent and viscous diffusion, D_ϕ^t and D_ϕ^v, respectively. The third and fourth processes take into account the production due to turbulence, P_ϕ, and destruction (or dissipation), ϕ_ϕ, of property ϕ. The last process is the transport of property ϕ due to the pressure-strain relationship. Π_ϕ. The transient Reynolds averaged transport Navier-Stokes equations for property ϕ can be written in their conservative form as given in Eq.4.1 (see [109, 110]).

$$\frac{\partial(\rho\phi)}{\partial t} + \mathrm{div}(\rho\phi\overrightarrow{u}) = \mathrm{div}(\Gamma_\phi \mathrm{grad}\phi) + S_\phi \tag{4.1}$$

The first term on the right hand side of the Eq.4.1 involves both the viscous diffusion, D_ϕ^v, and the turbulent diffusion, D_ϕ^t, with Γ_φ being the diffusion coefficient. The production term, P_ϕ, the destruction term, ϕ_ϕ, and the transport by pressure term, Π_ϕ, are included in the source term, S_φ, of Eq.4.1.

Equation 4.1 can be integrated over a control volume to get;

$$\begin{aligned}\int_{cv} \frac{\partial(\rho\phi)}{\partial t} dV + \int_{cv} \text{div}(\rho\phi\overrightarrow{u}) dV &= \int_{cv} \text{div}(\Gamma_\phi \text{grad}\phi) dV + \int_{cv} S_\phi dV \\ &= \int_{cv} \text{div}(\Gamma_\phi \nabla\phi) dV + \int_{cv} S_\phi dV\end{aligned} \tag{4.2}$$

For a steady flow, and by applying Gauss' divergence theorem to the volume integral of Eq.4.2 one gets;

$$\int_A \mathbf{n}.(\rho\phi\overrightarrow{u}) dA = \int_A \mathbf{n}.(\Gamma_\phi \nabla\phi) dA + \int_A S_\phi dV \tag{4.3}$$

Finite volume integration of Eq.4.3 over the control volume yields;

$$\sum_f^{N_{\text{faces}}} \rho_f \overrightarrow{u}_f \phi_f . \overrightarrow{A}_f = \sum_f^{N_{\text{faces}}} \Gamma_\phi (\nabla\phi)_n . \overrightarrow{A}_f + S_\phi V \tag{4.4}$$

where;

N_{faces} = number of faces enclosing a cell,
ϕ_f = value of ϕ convected through face f,
$\rho_f \overrightarrow{u}_f . \overrightarrow{A}_f$ = mass flux through the face,
$\overrightarrow{A}_f$ = area of face f, $|A|$ $(= A_x\hat{i} + A_y\hat{j}$ in 2D geometries),
$(\nabla\phi)_n$ = magnitude of $\nabla\phi$ normal to face f,
V = cell volume.

The discretized values of the scalar ϕ are stored at the cell centers of each control volume of a structured non-orthogonal grid. Since the ϕ_f values are required for the convection terms in Eq.4.4, they are interpolated from the cell center values using the various differencing schemes available in the literature such as the central differencing scheme, the first order upwind scheme, the second order upwind scheme, the power law scheme, the QUICK scheme, etc. [109].

For each cell, the discretized scalar transport equation (Eq.4.4) contains the unknown scalar variable, ϕ, as well as the unknown values of this variable

in the neighboring cells, ϕ_{nb}. This equation will, in general, be non-linear with respect to these variables. A linearized form of Eq.4.4 can be written as [109, 111];

$$a_P\phi = \sum_{nb} a_{nb}\phi_{nb} + b \tag{4.5}$$

where the subscript nb refers to neighboring cells.The coefficients a_P and a_{nb} are the linearized coefficients for ϕ and ϕ_{nb} respectively. The number of neighbors for each cell depends on the grid topology, but will typically be equal to the number of faces enclosing the cell (boundary cells being the exception). Similar equations can be written for each cell in the grid. This results in a set of algebraic equations with a sparse coefficient matrix. For scalar equations, this linear system is solved using a point implicit (Gauss-Seidel) linear equation solver in conjunction with an algebraic multi-grid (AMG) method that is in-built in the Fluent CFD solver and is described in [111].

The derivative $\nabla\phi$ of the variable ϕ is used to discretize the convection and diffusion terms of the equations of motion. Using the Green-Gauss theorem, the gradient is computed as;

$$(\nabla\phi)_{c0} = \frac{1}{v}\sum_{f} \overline{\phi}_f \overrightarrow{A_f} \tag{4.6}$$

where $\overline{\phi}_f$ is the value of ϕ at the cell face centroid, v is the cell volume, and the summation is over all the faces enclosing the cell. The face value, $\overline{\phi}_f$, in Eq.4.6 is taken from the arithmetic average of the values at the centers of the neighboring cells 0 and 1 that share a common interface f, i.e.,

$$\overline{\phi}_f = \frac{\phi_{c0} + \phi_{c1}}{2} \tag{4.7}$$

4.2 Numerical treatment

Computations were performed using a finite volume code, FLUENT Release 6.2.16, on a steady two-dimensional space. Solution of the modeled equations was carried out using the segregated numerical scheme approach with the non-linear governing equations being implicitly linearized. There were no user defined source terms that were specified. The pressure-velocity coupling was achieved by use of the SIMPLEC algorithm. Discretization of the k, ω, and momentum equations was done by use of the QUICK discretization scheme.

Due to non-linearity of the RANS equations, the scalar quantities are susceptible to numerical divergence during the iteration process [109]. Some under-relaxation of the new terms was therefore required. For this reason and based on operating experience, the pressure was under-relaxed by a factor of 0.5 while the approximations for the momentum transport equations were under-relaxed by a factor of 0.7. Both the k and the ω terms were each under-relaxed by a factor of 0.8.

Convergence of the solutions was monitored by means of scaled residuals. The residual levels were set at 1×10^{-6} for the continuity equation and the specific dissipation rate. For the turbulent kinetic energy, u and v velocities, the residual levels were specified as 1×10^{-5}. These residual level settings led to net mass outflow rates given in table 4.1 for each diffuser. The upstream inlet ducts for the 28° and 42° diffusers were developed to match the diffuser geometries of Cochran and Kline [4]. Thus, the mass inflow rate for the 28° and 42° diffusers was 1.48 kg/s while for all the other diffusers, the flow rates were 0.735 kg/s. The maximum error in mass outflow was 0.16% and hence the errors were considered small enough to be neglected. Within these settings, the solution convergence was acceptable.

Table 4.1: Exit Hydraulic diameters and mass flow rates

$2\theta(^\circ)$	D_h (Exit) (mm)	Net outflow 10^{-5}(kg/s)	Error in flow rate (%)
4	229.75	0.0084	1.14e-5
7	370.27	0.034	4.6e-5
10	423.51	0.14	2e-4
15	488.29	0.14	2e-4
20	534.5	0.033	4.55e-5
28	777.62	56	0.04
30	596.41	91.7	0.12
40	636.39	120	0.16
42	884.6	140	0.09
50	664.7	50	0.07

4.3 Computational domain

Figure 4.1 shows the general configuration against which the meshing was optimized. The meshes were generated using a CAD software, Gambit Version 2.04. This CAD software was flexible enough to allow the developed meshes to be integrated directly into the Fluent solver with the boundary conditions already specified. The versatility of Gambit allowed changes of such boundary conditions, or even modification of the mesh in Fluent without having to regenerate the mesh. Since the diffuser geometries were symmetrical about the x-axis, then for each diffuser, only half of the geometry was meshed, and then reflected about the x-axis to produce the full geometry. This was exported to the solver. The inlet duct was $10W_1$ long to ensure fully developed channel flow at the inlet of the diffuser. The diffusing section had a length of $10W_1$. The flow exhausted into a plenum chamber which was of another

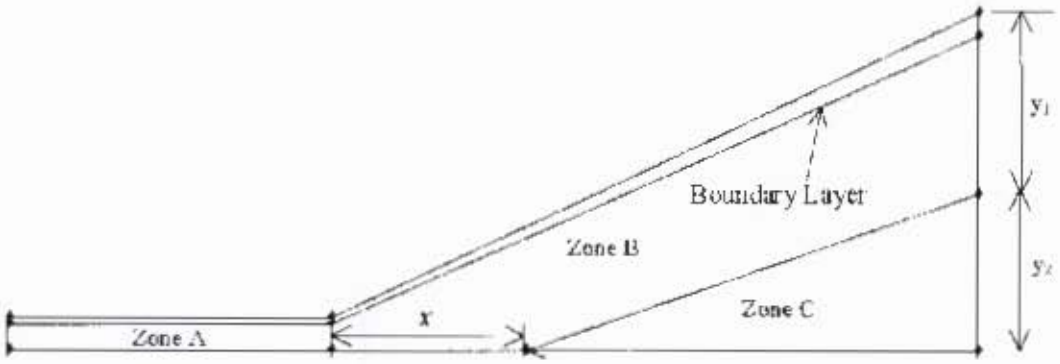

Figure 4.1: The basic mesh configuration

length $10W_1$ with a spanwise dimension of W_2. This was considered to be long enough to make the diffuser exit uninfluenced by the inherent back-flow pressure caused by the pressure outlet boundary condition. The meshing of zone A, the boundary layer thickness and grading, and lengths y_1, y_2 and x, in figure 4.1, were varied to give different mesh configurations. After many trials of meshing, it was concluded that the structured non-orthogonal meshes summarized in table 4.2 and whose notations are based on figure 4.2 gave the optimal performance against which conditions for grid independence and discretization scheme independence were tested.

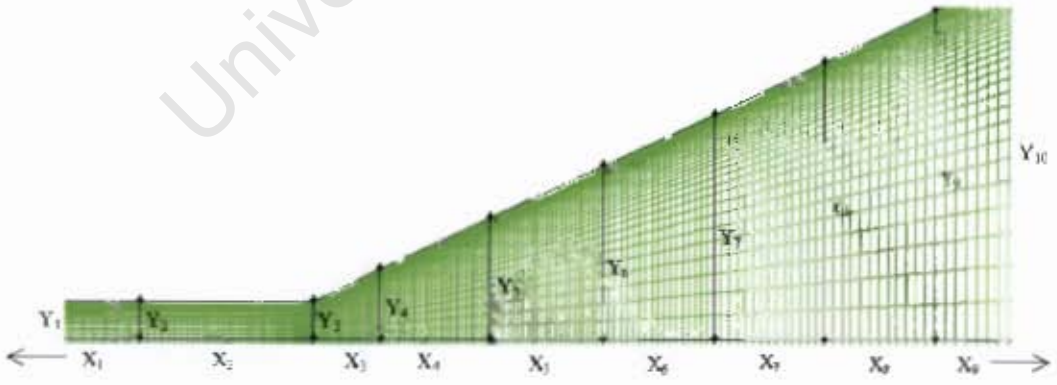

Figure 4.2: The optimized mesh configuration

The grading used while meshing edges Y_1 to Y_{10} was based on the suc-

Table 4.2: Specification for the meshes

Mesh type		X_1	X_2	X_3	X_4	X_5	X_6	X_7	X_8	X_9	Y_{10}
COARSE	L	250	250	90	150	150	150	150	150	160	Eq.4.9
	l_1	7.35	2	2	2.08	3.13	4.17	5.36	6.25	7.27	0.125
	n	34	116	70	72	48	36	28	24	22	120
FINE	L	250	250	90	150	150	150	150	150	160	Eq.4.9
	l_1	3.68	1	1	1.04	1.56	2.08	2.68	3.13	3.64	0.0625
	n	68	332	140	144	96	72	56	48	44	240
FINER	L	250	250	90	150	150	150	150	150	160	Eq.4.9
	l_1	1.89	0.5	0.5	0.52	0.78	1.04	1.34	1.56	1.82	0.03125
	n	132	664	280	288	192	144	112	96	88	480

cessive ratio approach whereby the cell lengths gradually increased as the distance from the wall was increased, generated according to the number of nodes, n, the distance of the first node, l_1, from the wall, and the total length of the edge, L. The successive ratio, r, and hence the distances between neighboring nodes were based on Eq.4.8 [112]. These edges were linked for meshing, and hence only the geometric properties for the edge Y_{10} were required. In the streamwise direction, apart from edge X_2 and X_3, whose gradings were done according to Eq.4.8, all the other edges were graded with a successive ratio of 1.

$$\sum_{i=1}^{n} r^{i-1} = \frac{L}{l_1} \qquad r = \frac{l_{i+1}}{l_i} = \text{constant} \tag{4.8}$$

$$Y_{i+1} = 50 + \left(\sum_{i=3}^{i} X_i \right) \tan\theta \qquad (i = 3, 4, ..., 9) \tag{4.9}$$

It is known that for APG flows, the wall functions that facilitate the integration of the transport equations across the viscous sub-layer, and hence

removing the need for a very fine mesh at the wall, do not give good results [59, 72, 79]. In such flows, the optimum mesh is the one whose $y^+ \approx 1$, ensuring that integration of the transport equations is performed all the way to the wall without any need for the near wall modifications of these equations. Even though the $y^+ \approx 1$ values check was performed for all the diffusers, the 50° diffuser has been chosen for the grid, model, and discretization scheme tests' presentation in section 6.3, because it provides the most severe APG flow.

Cochran and Kline [4] have shown that the introduction of short vanes at the inlet of wide angled diffusers led to an increase in pressure recovery. This aspect was investigated in this research both experimentally and numerically. The short inlet vanes of length 250 mm and thickness 0.5 mm, whose design is discussed in chapter 3, were introduced in the mesh type FINE for the 28°, 30°, 42° and 50° diffusers. A typical example of such a vaned diffuser is given in figure 4.3.

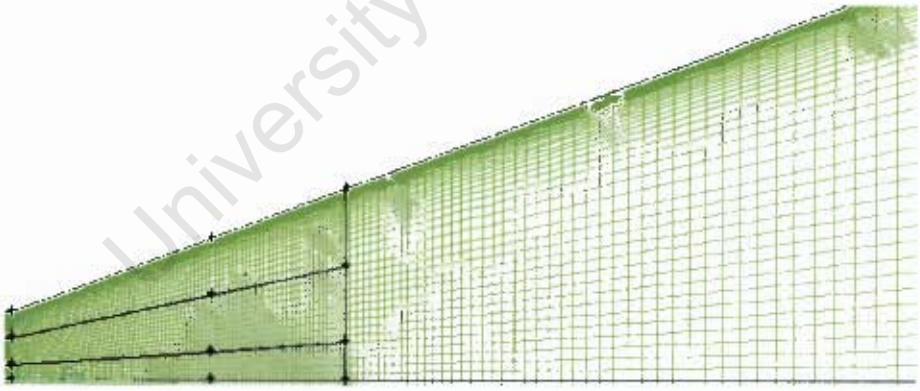

Figure 4.3: The mesh for the vaned diffuser

For all the diffuser geometries, the Reynolds numbers based on the upstream channel hydraulic diameter and the centerline velocities in the x direction were, 1.08×10^5, 1.63×10^5, 2.17×10^5 and 6.5×10^5. The air was of constant density of 1.225 kg/m^3 and constant absolute viscosity of

1.7894×10^{-5} kg/ms.

All other geometric considerations in the computational domain were developed to duplicate the experimental data set discussed in chapter 3.

4.4 Boundary conditions

The boundary condition at the inlet was specified as a constant velocity inlet with a turbulence intensity of 2% in all cases. The hydraulic diameter for 28° and 42° diffusers was 135.46 mm, while that for all the other angles was 160 mm, based on Eq.4.10.

The outlet boundary conditions were specified as constant pressure outlets with a turbulence intensity of 2% while the hydraulic diameters were as summarized in table 4.1. The pressure at the outlet was set at the gauge pressure of 0 Pa.

$$D_h = \frac{4A}{P} \tag{4.10}$$

Parameters A and P in Eq.4.10 denote the cross-sectional area and wetted perimeter of the upstream channel, respectively.

All the walls were considered as stationary walls along which the no-slip condition was applied. The wall roughness height, k_s, was specified as 0.05μm, which is the average roughness of Perpex. This ensured that the non-dimensional roughness constant, $k_s^+ = \rho k_s u^*/\mu \leq 2.25$, provided a hydrodynamically smooth wall. Within these specifications, Nikuradse's resistance data for smooth pipes could be reproduced when used with the $k-\omega$ and $k-\epsilon$ models [111] discussed in section 2.2.6. In any case, since the wall roughness was much smaller than the finest first cell height of 62.5 μm, the laminar sub-layer was then well resolved at all times.

Chapter 5

Pressure Coefficients and Uncertainties

5.1 Pressure recovery

Physical interpretation of the pressure recovery data used in the presentation of the experimental and numerical results in this research will be facilitated by reference to figure 5.1. The variations of static, dynamic, and total pressures in the two-dimensional diffuser section into which previously undisturbed air is drawn by the radial flow fan are shown in this figure. The static pressure recovered within the diffuser is $P_r = P_2 - P_1$.

In the case of a streamline such as A, the total pressure along it remains unchanged throughout the length of the diffuser and does not diminish until the streamline enters the external mixing zone at the exit of the diffuser. On the other hand, a loss of total pressure within the diffuser characterizes all streamlines such as B which traverse any part of the wall boundary layers. The velocities along streamlines A and B for an ideal fluid are given in Eq.5.1.

$$u_{2A} = \sqrt{\frac{2P_r}{\rho}} = u_{2i} \qquad u_{2B} < \sqrt{\frac{2P_r}{\rho}} \tag{5.1}$$

For the stalled asymmetric diffuser flows, the boundary layer displacement thicknesses δ^*_{2l} and δ^*_{2r} are not equal.

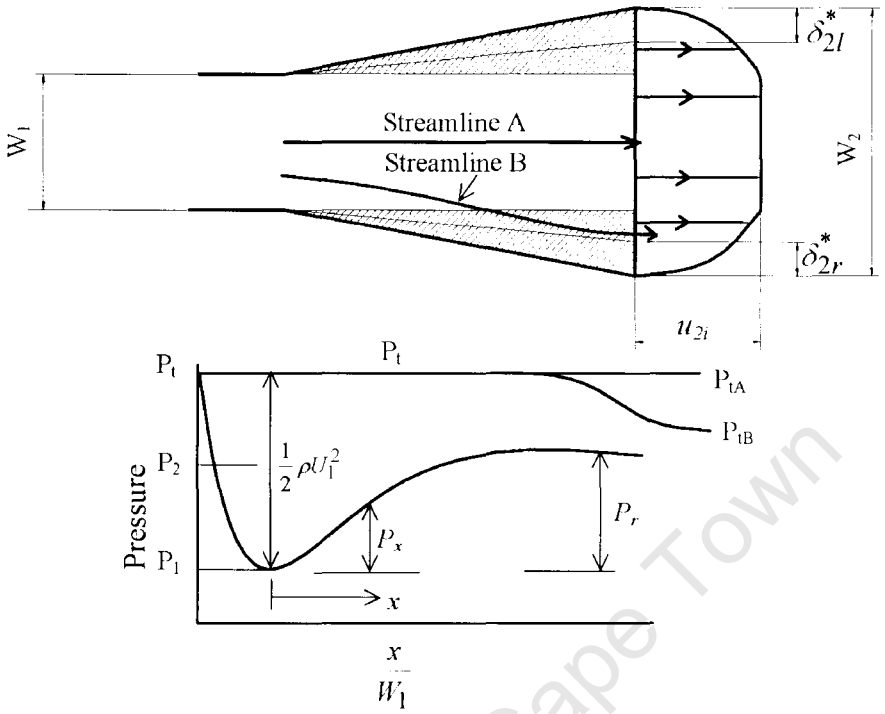

Figure 5.1: Idealized flow in diffusers

The volumetric flow rate per unit distance normal to the plane of flow is;

$$Q = u_{2i}\,(W_2 - (\delta^*_{2l} + \delta^*_{2r})) \tag{5.2}$$

If one now imagines P_2 (and P_r) to remain unchanged while the viscosity of the air and, therefore the boundary-layer thickness diminish indefinitely, conservation of Q necessitates a reduction of the exit width by the amount of the reduction of total boundary-layer displacement thickness at the exit.

Thus, as the viscosity approaches zero,the exit width would approach the limiting value $W_2 - (\delta^*_{2l} + \delta^*_{2r})$. Furthermore, reduction of the diffuser width throughout its length by amounts equal to the local displacement thicknesses would leave both the axial distribution of static pressure and the volumetric flow rate unchanged by the elimination of viscosity. Thus the volumetric flow rate and axial distribution of static pressure in a real diffuser are those

which would characterize frictionless flow through a diffuser whose transverse dimensions were smaller than those of the real one by the local thickness of the wall boundary layers. Conservation of Q in this idealized flow must then be followed by a reduction of static pressures at all points upstream of the diffuser exit.

However, in a real diffuser, the manner in which this reduction to the initial pressure P_1 occurs can only be experimentally determined. Besides that, the absolute values of the P_1 and P_2 will vary for different diffusers depending upon their geometries and inlet velocities U_1. If the trends were to be generally described then these concepts suggest expression of the experimentally determined static-pressure rise within a diffuser in the form of a non-dimensional coefficient. The most commonly used non-dimensional coefficient is known as the pressure-recovery coefficient and is defined as;

$$C_{pr} = \frac{P_2 - P_1}{\frac{1}{2}\rho U_1^2} \tag{5.3}$$

Further, to represent the static pressure distribution in the diffuser flow-field and more specifically at the walls, a static pressure coefficient is defined for any location downstream of the diffuser entry as;

$$C_p = \frac{P_x - P_1}{\frac{1}{2}\rho U_1^2} \tag{5.4}$$

where P_x is the pressure measured at any location either at the wall or in the flow-field. With these two coefficients, it is now possible to compare the pressure rise and static pressure profiles for different diffusers regardless of their geometry.

5.2 Statement of uncertainties

Due to the large number of data points in this research, the statement of uncertainties is based on the overall mean of standard deviations of repeated measurements at selected data points. To avoid going into the details of error analysis and yet retain the clarity in the statement of these discrepancies, only a brief presentation of the equations, as they are used in this research, is given.

5.2.1 Instrumentation random errors

These are the errors that resulted from the use of the pressure transducer in measuring both the pressure coefficients, C_p, and normalized velocity profiles, u/U_1. The pressure coefficients and normalized velocity profiles were measured according to Eq.5.5.

$$\begin{aligned} C_p &= \frac{P_x - P_1}{P_{D1}} \\ \frac{u}{U_1} &= \sqrt{\frac{P_T - P_x}{P_{D1}}} \end{aligned} \tag{5.5}$$

where the numerators and denominators of terms in Eq.5.5 are differential pressures measured by the transducer, denoted as P_R and P_D, respectively. The uncertainty of the transducer was stated as 1% including non-linearity errors. Based on the error analysis given in [113–115], and if C_p and u/U_1 are denoted by ϕ, then the resulting error, ε_ϕ, becomes;

$$\varepsilon_\phi = \left[\left(\frac{\partial \phi}{\partial P_R} \varepsilon_R \right)^2 + \left(\frac{\partial \phi}{\partial P_D} \varepsilon_D \right)^2 \right]^{1/2} \tag{5.6}$$

where $\varepsilon_R = \varepsilon_D$ is the uncertainty of the transducer differential pressure measurements, P_R and P_D. The uncertainties for C_p and u/U_1 are respectively;

$$w_{c_p} = \frac{\varepsilon_{c_p}}{C_p} \quad \text{and} \quad w_{upr} = \frac{\varepsilon_{upr}}{u/U_1} \tag{5.7}$$

where ε_{c_p} and ε_{upr} are the errors in measuring C_p and u/U_1 respectively. It is then a straightforward matter to show that

$$w_{c_p} = \left[w_R^2 + w_D^2\right]^{1/2} \quad \text{and} \quad w_{upr} = \frac{1}{4}\left[w_R^2 + w_D^2\right]^{1/2} \tag{5.8}$$

Thus, the uncertainties due to the instrumentation in measuring all the pressure coefficients, and all the velocity profiles are 1.4% and 0.35% respectively.

5.2.2 Experimental random errors

The experimental random errors at each point, and the overall experimental uncertainties, w_ϕ were determined using Eq.5.9. Discrepancies in the numerical results was based on the comparison of these results with experimental data either from this research or in some cases, those from published literature in a manner proposed in [116] and also calculated according to Eq.5.9.

$$w_{\phi_j} = \frac{\sqrt{\frac{1}{n}\sum_{j=1}^{n}\left(\phi_j - \overline{\phi}_j\right)^2}}{\overline{\phi}_j} \text{x} 100\% \quad \text{and} \quad w_\phi = \frac{1}{N}\sum_{i=1}^{N} w_{\varphi_i} \tag{5.9}$$

where $\overline{\phi}_j$ and n are the mean values of ϕ and the number of repeated readings measured at each data point respectively, and N is the total number of data points for a particular series of measurements.

Chapter 6

Results and Discussion

6.1 Tunnel qualification

6.1.1 Inlet channel flow

While reviewing the influence of inlet flow conditions on the diffuser performance in chapter 1, it was stated that the boundary layer thickness and uniformity as characterized by the blockage factor was important. In this respect, the inlet axial velocity profiles were measured, first without the diffuser and then repeated with the diffuser connected to the inlet duct. As can be seen from figure 6.1, the introduction of the diffuser introduced serious asymmetry of the inlet flow. The non-uniformity of the flow, λ, was evaluated as the overall discrepancy of axial velocities u_i, measured at corresponding points to the right and left of the x-axis. The overall discrepancy for any parameter was established by using Eq.5.9. A summary of the non-uniformities for all the diffusers with flow at different Reynolds numbers is given in table 6.1. The non-uniformity of the flow caused the corresponding static pressures on the opposite side walls at the inlet to be different. This situation presented a problem in the interpretation of reference inlet conditions both for the velocity and static pressure data, since each flow condition produced different profiles. Consequently, it was found necessary to refer-

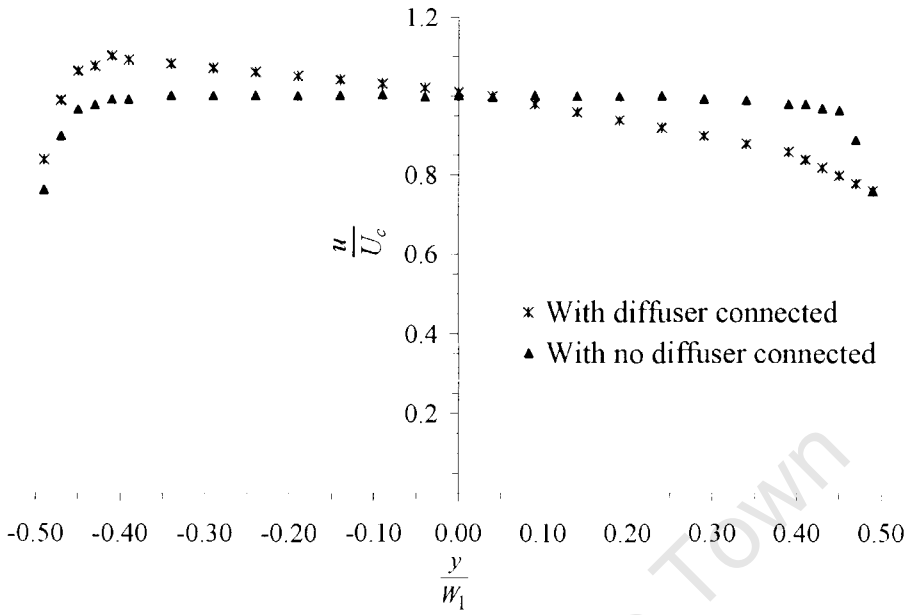

Figure 6.1: Inlet axial velocity profiles in the 50° diffuser

Table 6.1: Non-uniformity, λ (%), of inlet flow with diffuser

2θ	Re=1.08 × 10^5	Re=1.63 × 10^5	Re=2.18 × 10^5
30°	4.17	4.41	4.92
40°	4.21	4.42	4.77
50°	4.23	4.55	5.03

ence the inlet flow conditions to a location where the flow was reasonably uniform. Such a point was found to be at an arbitrarily chosen upstream location of $x/W_1 = -2.35$. At this inlet reference location, the axial velocity profiles were again measured, with and without the diffuser. Table 6.2 gives the non-uniformity of the axial velocity profiles measured in both the y and z directions at the reference diffuser location. All the measurements in the inlet duct were carried out using a single hot-wire anemometer.

From the velocity profiles at the reference location, boundary layer block-

Table 6.2: Non-uniformity, λ (%), of flow at $x/W_1 = -2.35$

Direction	2θ	Without diffuser			With diffuser		
		Re$\times 10^5$			Re$\times 10^5$		
		1.08	1.63	2.18	1.08	1.63	2.18
y	30°	0.12	0.12	0.13	0.19	0.20	0.20
	40°	0.13	0.13	0.13	0.20	0.22	0.23
	50°	0.15	0.15	0.14	0.25	0.25	0.27
z	30°	0.12	0.12	0.12	0.18	0.18	0.18
	40°	0.12	0.13	0.12	0.20	0.0.22	0.23
	50°	0.14	0.14	0.14	0.22	0.23	0.23

age factors B, were evaluated according to Eq.6.1.

$$B = \frac{2\delta^*}{W_1} = \frac{2}{W_1}\int_0^{\delta}(1 - \frac{u}{U})dy \tag{6.1}$$

The blockage factors were approximately 0.014 and hence the pressure recovery data can be compared with the data of Reneau et al. [3], which is available for $B = 0.015$. Table 6.3 summarizes both the blockage factors and the corresponding centerline turbulence intensities obtained for the three diffusers at the three different Reynolds numbers. A typical turbulence intensity profile, evaluated according to Eq.3.3, and measured alongside the velocity profiles is shown in figure 6.2. Of interest to this study, and for characterization of the inlet flow during the computational modeling, was the turbulence intensity at the centerline of the inlet duct.

It still remains unclear why stalling in the two-dimensional fully stalled regime in diffusers occur on a particular wall. As was described in chapter 3, great care was taken to manufacture highly symmetrical diffusers. Tests to rule out the possibility of a bias towards the flow attaching to a particular wall whenever the fan was switched on were carried out. In this regard, for

Table 6.3: Diffuser inlet blockage factors and turbulence intensities

	Blockage factors			Turbulence intensities (%)		
$Re/2\theta$	$1.08x10^5$	1.63×10^5	2.18×10^5	1.08×10^5	1.63×10^5	2.18×10^5
30°	0.0141	0.0142	0.0140	2.33	2.41	2.36
40°	0.0141	0.0141	0.0141	2.22	2.20	2.31
50°	0.0140	0.0139	0.139	2.41	2.32	2.27

all diffusers and before any measurements were taken, a start-stop check was done whereby the fan was started, the wall to which the flow was attached noted, the fan switched off and started again and the process repeated. These tests were done at an inlet duct velocity of 15 m/s. An intermittency parameter γ_s, was then defined as a ratio of the number of times the flow remained attached to a given wall to the total number of start-stop cycles. Figure 6.3 shows the variation of γ_s after 50 cycles of the start-stop experiments.

The same behavior was portrayed in the computational models whereby, computations were performed until solution convergence was achieved and the stall wall noted. Without altering anything in the CFD code, the flow was initialized and computations repeated. This procedure was repeated 10 times. Figure 6.4 shows typical contour plots of the streamlines for a 50° diffuser with the flow attached to the right and left walls, respectively in two such cycles. Even though the intermittency of stall between the two walls showed greater discrepancy (see figure 6.3) in the computational models than in the physical models, the fact that the flow was not biased to one wall ruled out the possibility of symmetrical imperfections as the reason for which the diffuser stalled on a particular wall. Furthermore, while it might be difficult to manufacture a perfectly symmetrical diffuser, the geometries produced in the CAD software that generated the meshes produced perfectly symmetrical

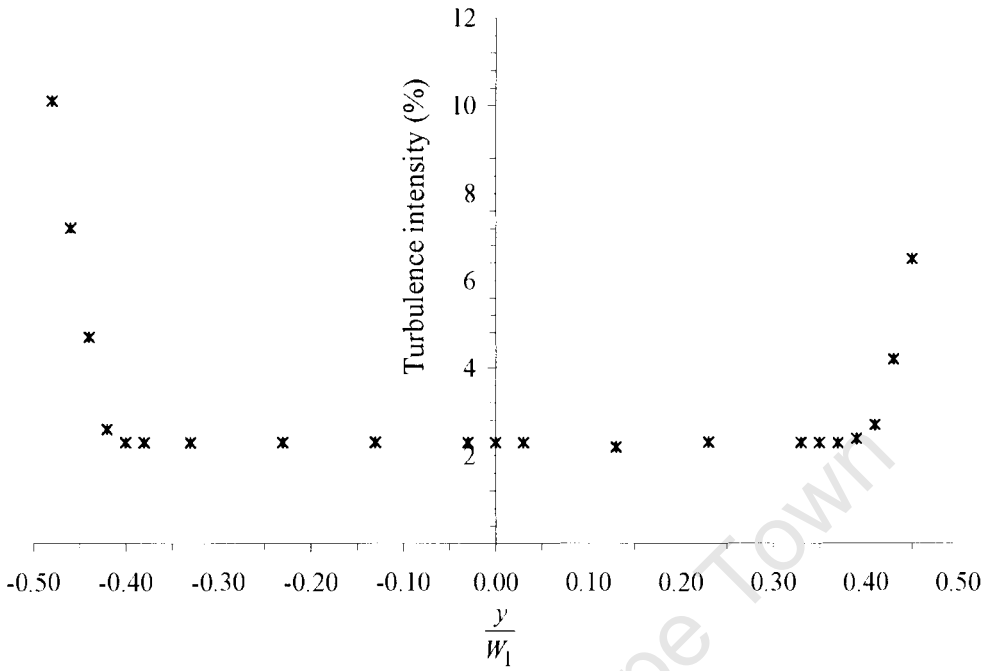

Figure 6.2: Turbulence intensity at $x/W_1 = -2.35$ for the 30° diffuser

diffusers. This reality implies that there is more to the stall bias than just the small manufacturing imperfections that might be present in the physical model.

In the physical models, it was possible to force the flow to attach to the other wall by partially blocking the flow at the inlet with a piece of Perspex, and directing it to the desired wall. Once 'switched' to the other side, the flow remained attached to that wall. However, in the computational model, this was not possible and computations were performed to solution convergence and 'switched' to the desired wall during post processing of the results. Thus, in instances when the stall wall in the computational model was different from that of the physical model, the results were reflected about the x-axis to allow comparison.

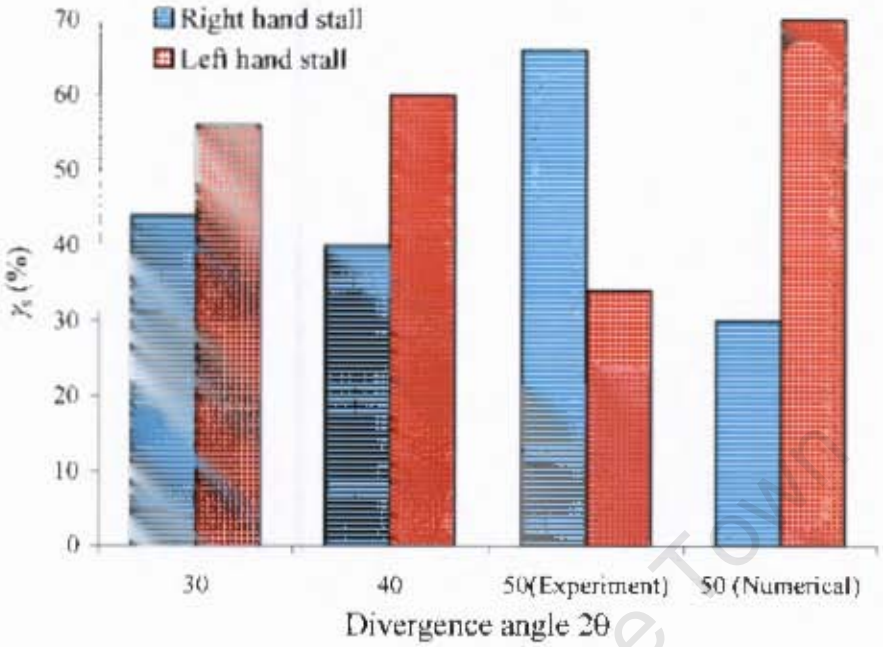

Figure 6.3: Intermittency of stalling between diffuser diverging walls

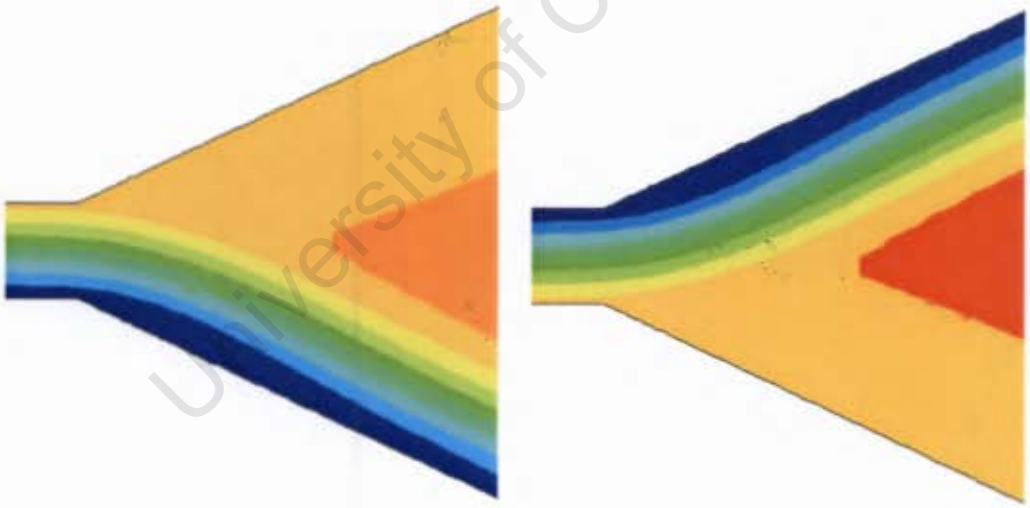

Figure 6.4: Streamline contours for the 50° diffuser

6.1.2 Reproducibility and replication

Flows in wide angled diffusers are inherently unsteady. In order to reduce the effect of the unsteadiness in the experimental results, the pressure trans-

ducer differential voltages, were averaged over long durations. The optimal averaging duration was achieved by setting it at a given value and then measuring the velocities and static pressures at a few selected data points while holding the inlet velocity constant. The averaging period was then varied and the measurements at the same data points repeated. Thus, the optimal averaging duration corresponded to the period beyond which the velocity and static pressure readings ceased changing with change in averaging period. This optimal averaging time was kept constant for the rest of the measurements and it was only then that the repeatability tests to determine the overall experimental uncertainties were performed. Due to the large number of data points obtained especially when measuring the velocity profiles, it was found adequate to take readings at each point three times and then average their discrepancies for all the data points in accordance with the techniques discussed earlier. In any case, the statement of overall uncertainties is all that is required. Figures 6.5 and 6.6 show typical reproducibility results obtained for the wall static pressure recovery and velocity field, respectively for a 30° diffuser. The reproducibility tests were however performed for all the angles and the results of the tests are summarized in table 6.4. Even though the reproducibility seems to worsen as both Reynolds number and divergence angles increased, the maximum discrepancy at 1.88% indicate fairly reproducible experiments of these physically complex flows.

As was shown in the previous section, the wall to which the flow attached was quite random. However, since the data acquisition system was placed on the left side of the diffuser, the flow was always manually 'switched' to the left wall in instances when it attached to the right wall. With this in mind, it was important to confirm that both the pressure and velocity fields were independent of the wall to which flow was attached. To verify this

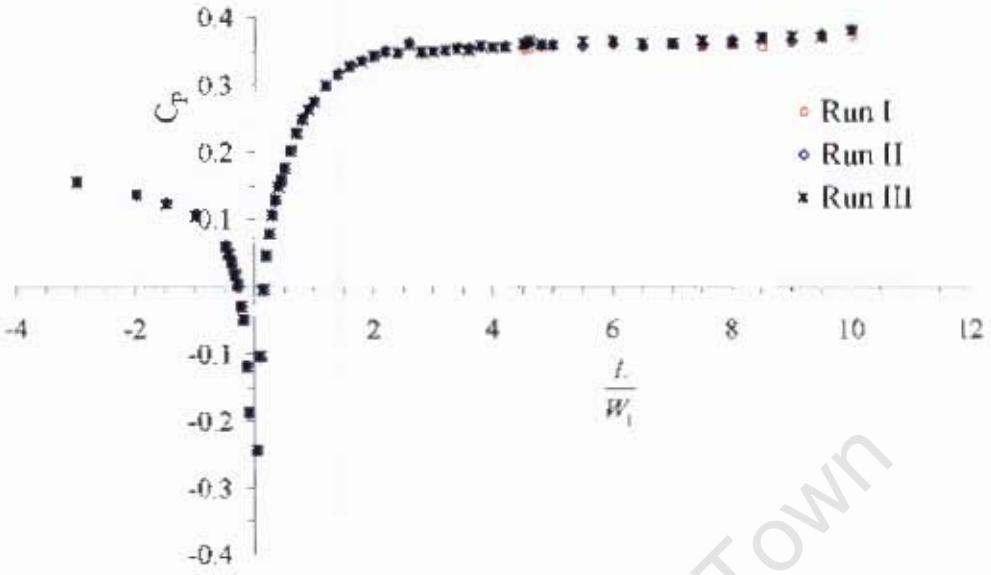

Figure 6.5: Reproducibility of C_p for the 30° diffuser

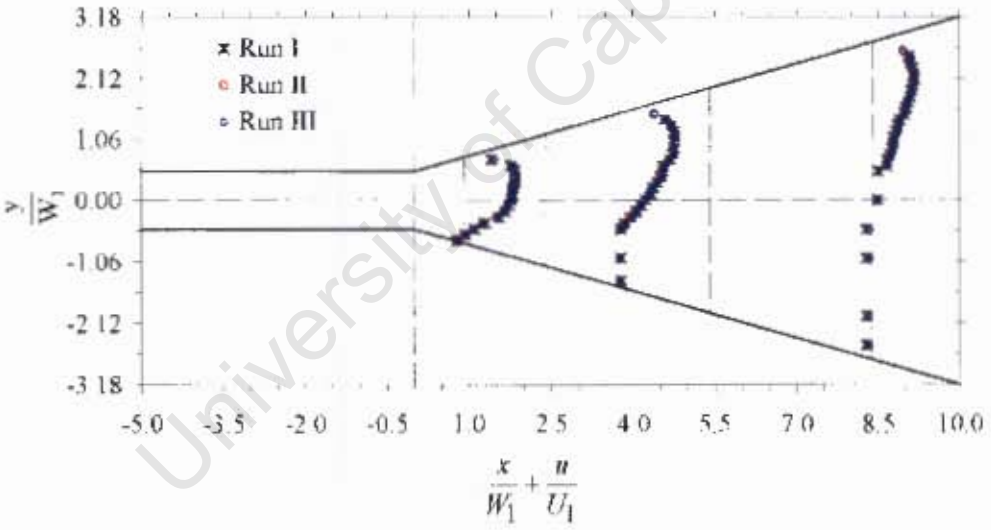

Figure 6.6: Reproducibility of velocity profiles for the 30° diffuser

requirement, the flow field was measured with the flow firstly attached to the left wall and secondly with the flow attached to the right wall, as can be seen from figure 6.7. For case of comparison, results of figure 6.7, when the flow was attached to the right wall, were reflected about the x-axis shown in

figure 6.8, leading to the choice of the term 'mirror replication' to describe the tests.

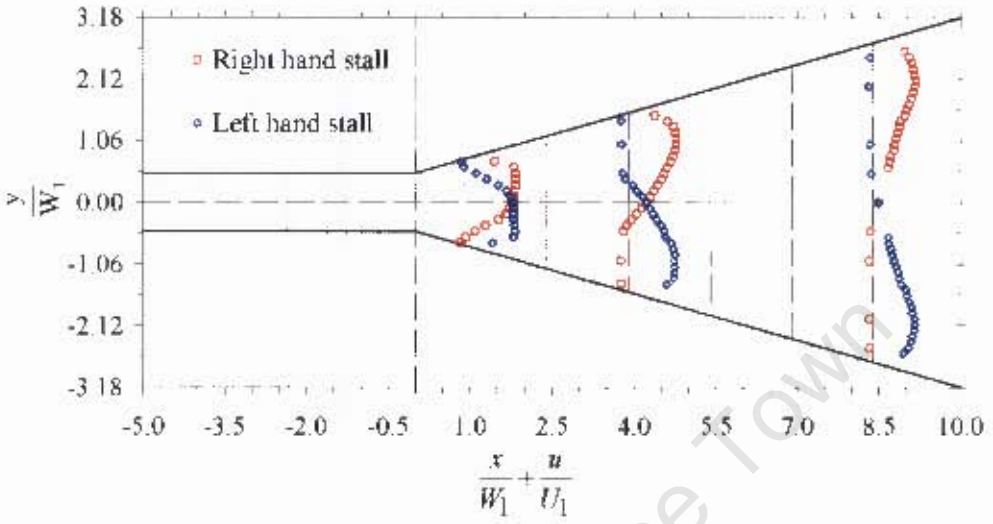

Figure 6.7: Replication of velocity profiles for the 30° diffuser

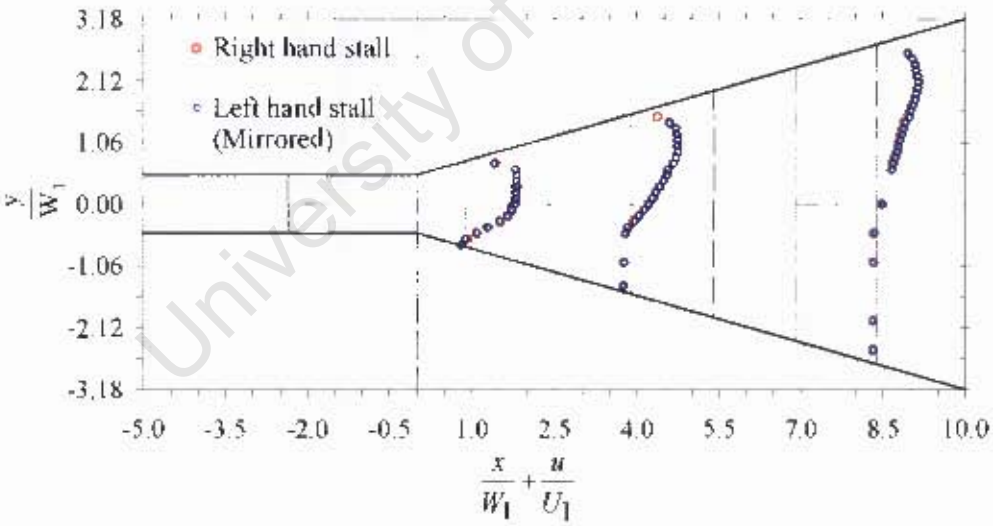

Figure 6.8: Mirror replication of velocity profiles for the 30° diffuser

Lastly, static pressures were measured on the wall to which the flow was attached (unstalled wall). Pressure recovery data for corresponding static pressure holes on the two walls is shown in figure 6.9. These replication tests

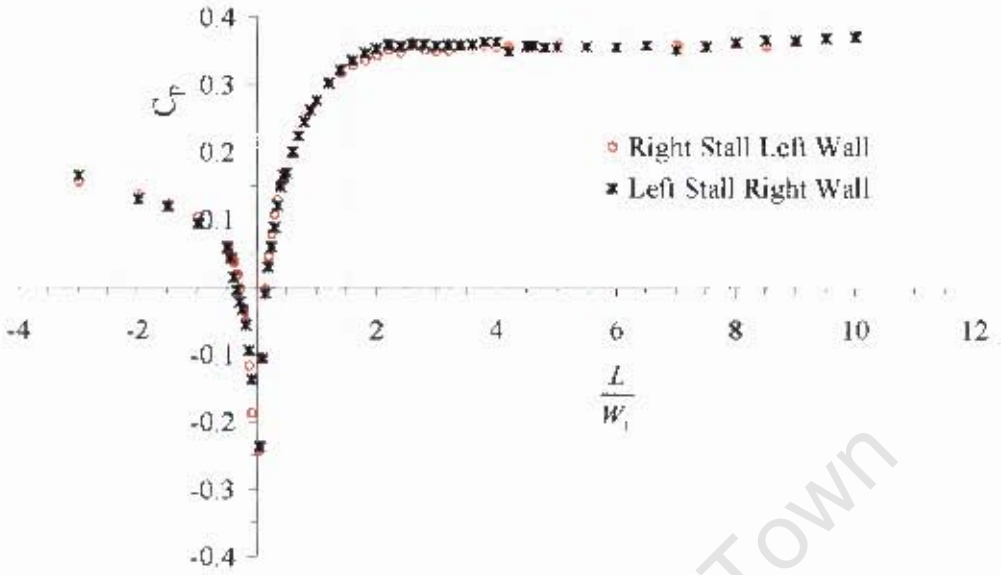

Figure 6.9: Replication of C_p for the 30° diffuser

were performed for all the angles at the different Reynolds numbers and a summary of these results are also included in table 6.4.

Table 6.4: Reproducibility and replication of diffuser flows

Flow field	2θ	Reproducibility discrepancy,% Re×10^5 1.08	1.63	2.18	Replication discrepancy,% Re×10^5 1.08	1.63	2.18
Pressure recovery	30°	1.42	1.57	1.63	1.77	1.85	1.97
	40°	1.53	1.61	1.70	1.91	1.97	2.01
	50°	1.66	1.72	1.88	1.93	1.99	2.13
Velocity profiles	30°	0.32	0.36	0.37	0.52	0.55	0.57
	40°	0.34	0.33	0.39	0.53	0.56	0.58
	50°	0.36	0.37	0.34	0.56	0.58	0.59

The static pressure field showed more sensitivity to replication than the velocity profiles. The replication discrepancies for the static pressure field

worsened as the flow velocity and divergence angle were increased. However, since the replication discrepancies are of the same order of magnitude as the reproducibility, they can be viewed to be a result of the flow unsteadiness and the small imperfections in the diffuser symmetry. The replication discrepancy of the velocity profiles was below 0.6% in all cases.

6.1.3 Reynolds number dependence

Although it is reported in the literature that variation of Reynolds number does not influence the pressure recovery data, the indications obtained while performing the reproducibility and replication tests, was that Reynolds number indeed has a significant influence on the flow field. It was therefore decided to perform tests to evaluate the influence of Reynolds number on both the static pressure and velocity fields. The inlet velocity was set at 10 m/s, 15 m/s and 20 m/s corresponding to Reynolds numbers 1.08×10^5, 1.63×10^5, 2.18×10^5, respectively. Preliminary tests showed that higher velocities produced undesirable vibration of the diffusers. Figures 6.10 and 6.11 show the influence of the Reynolds number on the wall static pressure recovery and velocity profiles respectively.

It can be observed from figure 6.10, that near the diffuser inlet the influence of Reynolds number on static pressure recovery is significant. This observation is roughly represented in a plot of the standard deviation of C_p values about the mean along the walls. As expected, the largest deviation occurs near the inlet as can be seen in figure 6.12.

This sensitivity of C_p values to Reynolds number changes can be attributed to the three dimensionality nature of the flow expected in this region and to the fact that it is in this region that the highest adverse pressure gradients are experienced, rendering the flow here very unstable. Attempts

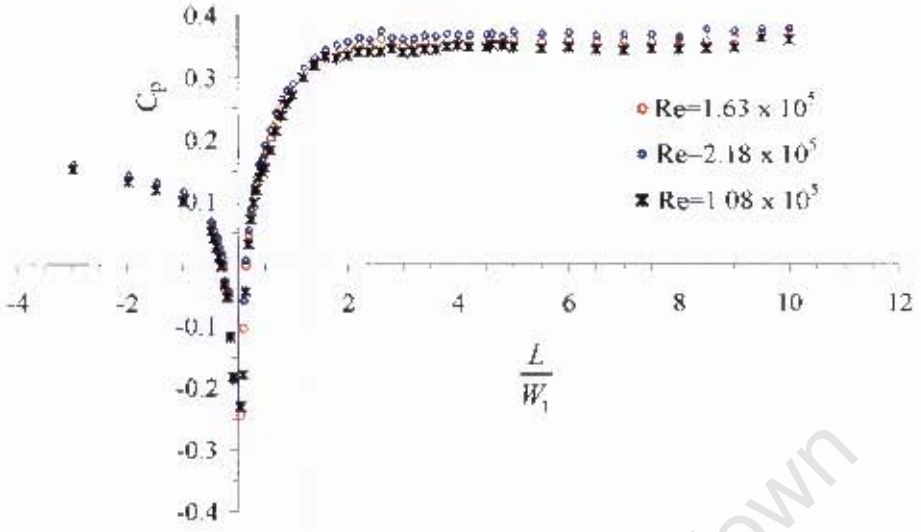

Figure 6.10: Influence of Re on C_p for the 30° diffuser

to use the yaw meter to measure the velocity profiles in this region resulted in data whose reproducibility was above 15%. However, velocity profiles measured at the first strip (located 90 mm downstream of the diffuser inlet), indicated very little influence (of the order of 1%) on the profiles due to Reynolds numbers, as can be seen from figure 6.11.

To get an indication of the influence of Reynolds number and yet include results from this very unstable region, some out-of-range discrepancy results were statistically rejected using Chauvenet's data rejection criteria '115'. With this treatment of data, the results show that by changing the velocity from 10 m/s to 20 m/s, the static pressure recovery increased by 8.31%, 10.15%, and 9.35% for 30°, 40° and 50° diffusers, respectively. A similar data treatment approach adopted for the velocity profiles showed that the increase of the normalized velocities, for a similar increase in Reynolds number, was 1.37%, 1.57%, and 1.60% for 30°, 40° and 50° diffusers, respectively. Evidently, the static pressure was influenced by the Reynolds number at values that are outside the overall experimental uncertainties of about 2% in this

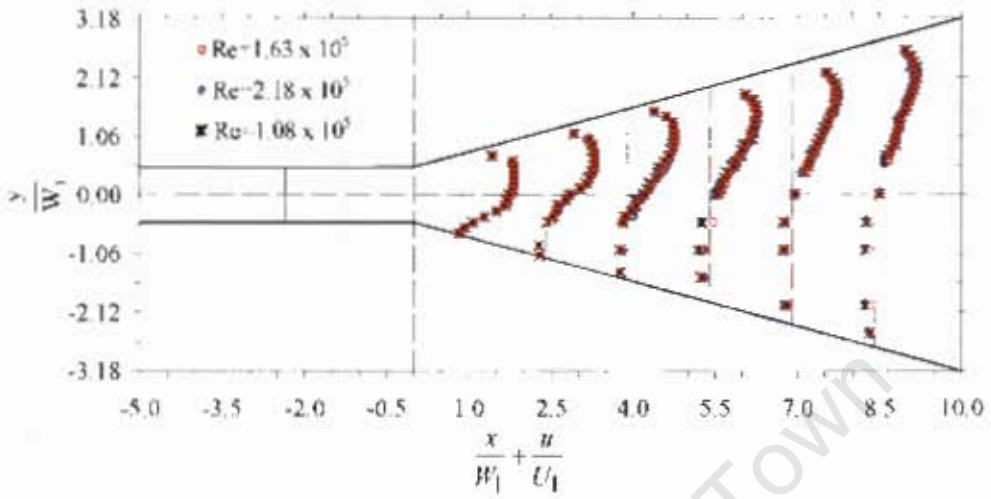

Figure 6.11: Influence of Re on velocity profiles for the 30° diffuser

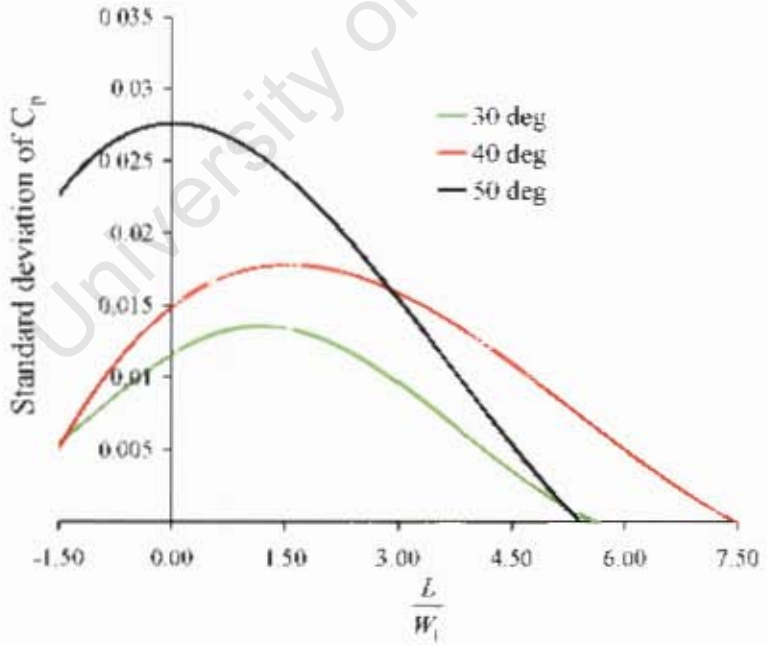

Figure 6.12: Standard deviation of C_p data due to change in Re

research.

It might be of interest in future to carry out a study that can relate, Reynolds number to diffuser geometry. Results from the limited number of flow cases in this study can not be considered adequate to provide a reasonable correlation. Bearing this in mind and in order to focus on the primary objectives of this research, it was decided that from this point onwards, the Reynolds number be held constant at 1.63×10^5 corresponding to an inlet duct velocity of 15 m/s.

6.1.4 Two-dimensionality

The primary assumption made in this study is that the flow is two dimensional. In fact, it is only due to this assumption that the three-tube yaw meter was used to measure the velocity vectors. All diffusers studied in this research had the roof and the floor walls running parallel to each other. It was rational to assume that the boundary layer growth rates from the floor and roof walls were the same and merged at the mid-plane. Therefore, measuring the flow in the mid-plane was adequately representative of a two-dimensional flow.

Traditionally, proof of two-dimensionality of a flow is carried out by measuring axial velocity profiles at two different planes, one below the mid-plane, and another above the mid-plane. Thus, for a given location within the diffuser, axial velocity profiles were measured in three planes, namely; upper, mid and lower planes. The upper and lower planes were both at a 100 mm distance from the roof and floor of the diffuser respectively. For all diffusers in this study, the two-dimensionality of the flow was verified using this procedure, with the velocity profiles being measured at three locations downstream of the diffuser inlet located at $x/W_1 = 0.9$, 3.9 and 8.4. The tests were car-

ried out at 15 m/s. Typical results of such measurements are shown in figure 6.13.

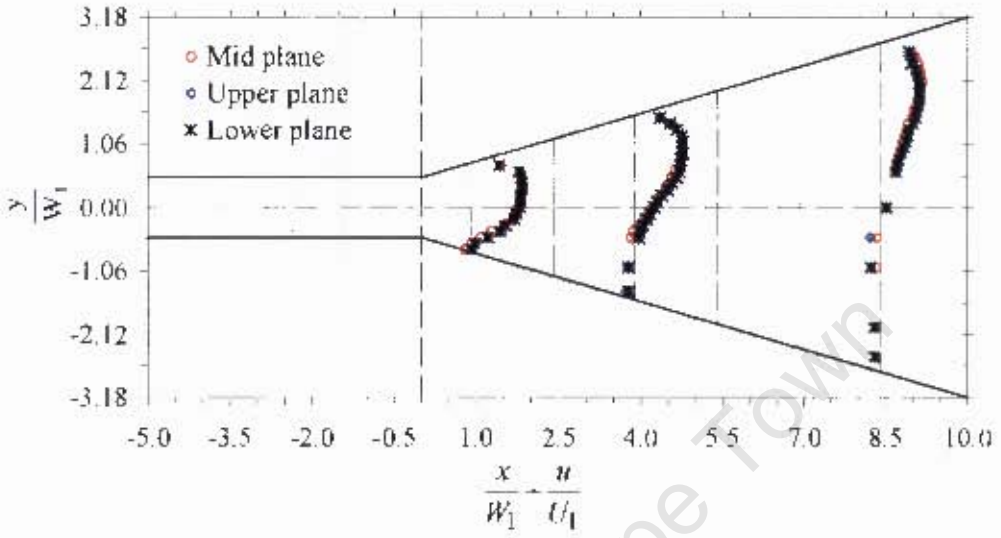

Figure 6.13: Two-dimensionality test for a 30° diffuser

The velocity profiles in the upper and lower planes, for symmetrical boundary layer growth rates between roof and floor walls, must be the same. With the mid-plane held as the datum, the overall deviations from this plane for the lower and the upper planes are shown in figure 6.14. The largest difference in these deviations between the upper and lower planes in figure 6.14 was 0.3% meaning that the two-dimensionality was well within the uncertainties of the experimental data in this study. However, the lower plane consistently gave higher discrepancies, in line with what Kline [8] observed about the stall starting at a localized position on the lower corners of the diffuser before spreading to the rest of the diffuser.

Flow visualization using woolen tufts was performed in order to observe the steadiness and two-dimensionality of the flow. The woolen tufts were attached to the side walls of the diffuser at several locations. Apart from the tufts that were next to the roof and floor, and which displayed slight

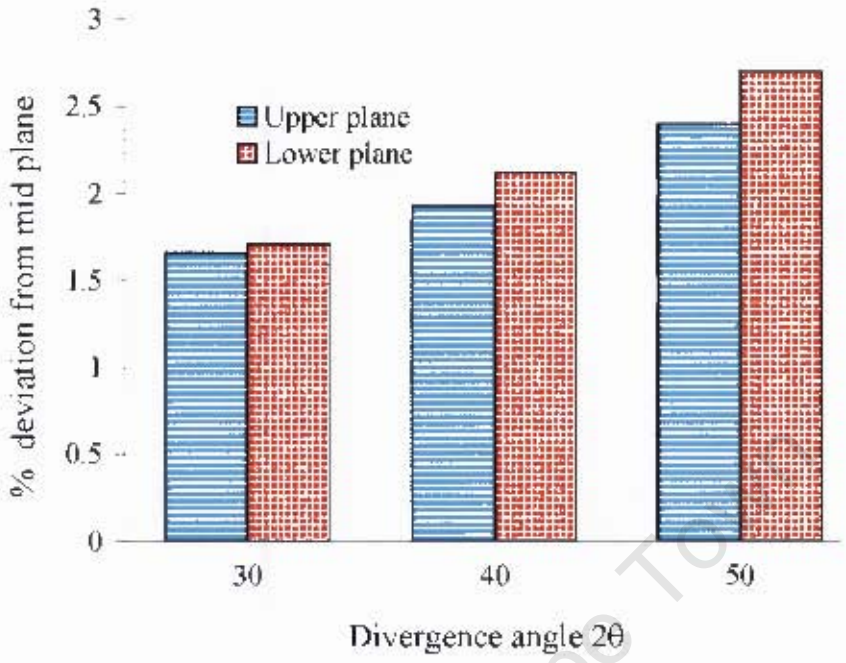

Figure 6.14: Discrepancies in the velocity profiles between planes

fluctuations of movement, all the other tufts faced the downstream direction steadily and ran almost parallel to each other as can be seen from figure 6.15.

Further flow visualization was carried out using thin tailor's thread. Long pieces of the thread were passed through corresponding static pressure holes across the width of the diffuser at several locations in the flow-field. On each of these threads, short pieces of thread about 20 mm long were tied at several points. Lastly, pieces of the tailor's thread were passed through each wall static pressure hole. Following, this treatment, the flow visualization results shown in figure 6.36, and to be discussed later, were obtained. On the unstalled wall near the diffuser inlet of the 50° diffuser, a separation bubble consistent with the notation of figure 6.36 was observed. This bubble was not present in the flow visualization results of the 30° and 40° diffusers.

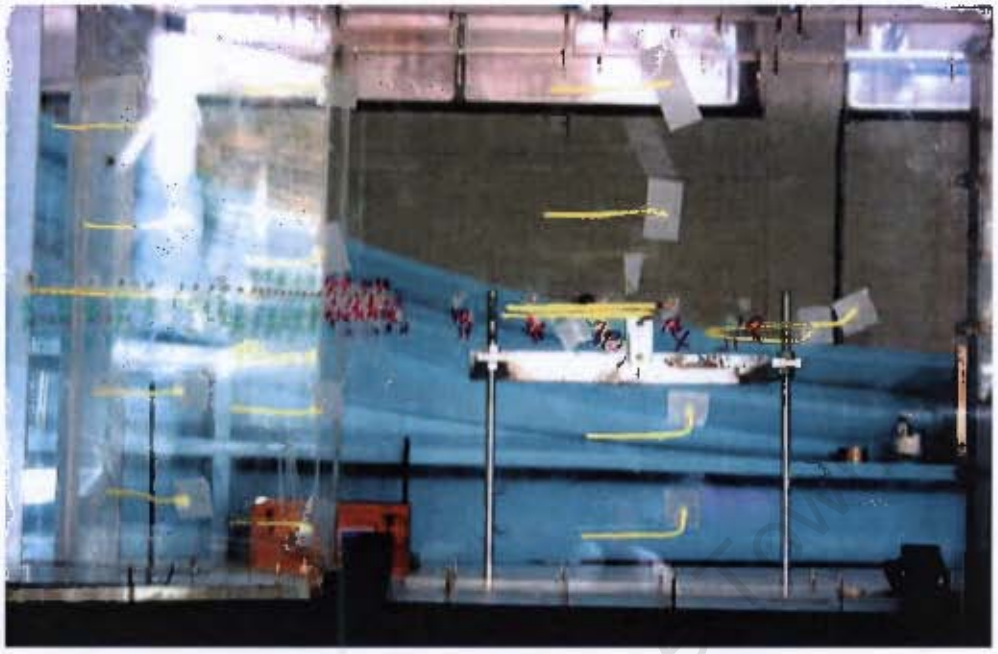

Figure 6.15: Tuft flow visualization on the side walls

6.2 Data bank contribution

In the interest of clarity while discussing the experimental results, only representative cases of extensive experimental data have been presented. However, the same rigorous checks and experimental procedures, as discussed in section 6.1, were performed for all flow cases. These results are presented in appendix A as a data bank contribution. The experimental and numerical results from identical flow cases are presented on the same graphs for ease of comparison. The results presented in the data bank include, the axial velocity profiles, u/U_1, lateral velocity profiles, v/U_1, and the wall static pressure recovery and static pressure fields, C_p.

It is known from previous research [4 6] that the introduction of inlet vanes to a diffuser greatly improve diffuser pressure recovery. This aspect of diffuser flows was also investigated in this research. However, introduction of the vanes led to unsteadiness of the flow as was observed through flow

visualization studies. The flow switched randomly from one wall to the other even though no external disturbance had been applied. For this reason, no measurement of the velocity field was attempted. The overall pressure rise $P_2 - P_1$, and hence C_{pr}, was measured by averaging the differential pressure between the inlet and outlet of the diffuser over a long period of time, typically 90 seconds. These results are presented together with the simulated results in section 6.6.

6.3 Computational models: Convergence

For a turbulence model to give results that can be verified by physical testing, the model must satisfy certain solution convergence criteria. Such criteria include, grid and discretization scheme convergence. Two-equation eddy viscosity models were chosen in this research because they are known to give reasonable solutions in APG flows. Preliminary computations with the more 'accurate' RSM and LES models failed to predict stalling of the flow while using the same grid as that of the eddy viscosity models. This was a clear indication that a finer grid was required with the possibility of performing the computations in an unsteady three dimensional space, if RSM and LES models were to provide reasonable predictions. Considering that the optimal grid used (fine mesh) had 229,440 cells in a two-dimensional space, performing the computations in the three dimensional space required the introduction of more planes over the 0.4 m depth of the diffusers. In terms of computing resources and the convergence periods, this was prohibitively expensive.

The Menter SST $k - \omega$ model was used in the convergence tests. In all cases, the pressure-velocity coupling was performed using the SIMPLEC scheme due to its increased pressure-correction under-relaxation which greatly improves convergence in APG flows [111].

6.3.1 Grid convergence test

A large number of grid types were tested as discussed in section 4.3. The momentum, k and ω equations were discretized using the QUICK scheme. The grid was refined several times by reducing the mesh sizes to the optimal size until the flow properties stopped varying with further grid refinement. The convergence tests were performed on only the 50° diffuser since it was thought to present the most stringent flow conditions in terms of the pressure gradients and severity of the velocity profile distortions. Once grid convergence was achieved, the same grid properties were used for all the narrower diffusers. Three mesh types namely; 'coarse mesh', 'fine mesh' and 'finer mesh', and whose properties are given in table 4.2, were used to test for the grid independence of the numerical solutions. The overall discrepancies in the velocity profiles of the 'coarse' and 'finer' meshes from the 'fine' mesh were 0.46% and 0.63%, respectively, for the velocity profiles that are shown in figure 6.16. Corresponding discrepancies for the static pressures, in figure

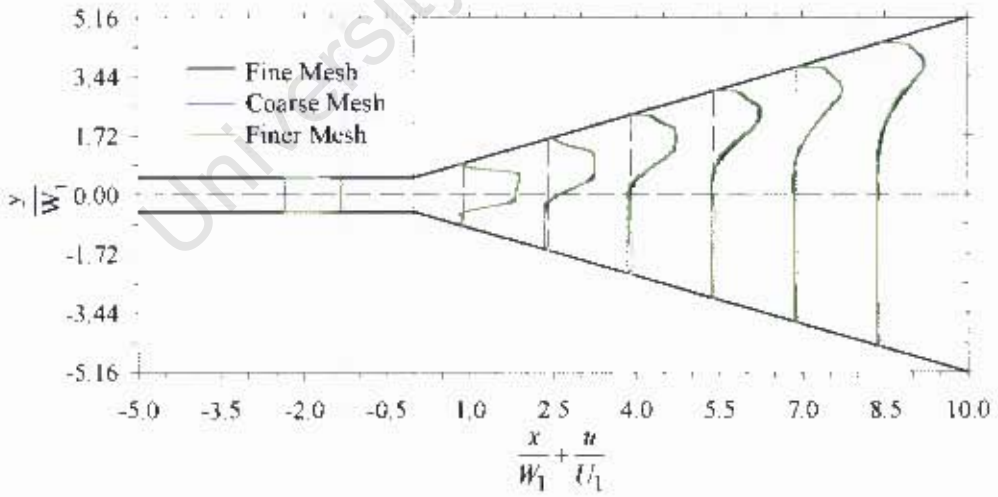

Figure 6.16: Grid convergence test on velocity profiles

6.17, were 1.86% and 1.02%, respectively. These discrepancies are within

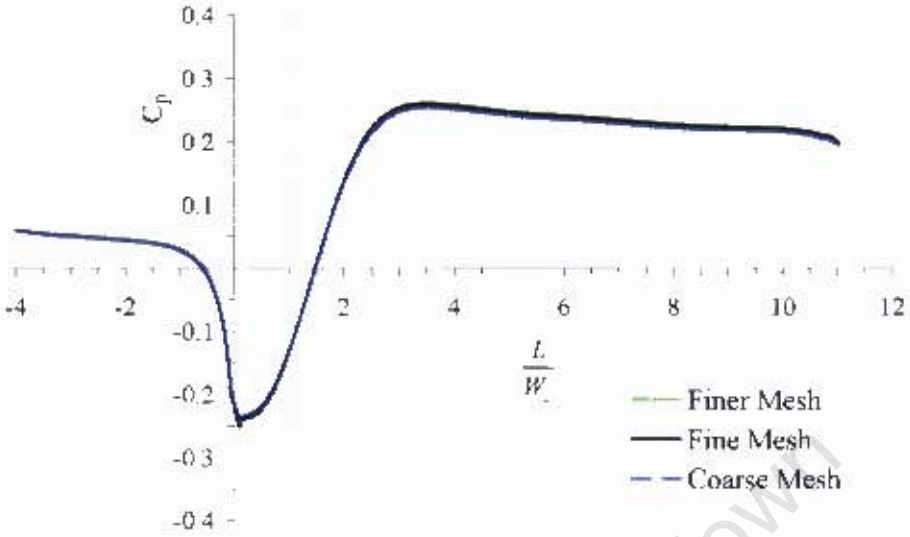

Figure 6.17: Grid convergence test on C_p

the uncertainties of the experiment and hence the grid refinement was considered to have converged. The 'coarse' mesh however produced y^+ values much higher than 1 as can be seen in figure 6.18 indicating that solution in the viscous sub-layer may not be well resolved for this mesh. Therefore the 'fine' mesh, whose total number of cells were half those of the 'finer' mesh and $y^+ \approx 1$, was used in all subsequent computations.

6.3.2 Discretization scheme

A good numerical solution should not depend on the scheme used to discretize the transport equations, especially when the schemes are of the same order of accuracy. Figures 6.19 and 6.20 show the discretization convergence tests for the axial velocity profiles, and C_p, respectively. Even, though prediction given by first order accurate schemes, i.e. the first order upwind and power law schemes differ from those of the higher order schemes, the predictions by these first order accurate schemes are almost indistinguishable from each other. The same can be said about the higher order schemes

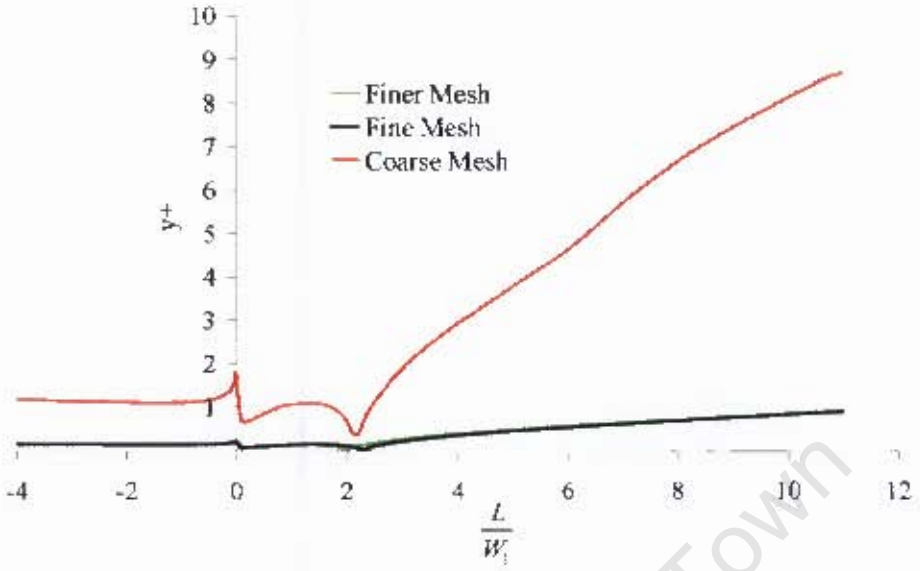

Figure 6.18: The y^+ values for the 50° diffuser

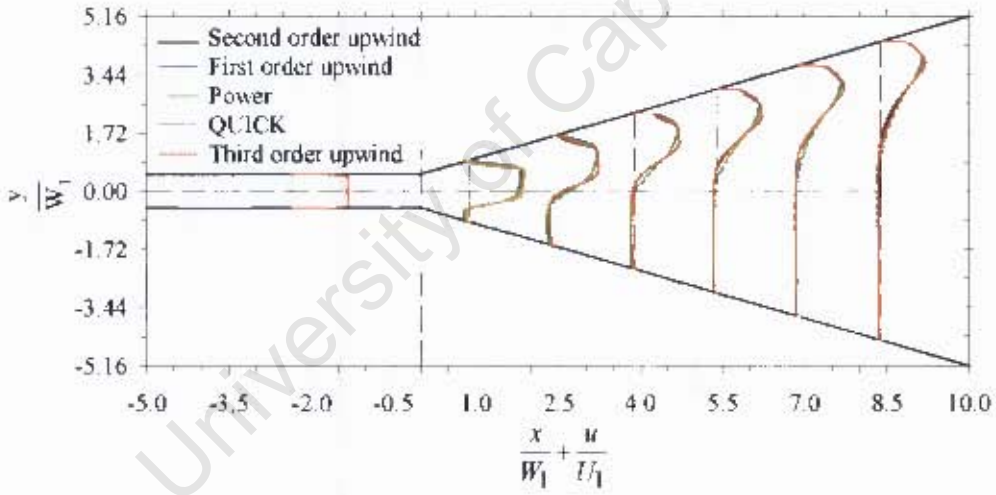

Figure 6.19: Discretization scheme convergence for velocity profiles

both for the velocity profiles and the static pressure recovery. However, since more computational effort was required for the third order scheme, it was abandoned in favor of the second order accurate schemes. Lastly, because the second order upwind scheme is a hybrid between the first order central differencing and second order upwind schemes [111], and since the switching

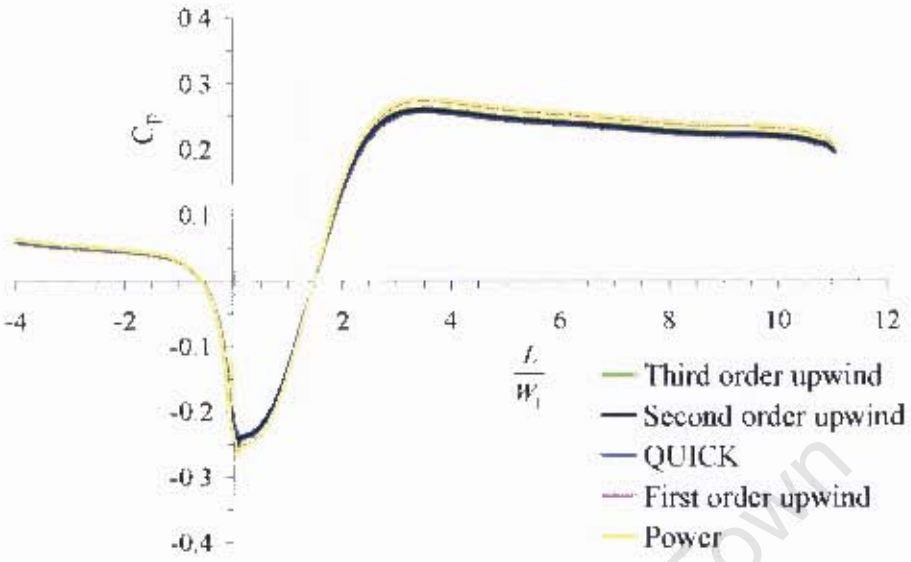

Figure 6.20: Discretization scheme convergence for C_p

between the two schemes is dependent on the value of the Peclet number, it was thought prudent to use the QUICK scheme as it ensured second order accurate solutions at all times.

6.3.3 Models' comparison

The choice of the two-equation eddy viscosity models that give reasonable predictions in APG flows is well supported in the literature as was demonstrated in section 1.3.2. As a result, in this strong APG flows dominated study, four eddy viscosity models were selected, i.e. the Menter SST $k-\omega$, the Wilcox $k-\omega$, the standard $k-\epsilon$, and the realizable $k-\epsilon$ models. Figures 6.21 and 6.22 show the performance of these models in comparison with experimental results for the C_p and velocity profiles, respectively. The discrepancies between these numerical predictions and the experimental results are given in table 6.5.

Even though the prediction errors for the $k-\epsilon$ models are of the same order of magnitude as those by the $k-\omega$ models for the velocity profiles, the

$k-\epsilon$ models over-predicted the C_p values by over 200%. This was however not surprising since this over-prediction was a major concern raised in the 1980-81 AFOSR-HTTM-Stanford Conference on Complex Turbulent Flows [72, 73]. The use of wall functions in the $k-\epsilon$ models is thought to be responsible for this over-prediction since the wall functions used do not apply any correction for pressure gradient effects. But, the pressure gradient effects are the main flow feature in this study. Besides the over-prediction of C_p, the $k-\epsilon$ models fail to capture the separation bubble observed in figure 6.36. Consequently, it was concluded that the $k-\epsilon$ models were not appropriate in modeling these flows and were therefore not considered further.

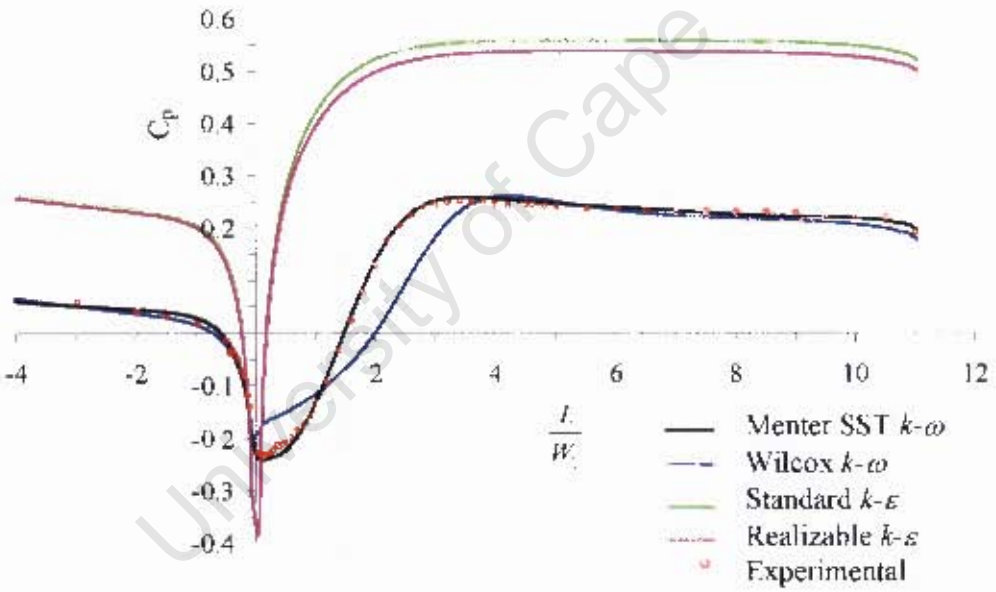

Figure 6.21: Performance of eddy viscosity models in predicting C_p

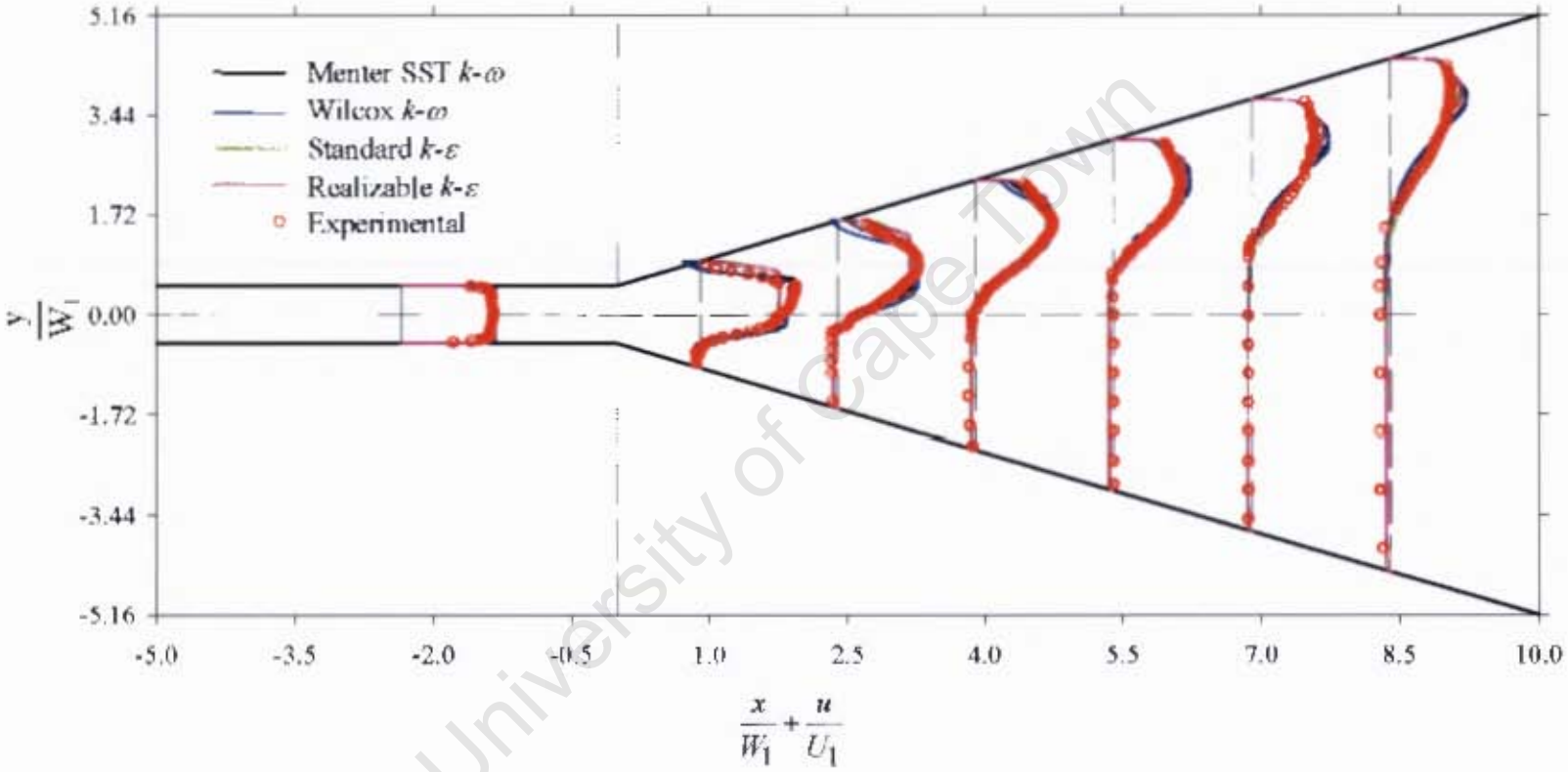

Figure 6.22: Performance of eddy viscosity models in predicting velocity profiles

Table 6.5: Performance of turbulence models

Flow field	Location	SST $k-\omega$	Wilcox $k-\omega$	Std $k-\epsilon$	Realizable $k-\epsilon$
Wall pressure recovery data %error	-	4.05	14.66	233.4	219.7
Velocity profiles % error	Entry	3.63	3.65	3.65	3.65
	Strip 1	7.87	6.82	5.30	5.38
	Strip 2	0.94	2.89	2.01	4.79
	Strip 3	0.37	0.32	0.30	0.38
	Strip 4	5.48	5.46	3.38	5.48
	Strip 5	2.64	2.64	2.64	2.64
	Strip 6	3.85	3.86	3.86	3.86
	Overall	3.54	3.66	3.02	3.74

Compared to the experimental results, the Wilcox $k-\omega$ and SST $k-\omega$ models over-predicted the velocity profiles by 3.66% and 3.54%, respectively. However, the Wilcox $k-\omega$ model under-predicted the C_p value by 14.66%. This behavior is due the absence of the cross-diffusion that is introduced into the SST $k-\omega$ model through the ϵ to ω transformation. The performance of the SST $k-\omega$ model was enhanced further by reducing the production of the turbulent kinetic energy through a reduction of the model coefficient R_β from 8 to 5.5. The effect of adding the cross diffusion into the turbulent diffusion terms of the ω-equation is to reduce the net production of turbulent kinetic energy. Since the production of this turbulent kinetic energy is responsible for the difference in performance between the two models, it was then easier to reduce it directly by modifying the production term of the k-equation.

6.3.4 Reynolds number independence

As in the physical models, it was necessary to check the influence of the Reynolds number on the prediction of these flows. Simulations were performed at Reynolds numbers identical to those of the experiments. In the experiments, the increase of Reynolds number was limited by some physical constraints like the fan speed and the undesirable vibration effects as mentioned earlier. However, such limitations are absent in computational models and therefore the Reynolds number independence tests were performed to include $\mathrm{Re} = 6.53 \times 10^5$, corresponding to an inlet velocity of 60 m/s. As can be seen from figures 6.23 and 6.24, the predictions are almost indistinguishable for both the velocity profiles and C_p. This led to the conclusion that the solution of these diffuser flows were independent of Reynolds number. Henceforth, all the computations, just like in the physical models, were performed at 15 m/s corresponding to a Reynolds number of 2.18×10^5.

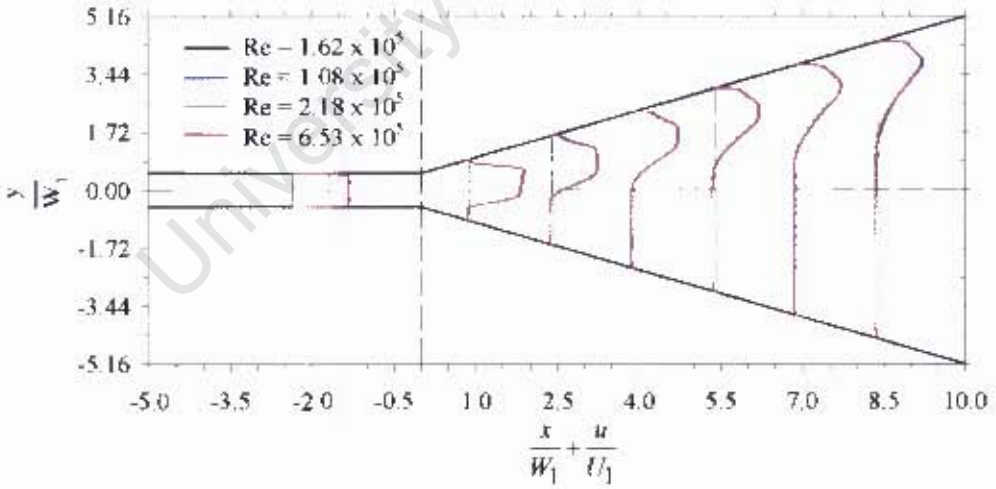

Figure 6.23: Reynolds number dependence test for the velocity profiles

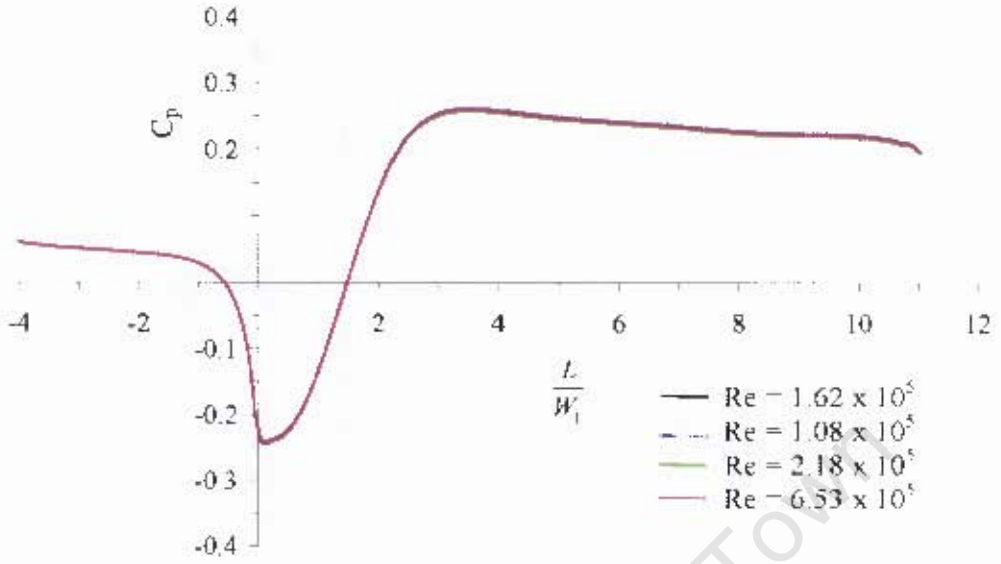

Figure 6.24: Reynolds number dependence test for C_p

6.4 Summary: Experiments vs CFD results

Other available experimental data for verifying the predicted flow data include the v/U_1 and C_p profiles. Figures 6.25 to 6.28 give a complete sample of the data set for the 50° diffuser.

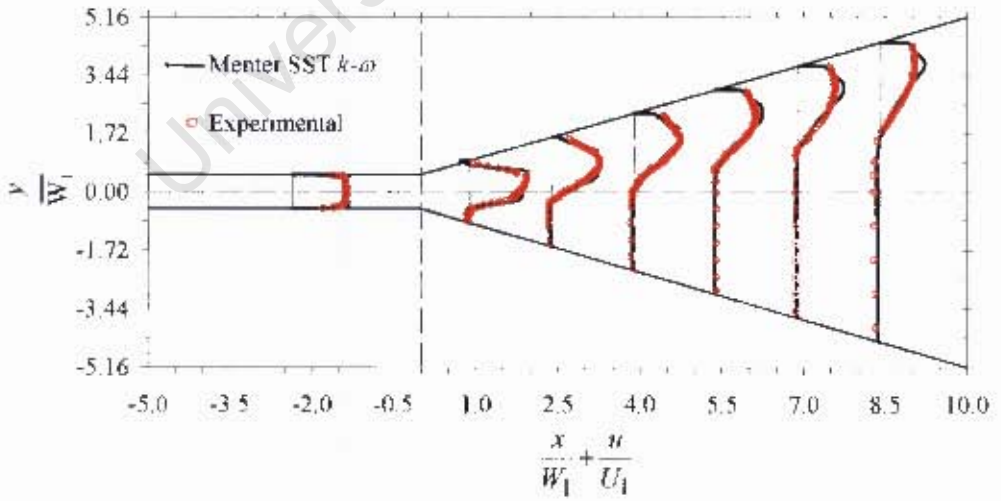

Figure 6.25: Axial velocity profiles for the 50° diffuser

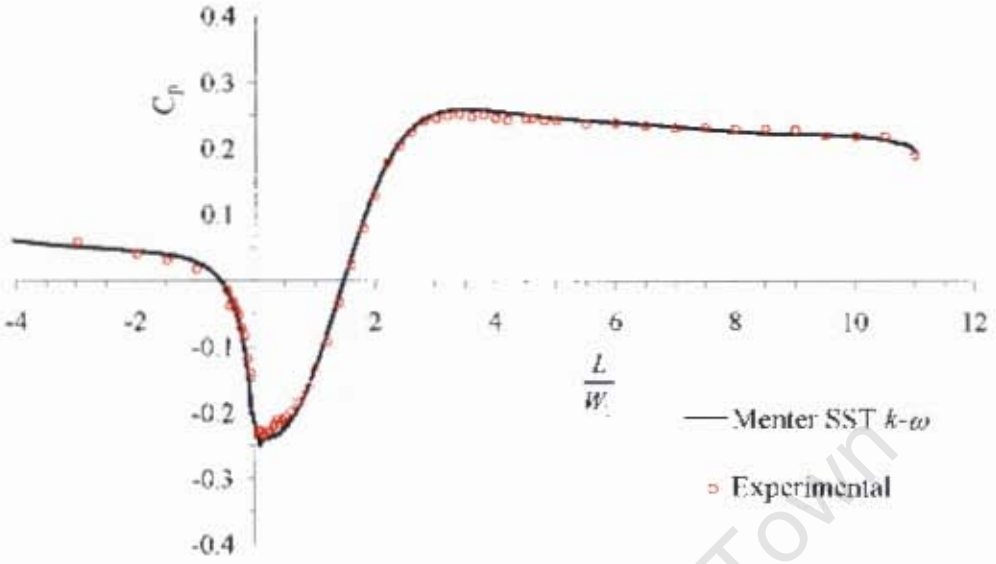

Figure 6.26: Pressure recovery coefficient for the 50° diffuser

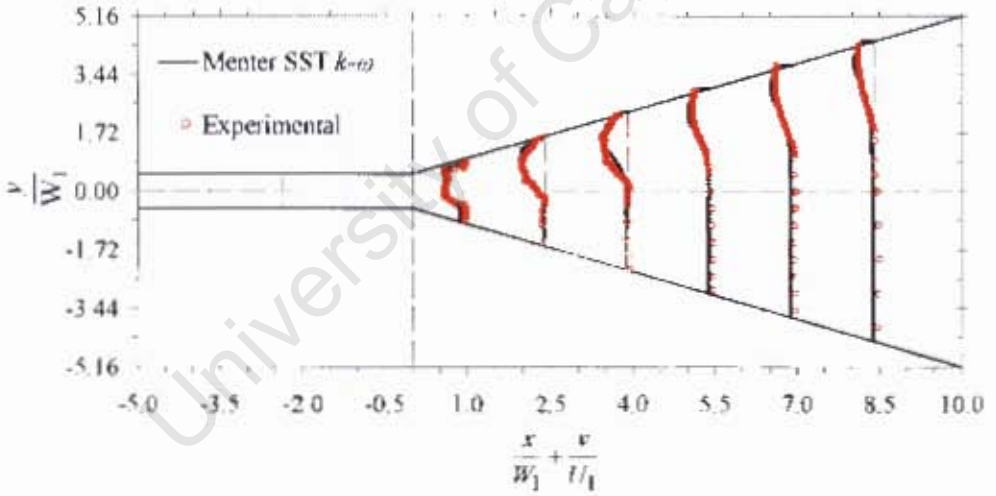

Figure 6.27: Lateral velocity profiles for the 50° diffuser

Similar results are available for the other diffusers as given in appendix A. Table 6.6 summarizes the overall errors arising from the numerical prediction of these parameters for all the diffusers.

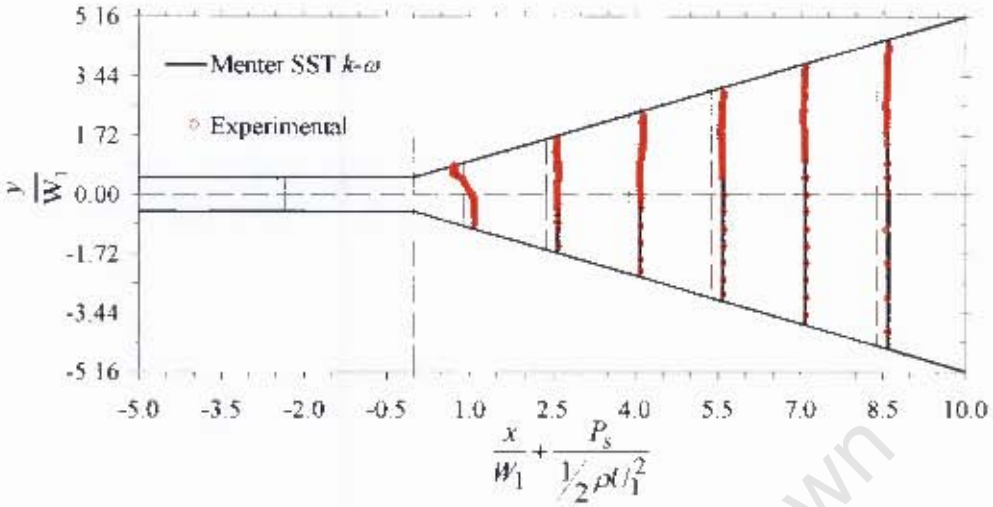

Figure 6.28: Static pressure coefficient profiles for the 50° diffuser

Table 6.6: Prediction of % errors in diffusers

2θ/Parameter	50°	40°	30°
C_p at wall	4.05	3.6	2.71
u/U_1 profiles	3.54	2.80	3.72
v/U_1 profiles	0.97	1.2	0.91
C_p profiles	0.15	0.15	0.15

6.5 Prediction of C_{pr} in unvaned diffusers

Data is available in the literature, (e.g. [1, 3, 7, 12]), for the overall pressure recovery C_{pr} in unvaned diffusers. To verify the prediction of the overall pressure recovery, further computations were performed for 4°, 7°, 10°, 15°, 20°, 28° and 42° diffusers. The grid properties and solution techniques were kept the same as those of the previous computations. The geometries, and flow conditions for the 28° and 42° diffusers were however different from those studied experimentally in this research. Accordingly, the N/W_1 ratio, the inlet hydraulic diameter, and the inlet flow velocity for these two diffusers

were set as 8.35, 0.14 m, and 26 m/s, respectively, so as to correspond to the geometric and flow conditions of the data of Cochran and Kline [4]. The C_{pr} results for these diffusers were then compared with the experimental data of Reneau et. al. [3] and are shown in figure 6.29.

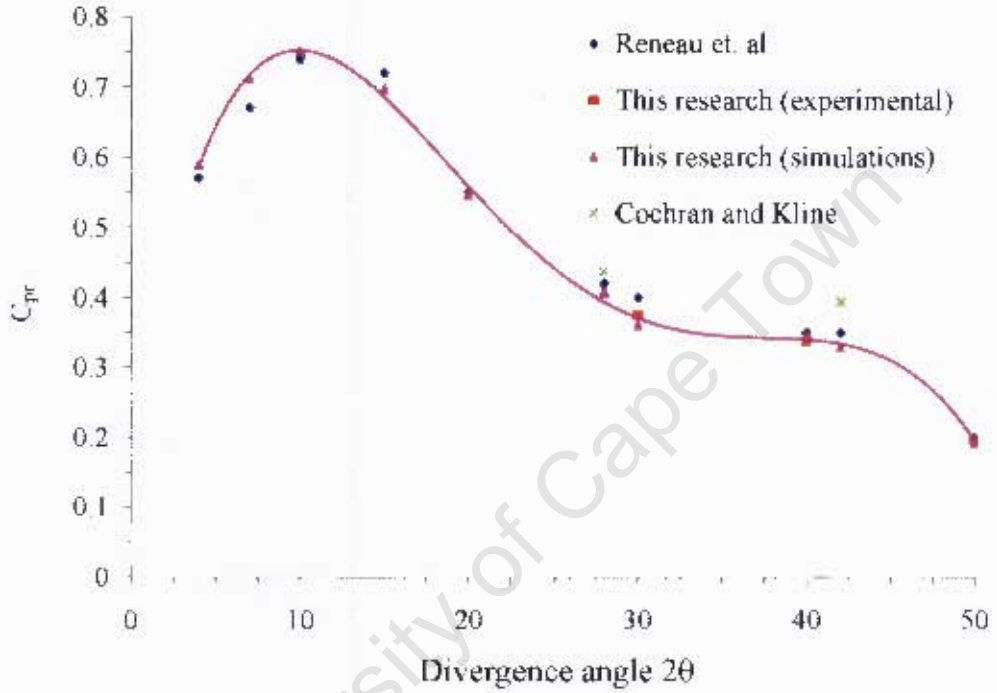

Figure 6.29: Coefficient of pressure recovery data

The maximum C_{pr} was achieved when $2\theta = 11°$ and is in agreement with the results of Reneau et al. for diffusers with similar inlet blockage factors. For diffusers within $30° < 2\theta < 42°$, the C_{pr} values are little affected by changes in θ as the $C_{pr} - 2\theta$ curve levels off. However, beyond this range, there is a sudden drop in C_{pr}. It is expected from this discontinuity that the wall C_p profiles must then show a different trend as can be observed from the experimental results of the wall C_p plot in figure 6.30.

This sudden change in pressure recovery data is due to the presence of the inlet separation bubble, observed in the 50° diffuser (see figure 6.33) but

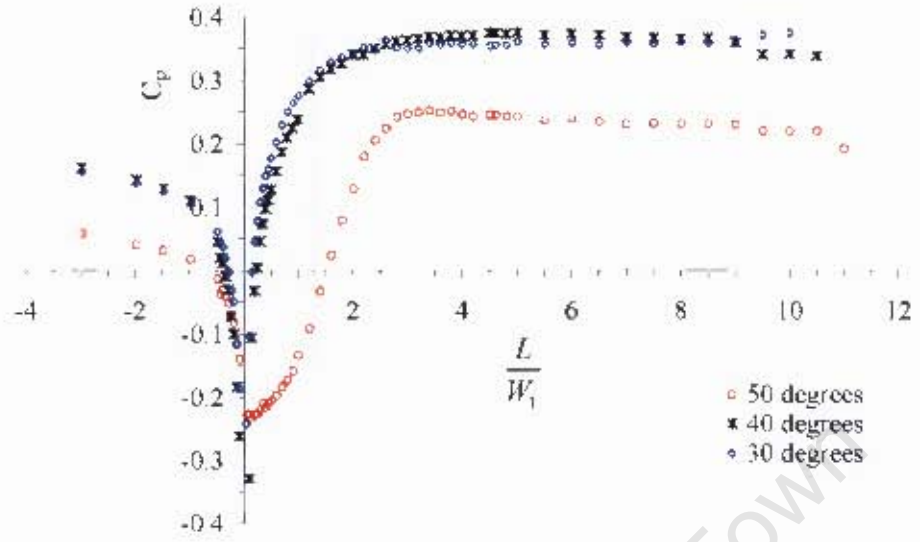

Figure 6.30: Experimental wall C_p for all angles

absent in the 30° and 40° diffusers as can be seen in figure 6.31.

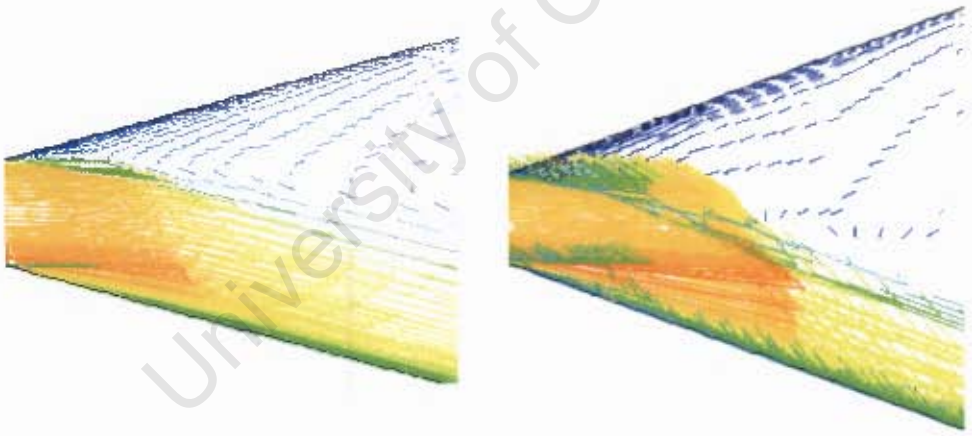

Figure 6.31: Velocity vectors for the 30° and 40° diffusers

The separation bubble, thought of as a limiting case between the recirculating region of the backward facing step (sudden expansion) and attached flow, certainly changes the flow field behavior even beyond its reattachment point.

The experimental and computational results from the current research

are in agreement with the Reneau et al. data to within 4.74% and 3.71% respectively.

6.6 Prediction of C_{pr} in vaned diffusers

Computations with the inlet vanes were performed on 28°, 30°, 40°, 42°, and 50° diffusers. This is because they are the only ones whose experimental data for verification of the numerical solutions is available (from [4] and the current research). Near the vanes' surfaces, the grid properties were matched to those of the diffuser walls to ensure that the y^+ values in the entire flow-field remained close to 1. Figure 6.32 shows the improvement in pressure recovery achieved due to the use of inlet vanes. Based on the unvaned diffuser results of Reneau et al. [3], all the diffusers increased their C_{pr} values by over 75%. Cochran and Kline [4] have shown that the improvement in pressure recovery

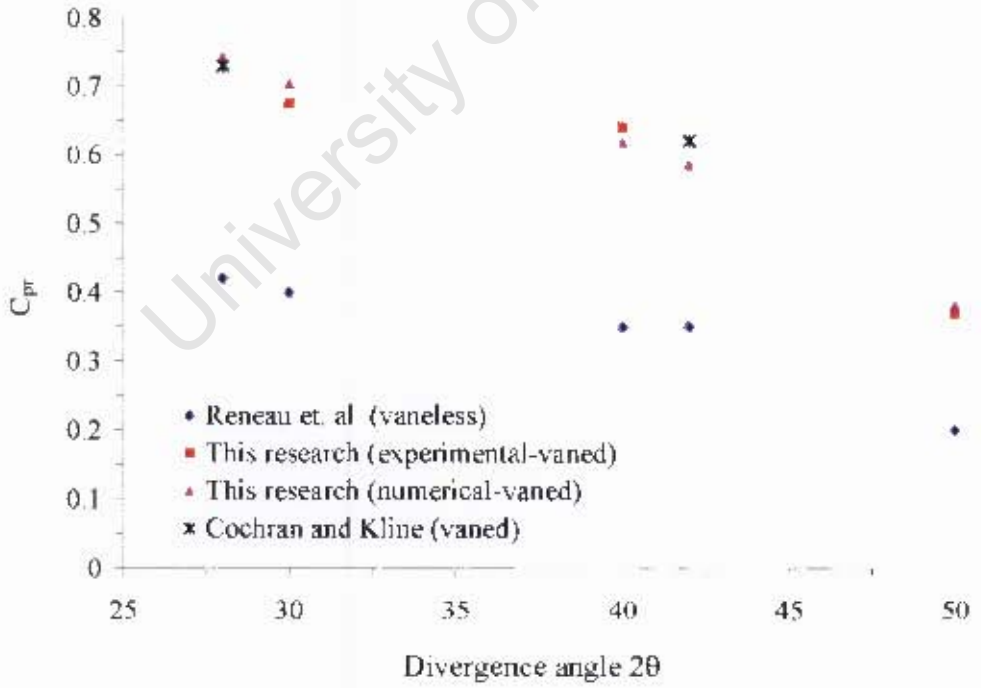

Figure 6.32: Coefficient of pressure recovery data for vaned diffusers

in diffusers depends on the ratio of the diffuser length to the vane length. For this reason, no direct comparison of experimental results for vaned diffusers can be made due to the difference in geometries of the two sets of experiments. However, the computed data for vaned diffusers has an error of 3.56% and 3.71%, compared to the experimental results from the current research, and those from Cochran and Kline, respectively. This is a promising indication that the vaned diffuser flows can be well resolved with the current solution techniques and turbulence model. It is however important that more physical testing, which should include both the velocity and pressure fields, should be carried out before conclusions about performance of the turbulence model can be drawn.

6.7 Prediction of the effective flow geometry

In wide-angled diffuser flows, the magnitude of the velocities in the stalled region is much lower than those in the unstalled region. From one dimensional flow theory considerations, higher diffuser exit effective areas correspond to higher pressure recoveries. Thus, for prediction of the pressure recovery, the effective flow area, especially at the exit, is critical. The velocity profiles presented so far, and inspection of the velocity vectors in figure 6.33, suggest the existence of an imaginary streamline that defines the transition between regions of stalled and unstalled flow. This streamline corresponds to the imaginary line of all the points where $u = 0$, measured while probing the velocities between the left and right walls of the diffusers as described below.

The distances of all the six roof strips from the diffuser entry point in the x direction were known, and hence the width of each strip W_x, was evaluated according to Eq.6.2. The calculated width W_x, was used to normalize distances measured in the y direction about the x-axis for each strip. A

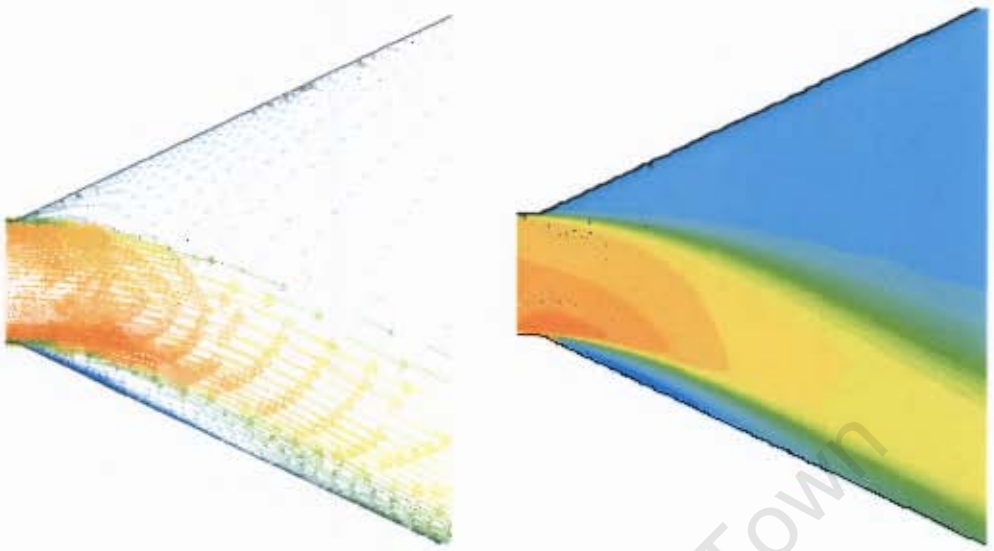

Figure 6.33: Velocity vectors and contours for the 50° diffuser

normalized length scale ξ, was then defined and is given in Eq.6.2.

$$W_x = 2x\tan\theta + W_1 \qquad \xi = \frac{y}{W_x} \tag{6.2}$$

Thus, for each strip, a different length was used to normalize the data points in the y direction, resulting in normalized distances of the data points falling in the range $-0.5 < \xi < +0.5$.

The velocity profiles u/U_1, for all the strips can then be plotted on the same graph. This post-processing procedure was performed on the data for all the diffusers and the resulting graphs, similar in appearance to figure 6.34, are given in appendix A. This data set shows that asymmetry of the flow in diffusers begins when the divergence angle is above 15°. Reverse flow was only observed in the 50° diffuser as can be seen from the plot of the $x/W_1 = 0.9$ in figure 6.34. From this figure, it is seen that along the left hand portion of each data set corresponding to the different strips, a linear section exists, which intercepts with the abscissa ξ. This intercept gives the location at which the axial velocity u reverses.

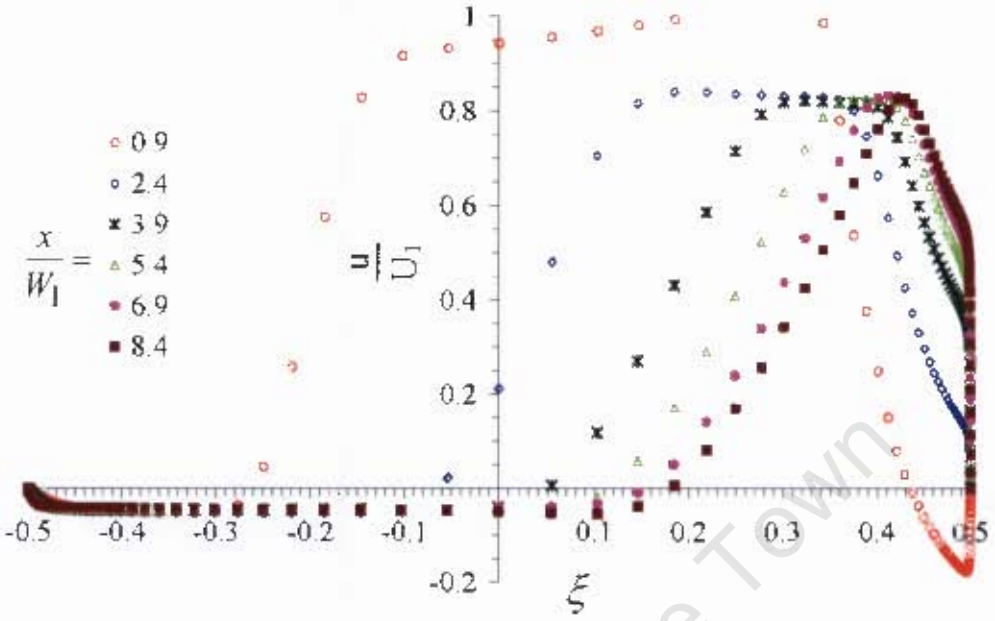

Figure 6.34: Normalized velocity profiles for the 50° diffuser

At each strip, this intercept is unique and can be denoted as ξ_r. The streamline that is defined by joining ξ_r must then describe the edge of the transition line between regions of unstalled and stalled flow. Six values of ξ_r were obtained for each strip, and eventually for all the angles. Figure 6.35 shows a plot of these values against the normalized axial distance x/W_1.

Inspection of figure 6.35 suggests the existence of an exponential relationships between these parameters for $20° \leq 2\theta \leq 50°$, which through curve fitting techniques and computer optimization of the coefficients, were correlated to give Eq.6.3.

$$\xi_r = \varsigma_1 \ln\left(\frac{x}{W_1}\theta^2\right) - \frac{1}{\varsigma_1}\ln\frac{1}{\varsigma_2} \quad \text{for} \quad 20° < 2\theta < 50° \tag{6.3}$$

where the coefficients ς_1 and ς_2 are;

$$\begin{aligned} \varsigma_1 &= \frac{1}{7.4 - 0.1\theta} \\ \varsigma_2 &= \left(0.73\theta^2 + 1323\right)\theta^2 - \left(51.2\theta^2 + 14764\right)\theta + 61291 \end{aligned} \tag{6.4}$$

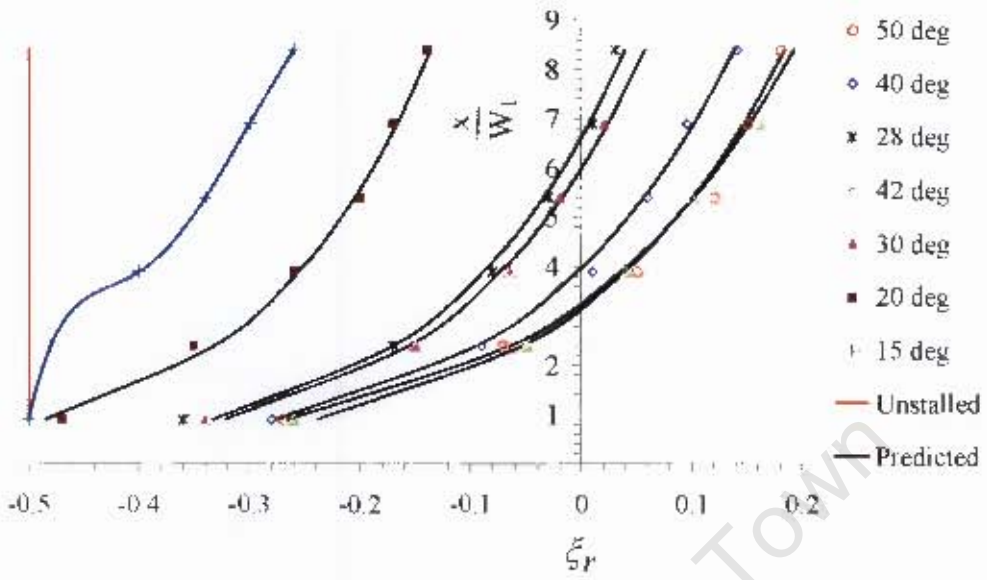

Figure 6.35: Reversal points ξ_r for diffusers

The limiting case of $\xi_r = -0.5$ occurs for unstalled diffusers. Results for diffusers that are in the transitory flow regime tend to blend between the limiting case nearer the diffuser inlet and the exponential profile of the fully stalled flow regime further downstream of the inlet, as the curve for the 15° diffuser in figure 6.35 shows. The reason for this behavior is that, as will be demonstrated shortly, separation of flow on the stalled wall does not take place at the diffuser entry for the diffusers that are in a transitory flow regime.

For wide-angled diffusers therefore, if the ratio x/W_1 is known, the effective width of flow $0.5 - \xi_r$, as shown in figure 6.36 can be evaluated. The mapping of the effective flow area includes locating the separation bubble as can be seen from the velocity vectors plot near the inlet shown in figure 6.37. From a boundary layer theory view point, separation of the flow at the wall occurs when the wall shear stress becomes zero. Precisely, at the point of stall $\partial u/\partial x = 0$. Thus, if the wall shear stress was to be resolved into its x and y components, then this boundary condition is equivalent to setting the

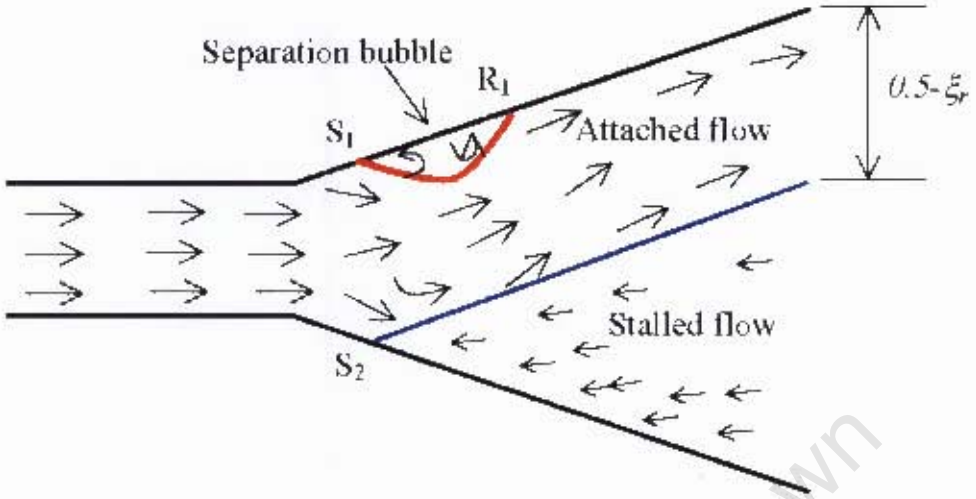

Figure 6.36: Effective flow-field for wide angled diffusers

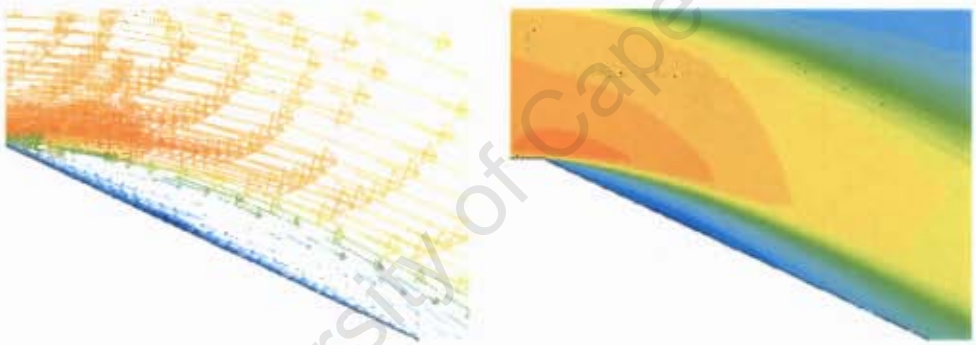

Figure 6.37: Separation bubble on the unstalled wall

x-wall shear stress to zero. The x-wall shear stress can be normalized by the inlet dynamic pressure to obtain a skin friction coefficient C_{fx}, resolved in x direction. The point of separation is then that point along the wall when $C_{fx} = 0$.

For all the diffusers, C_{fx} was plotted against x/W_1 and the graphs presented in appendix A. Figures 6.38 and 6.39 show representative graphs of these plots.

The location of point S_1 and R_1 in figure 6.36 correspond to the points on the curve when $C_{fx} = 0$ on the unstalled wall. Point S_2 corresponds

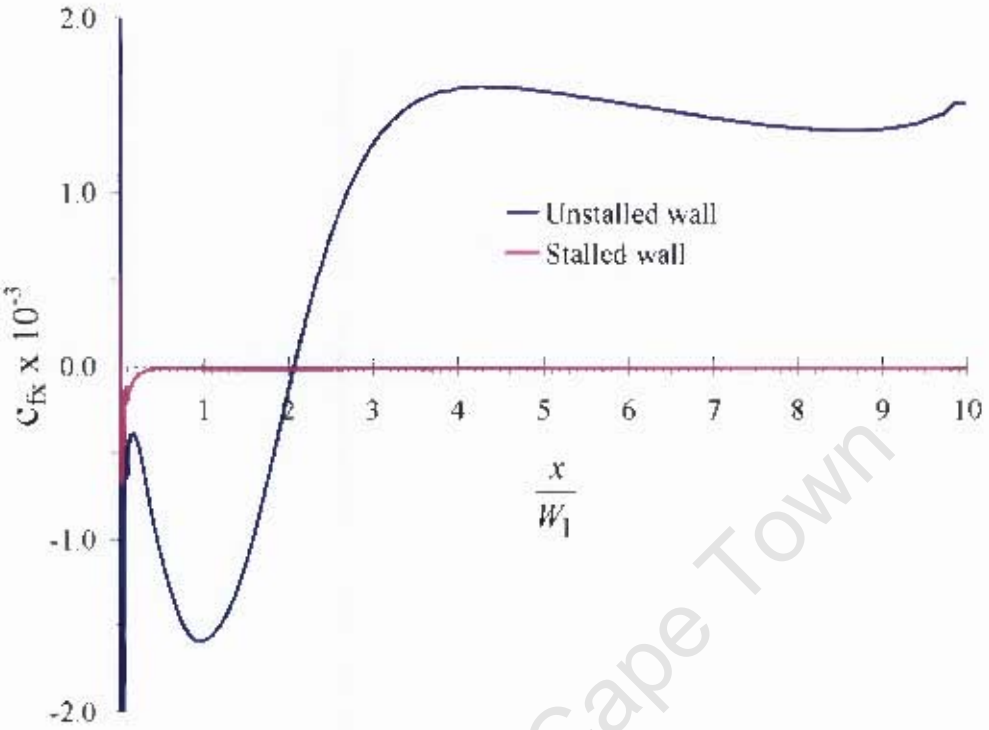

Figure 6.38: x-shear stress coefficient for the 50° diffuser

to the location when $C_{fx} = 0$ on the stalled wall. Figure 6.39 shows that separation on the stalled wall does not necessarily take place at the diffuser entry especially for diffusers that are in the transitory flow regime. However, it can be observed from figure 6.38 and the graphs in appendix A that for flows in the fully stalled flow regime, separation on the stalled wall always occurs at the diffuser entry.

With the aid of Eq.6.3, the effective flow area for wide-angled diffusers that are in the fully stalled regime, as represented in figure 6.36, can be mapped and are summarized in table 6.7. The average of the errors between the calculated and measured effective flow areas that results from such mapping is less than 6%.

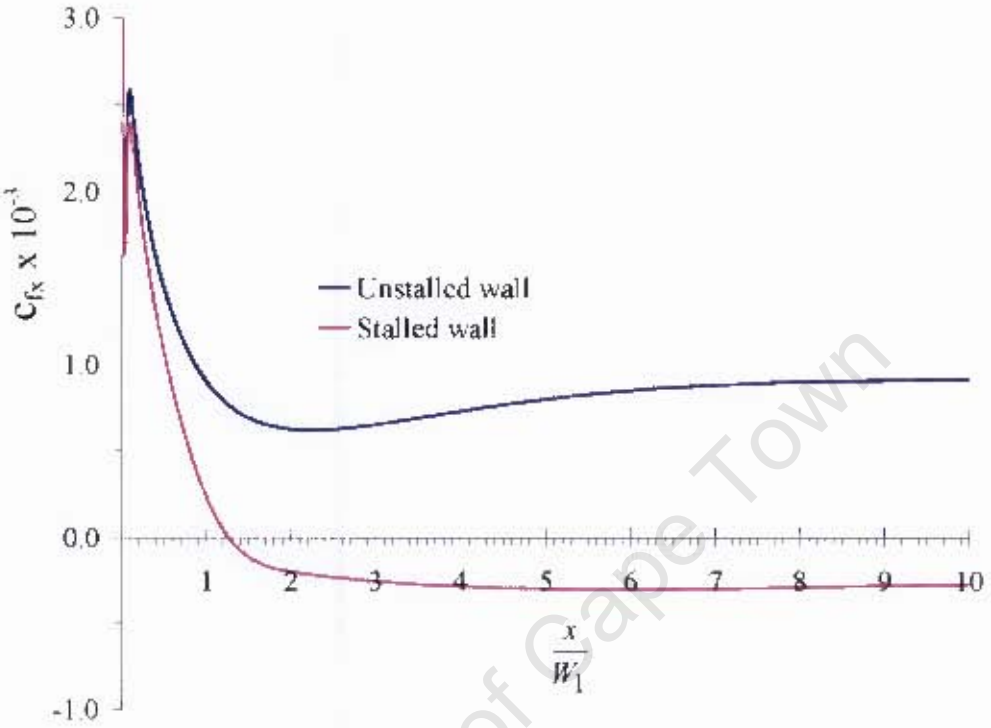

Figure 6.39: x-shear stress coefficient for the 15° diffuser

Table 6.7: Mapping of the flow-field

2θ	15°	20°	28°	30°	40°	42°	50°
S_1	0	0	0	0	0	0	0
R_1	0	0	0	0	0	0	2.1
S_2	1.3	0.2	0	0	0	0	0
ξ_r at exit	-	-0.11	0.04	0.09	0.17	0.18	0.23
% error in ξ_r	-	2.98	8.18	8.00	1.15	5.14	6.83

Chapter 7

Conclusions

In this study, experimental and numerical investigations of separated flows in fully stalled wide-angled diffusers have been carried out. Due to the adverse pressure gradient along the diffuser walls, flow separated from one diverging wall and became attached to the other wall, thus forming a region of steady stall within each diffuser. It was not possible to determine in advance, the wall to which the flow would attach. Tests to determine the wall to which the flow remains attached led to the conclusion that the wall of preference was totally random and was probably caused by a slight upstream disturbance that was impossible to detect. The computational models also displayed this physical behavior.

However, in the physical models, it was possible to 'switch' the flow from one wall to the other by introducing an inlet disturbance. It was found that once 'switched' to a wall, the flow remained attached to that wall permanently. Experimental results showed that regardless of the wall to which the flow was attached, both the velocity and pressure flow-fields were replicated with discrepancies below 2%. The static pressure displayed a greater sensitivity to an increase in divergence angle.

Although current literature states that for a given geometry, the Reynolds

number has little influence on the static pressure recovery, it was found in this study that by increasing the velocity from 10 m/s to 20 m/s, the static pressure recovery for the 30° diffuser increased by 8.31%. However, as the divergence angle was increased, a similar increase in Reynolds number resulted in a higher percentage of pressure recovery. The limited range of Reynolds numbers investigated in this study could not allow a rational correlation between the Reynolds number and the C_{pr} profiles. This range was limited by the physical constraints imposed by the wind tunnel and fan speed. For instance, a change of velocity from 10 m/s to 80 m/s would not change the Reynolds number by even one order of magnitude.

The experimental uncertainties in this research were approximately 2%. Within these uncertainties a reliable data bank contribution has been provided for unvaned fully stalled wide-angled diffusers. The parameters in the data bank include the wall static pressure recovery data, axial and lateral velocity profiles and static pressure profiles. Velocity profiles that are plotted on the proposed normalized length scale together with the skin friction coefficients have also been included in the data bank.

The design criteria utilizing short, flat, vane installations at the inlet as proposed by Cochran and Kline [4] was checked over a range of angles. A marked improvement in pressure recovery, with C_{pr} increasing by more than 75% in this high pressure loss regime of the fully developed stall, was achieved.

Four eddy viscosity models were used to predict the diffusers' flows, namely; the standard $k-\epsilon$, realizable $k-\epsilon$, Wilcox $k-\omega$ and Menter SST $k-\omega$ models. All four models showed comparable performance in the prediction of the velocity profiles. The $k-\epsilon$ models however consistently over-predicted C_{pr} by more than 200%. This was due to the use of the wall

functions incorporated in the $k-\epsilon$ models in the near-wall region. The wall functions do not account for any pressure gradient effects, which are the main flow features of this study. The $k-\epsilon$ models even failed to predict the separation bubble that had been observed to appear on the unstalled wall near the entry for the 50° diffuser.

The variants of the $k-\omega$ turbulence model gave comparable results in the velocity field but again differed in their prediction of the wall static pressure. The Wilcox $k-\omega$ model under-predicted the wall static pressure by 14.66%, a behavior thought to be as a result of high production of turbulent kinetic energy in the k-equation caused by a lack of cross-diffusion in the ω-equation. The SST $k-\omega$ model therefore emerged as the best overall model. A little modification to the k-equation of the SST $k-\omega$ models resulted in the model predicting the static pressure data and velocity fields to within a maximum error of 4%. The lateral velocity and static pressure profiles were predicted to within 1% and 0.15%, respectively.

Other diffuser geometries were included so that predicted overall pressure recovery could be compared with the results of Reneau et.al [3]. For constant inlet duct aspect ratio and N/W_1 ratio, the maximum C_{pr} was predicted to occur in a 11° diffuser. The trend measured by Reneau et.al for variation of C_{pr} with θ was reproduced to within 3.71%. Prediction errors for C_{pr} in the vaned diffusers, were 3.56% compared to the experimental results of the current research and 3.71% compared to the results of Cochran and Kline [4] for similar geometries.

A simple correlation for determining the effective flow areas for fully stalled diffusers has been proposed. When used together with the separation bubble mapping, separation points on the unstalled and stalled walls, and reattachment point on the unstalled wall can be mapped. Thus, if the

effective flow area is predicted in advance, then it is promising that one-dimensional flow theory together with the boundary layer equations can be used to provide useful information in stalled APG flows.

Finally, the Menter SST $k-\omega$ model was found to be adequate in predicting fully stalled flows in wide-angled diffusers.

Chapter 8

Future Outlook

Results obtained and presented in this research indicate that the dependence of pressure and velocity profiles on Reynolds number disagrees with the literature. The numerical pressure recovery profiles were independent of Reynolds number in the range studied, but that the experimental profiles were not, with a greater C_p at higher Reynolds number. Nevertheless the differences in C_p are of the order of only 3% across a factor of two in Reynolds number and increases with increase in the divergence angle. It is recommended that this dependence on Reynolds number be investigated to establish a clear relationship between these parameters.

The velocity measurements of the reversed flow on the stalled side of the diffusers were of smaller magnitude compared to the attached flow. In this region the accuracy of the velocity measurements using the intrusive probe is suspect. It is recommended that in future non-intrusive techniques for both velocity measurements and flow visualization be used. Further, to give the complete flow structure, future measurements should include turbulence whereby the microscale energy spectrum and momentum transfer in the diffuser can be established.

The random nature of the choice of wall to which the flow attaches has

been observed in both the numerical simulations and experimental work. It is suspected that in the physical models, the wall to which the flow attaches is determined by the quasi-random turbulent initial conditions which varies in a quasi-random manner from experiment to experiment. However, there is no plausible explanation why in the computational models running under similar initialization, numerical scheme and mesh, the wall should be random from run to run. This requires further investigation.

Finally, as discussed in the thesis, it is only due to constraints in computational capacity that simulations were performed in a two dimensional space using two equation models. It is recommended that future work should extend to three dimensional space using the more robust models like RSM and LES.

References

[1] R. Fox and S. Kline, "Flow regime data and design methods for curved subsonic diffusers," *Transactions of the ASME, Journal of Basic Engineering*, vol. 84, pp. 303–312, 1962.

[2] J. Ashjaee and J. Johnston, "Straight walled, two-dimensional diffusers-transitory stall and peak pressure recovery," *Transactions of the ASME, Journal of Fluids Engineering*, vol. 102, no. 4, pp. 275–282, 1980.

[3] L. Reneau, J. Johnston, and S. Kline, "Performance and design of straight, two-dimensional diffusers," *Transactions of the ASME, Journal of Basic Engineering*, vol. 89, no. 1, pp. 141–150, 1967.

[4] D. Cochran and S. Kline, "Use of short flat vanes for producing efficient wide-angle two dimensional subsonic diffusers," technical report 4309, NACA, 1958.

[5] C. Moore and S. Kline, "Some effects of vanes and turbulence in two-dimensional wide-angle diffusers," technical report 4080, NACA, 1958.

[6] O. Feil, "Vane systems for very-wide -angle subsonic diffusers," *Transactions of the ASME, Journal of Basic Engineering*, vol. 86, pp. 759–765, 1964.

[7] E. Reid, "Performance characteristics of plan-wall two-dimensional diffusers," technical report 2888, NACA, 1953.

[8] S. Kline, "On the nature of stall," *Transactions of the ASME, Journal of Basic Engineering*, vol. 81, pp. 305–321, 1959.

[9] C. Smith, "Transitory stall time-scales for plane-wall air diffusers," *Transactions of the ASME, Journal of Fluids Engineering*, vol. 100, no. 1, pp. 133–135, 1978.

[10] C. Smith and S. Kline, "An experimental investigation of the transitory stall regime in two-dimensional diffusers," *Transactions of the ASME, Journal of Fluids Engineering*, vol. 96, pp. 275–282, 1974.

[11] B. Waitman, L. Reneau, and S. Kline, "Effects of inlet conditions on performance of two-dimensional diffusers." *Transactions of the ASME, Journal of Basic Engineering*, vol. 83, no. 3, pp. 349–360, 1961.

[12] S. Kline, D. Abbort, and R. Fox, "Optimum design of straight-walled diffusers," *Transactions of the ASME, Journal of Basic Engineering*, vol. 81, pp. 321–331, 1959.

[13] C. Sagi and J. Johnston, "The design and performance of two-dimensional, curved diffusers: Part I - Exposition of method," *Transactions of the ASME, Journal of Basic Engineering*, vol. 89, pp. 715–731, 1967.

[14] J. Norbury, "Some measurements of boundary-layer growth in a two-dimensional diffuser," *Transactions of the ASME, Journal of Basic Engineering*, vol. 81, pp. 285–296, 1959.

[15] J. Johnston and C. Powars, "Some effects of inlet blockage and aspect ratio on diffuser performance," *Transactions of the ASME, Journal of Basic Engineering*, vol. 91, pp. 551–553, 1969.

[16] O. McMillan and J. Johnston, "Performance of low-aspect ratio diffusers with fully developed turbulent inlet flows - Some experimetal results," *Transactions of the ASME, Journal of Fluids Engineering*, vol. 95, no. 3, pp. 385–392, 1973.

[17] S. Wolf and J. Johnston, "Effects of non-uniform inlet velocity profiles on flow regimes and performance in two-dimensional diffusers." *Transactions of the ASME, Journal of Basic Engineering*, vol. 91, no. 3, pp. 462–474, 1969.

[18] K. Kaiser and A. McDonald, "Effect of wake-type non-uniform inlet velocity profiles on first appreciable stall in plane-wall diffusers," *Transactions of the ASME, Journal of Fluids Engineering*, vol. 102, no. 3, pp. 283–289, 1980.

[19] P. Kibicho, T. Suzuki, and R. Waka, "Study on subsonic two-dimensional diffuser flows," *Journal of Agriculture Science and Technology*, vol. 3, no. 2, pp. 68 – 83, 2001.

[20] P. Kibicho and A. Sayers, "Velocity and static pressure profiles in wide angled two-dimensional stalled diffuser flows," in *Fluid Structure Interaction 2005*, (La Coruna, Spain), 19th-21st September 2005.

[21] P. Runstadler and R. Dean, "Straight channel diffuser performance at high inlet mach numbers," *Transactions of the ASME, Journal of Basic Engineering*, vol. 91, pp. 397–422, 1969.

[22] J. Hoffmann, "Effects of free-stream turbulence on diffuser perfromance," *Transactions of the ASME, Journal of Fluids Engineering*, vol. 103, no. 3, pp. 385–390, 1981.

[23] Y. Furuya, T. Sato, and T. Kushida, "The loss of flow in the conical diffusers with suction at the entrance," *Bulletin of JSME*, vol. 9, no. 33, pp. 131–137, 1966.

[24] Y. Furuya, T. Fujimoto, and E. Yamazato, "Performance of two-dimensional diffusers with suction at the entrance," *Bulletin of JSME*, vol. 13, no. 56, pp. 264–271, 1970.

[25] Y. Senoo and M. Nishi, "Improvement of the performance of conical diffusers by vortex generators," *Transactions of the ASME, Journal of Fluids Engineering*, vol. 96, pp. 5–10, 1974.

[26] J. Carlson, J. Johnston, and C. Sagi, "Effects of wall shape on flow regimes and performance in straight, two-dimensional diffusers," *Transactions of the ASME, Journal of Basic Engineering*, vol. 89, no. 1, pp. 151–160, 1967.

[27] S. Raghunathan and R. Cooper, "Passive boundary layer control with slots in short diffusers," *Transactions of the ASME, Journal of Fluids Engineering*, vol. 122, no. 1, pp. 177–179, 2000.

[28] L. Reneau and J. Johnston, "A performance prediction method for unstalled, two-dimensional diffusers," *Transactions of the ASME, Journal of Basic Engineering*, vol. 89, no. 3, pp. 643 654, 1967.

[29] O. McMillan and J. Johnston, "Performance of low-aspect ratio diffusers with fully developed turbulent inlet flows - Development and application of a performance prediction method," *Transactions of the ASME, Journal of Fluids Engineering*, vol. 95, pp. 393–400, 1973.

[30] R. Woolley and S. Kline, "A procedure for computation of fully stalled flows in two dimensional passages," *Transactions of the ASME, Journal of Fluids Engineering*, vol. 100, no. 2, pp. 180–186, 1978.

[31] G. Chui and S. Kline, "Investigation of a two-dimensional, fully stalled, turbulent flow field," Tech. Rep. MD-19, Thermosciences Div., M.E. Dept, Stanford University, 1967.

[32] S. Ghose and S. Kline, "The computation of optimum pressure recovery in two-dimensional diffusers," *Transactions of the ASME, Journal of Fluids Engineering*, vol. 100, no. 4, pp. 419–426, 1978.

[33] W. Wysocki and Z. Kazimierski, "Analysis of subsonic transitory stalled flows in straight walled diffusers," *Transactions of the ASME, Journal of Fluids Engineering*, vol. 108, no. 2, pp. 222–226, 1986.

[34] M. Vujicic and C. Crnojevic, "Calculation of the separation point for the turbulent flow in plane diffusers," *Mechanics, Automatic Control and Robotics*, vol. 3, no. 15, pp. 1001–1006, 2003.

[35] M. Vujicic and C. Crnojevic, "Calculation of the turbulent flow in a plane diffuser by using the integral method," *FME Transactions*, vol. 31, pp. 69–74, 2003.

[36] J. Bardina, A. Lyrio, S. Kline, J. Ferziger, and J. Johnston, "A prediction method for planar diffuser flows," *Transactions of the ASME, Journal of Fluids Engineering*, vol. 103, no. 2, pp. 315–321, 1981.

[37] J. Johnston, "Review: Diffuser design and performance analysis by unified integral method," *Transactions of the ASME, Journal of Fluids Engineering*, vol. 120, no. 1, pp. 6–17, 1998.

[38] S. Pope. "The calculation of turbulent recirculating flows in general orthorgonal coordinates," *Journal of Computational Physics*, vol. 26, no. 2, pp. 197–217, 1978.

[39] M. Habib and J. Whitelaw, "The calculation of turbulent flow in wide-angled diffusers," *Numerical Heat Transfer*, vol. 5, pp. 145–164, 1982.

[40] S. Obi, K. Aoki, and S. Masuda, "Experimental and computational study of separating flow in an asymmetric planar diffuser.," in *9th Symposium on turbulent shear flows*, vol. 305, (Kyoto, Japan), pp. 1–4, 1993.

[41] C. Buice and J. Eaton, "Experimental investigation of flow through an asymmetric plane diffuser," Report No. TSD 107, Center for Turbulence Research, Stanford University, 1997.

[42] S. Gullman, O. Tornblom, B. Lindgren, G. Amberg, and A. Johanson, "Numerical and experimental study of separated flow in a plane asymmetric diffuser," *International Journal of Heat and Fluid Flow*, vol. 25, no. 3, pp. 451–460, 2004.

[43] S. Gullman, *Turbulence and Scalar Flux Modelling Applied to Separated Flows*. Phd thesis, Royal Institute of Technology, 2004.

[44] S. Lim and H. Choi, "Optimal shape design of a two-dimensional asymmetric diffuser in turbulent flow," *AIAA Journal*, vol. 42, no. 6, pp. 1154–1169, 2004.

[45] P. Kibicho and A. Sayers, "Performance of a standard $k-\omega$ model in predicting separated diffuser flows," in *Heat Transfer, Fluid Mechanics and Thermodynamics Conference*, (Cape Town, South Africa), 21st-24th June 2004.

[46] T. Ohta, T. Kajishima, and S. Nakagawa, "Direct numerical simulation of turbulent separating flow in an asymmetric plane diffuser," *Turbulence, Heat and Mass Transfer*, vol. 4, 2003.

[47] S. Jungsoo, "Large eddy simulation of turbulent flow in a planar asymmetric diffuser," tech. rep., School of Mechanical Engineering, Purdue University, 2002.

[48] M. Skote and D. Henningson, "Direct numerical simulation of a separated turbulent boundary layer," *Journal of Fluid Mechanics*, vol. 471, pp. 107–136, 2002.

[49] D. Apsley and M. Leschziner, "Advanced turbulence modelling of separated flow in a diffuser," *Flow , Turbulence and Combustion*, vol. 63, pp. 81–112, 2000.

[50] H. Kaltenbach, M. Fatica, R. Mittal, T. Lund, and P. Moin, "Study of flow in a planar asymmetric diffuser using large-eddy simulation," *Journal of Fluid Mechanics*, vol. 390, pp. 151–185, 1999.

[51] H. Kaltenbach, "Towards a near-wall model for LES of a separated diffuser flow," *Annual Research Briefs, Centre for Turbulence Research, Stanford University*, pp. 255–265, 1998.

[52] M. Fatica, H. Kaltenbach, and R. Mittal, "Validation of large-eddy simulation in a plane asymmetric diffuser," *Annual Research Briefs, Centre for Turbulence Research, Stanford University*, pp. 23–33, 1997.

[53] M. Fatica and R. Mittal, "Progress in the large-eddy simulation of an asymmetric plane diffuser," *Annual Research Briefs, Centre for Turbulence Research, Stanford University*, pp. 249–255, 1996.

[54] A. Hellsten and P. Rautaheimo, eds., *8th Ercoftac/Iahr/Cost Workshop*, Helsinki University of Technology, Finland, 1999.

[55] F. Menter, M. Kuntz, and R. Langtry, "Ten years of industrial experience with the SST turbulence model," in *Turbulence, Heat and Mass Transfer 4* (K. Hanjalic, Y. Nagano, and M. Tummers, eds.), Begell House, Inc, 2003.

[56] G. Iaccarino, "Prediction of the turbulent flow in a diffuser with commercial CFD codes," *Annual Research Briefs, Centre for Turbulence Research, Stanford University*, pp. 271–278, 2000.

[57] C. Chen and S. Jaw, *Fundamentals of Turbulence Modeling*. Washington DC, USA: Taylor and Francis, 1998.

[58] D. Wilcox, "Reassessment of the scale-determining equation for advanced turbulence models," *AIAA Journal*, vol. 26, no. 11, pp. 1299–1310, 1988.

[59] F. Menter, "Performance of popular turbulence models for attached and separated adverse pressure gradient flows," *AIAA Journal*, vol. 30, no. 8, pp. 2066–2072, 1992.

[60] P. Huang and P. Bradshaw, "Law of the wall for turbulent flows in pressure gradients," *AIAA Journal*, vol. 33, pp. 624–632, 1995.

[61] F. Menter, "A comparison of some recent eddy-viscosity turbulence models," *Transactions of the ASME, Journal of Fluids Engineering*, vol. 118, no. 3, pp. 514–519, 1996.

[62] C. Yorke and G. Coleman, "Assessment of common turbulence models for an idealized adverse pressure gradient flow," *European Journal of Mechanics B:Fluids*, vol. 23, pp. 319–337, 2004.

[63] J. Kok, "Resolving the dependence on freestream values for the $k-\omega$ turbulence model," *AIAA Journal*, vol. 38, no. 7, pp. 1292–1295, 2000.

[64] F. Menter, "Influence of freestream values on $k-\omega$ turbulence model predictions," *AIAA Journal*, vol. 30, no. 6, pp. 1657 1659, 1992.

[65] F. Menter, "Two-equation eddy-viscosity turbulence models for engineering applications," *AIAA Journal*, vol. 32, no. 8, pp. 1598–1605, 1994.

[66] C. Chambers and D. Wilcox, "Critical examination of two-equation turbulence closure models for boundary layers," *AIAA Journal*, vol. 15, no. 6, pp. 821–828, 1977.

[67] Y. Lai and C. So, "Calculation of planar and conical diffuser flows," *AIAA Journal*, vol. 27, no. 5, pp. 542–548, 1989.

[68] B. Launder and B. Sharma, "Application of the energy dissipation model of turbulence to the calculation of flow near a spinning disc," *Letters in Heat and Mass Transfer*, vol. 1, no. 2, pp. 131–138, 1974.

[69] J. Bredberg, S. Peng, and L. Davidson, "An improved $k-\omega$ turbulence model applied to recirculating flows," *International Journal of Heat and Fluid Flow*, vol. 23, pp. 731–743, 2002.

[70] T. Jeremy, "Stability analysis of the $k-\omega$ turbulence model for channel flow," 2000.

[71] R. Morgans, B. Dally, G. Nathan, P. LansPeary, and D. Fletcher, "Application of the revised Wilcox $k-\omega$ turbulence model to a jet in co-axial flow," in *Minerals and Process Industries Conference*, (Melabourne, Australia), pp. 479–484, CSIRO, 6th-8th December 1999.

[72] W. Rodi and Scheuerer, "Scrutinizing the $k-\epsilon$ turbulence model under adverse pressure gradient conditions," *Transactions of the ASME, Journal of Fluids Engineering*, vol. 108, no. 2, pp. 174–179, 1986.

[73] S. Kline, B. Cantwell, and G. Lilley, eds., *1980-81 AFROSR-HTTM-Stanford Conference on Complex Flows*, vol. III, 1980-81.

[74] A. Samuel and P. Joubert, "A boundary layer development in an increasingly adverse pressure gradient," *Journal of Fluid Mechanics*, vol. 66, pp. 481–505, 1974.

[75] X. Tong, E. Luke, and L. Tang, "Evaluation of the shear-stress transport turbulence model for heat transfer applications," in *41st Aerospace Sciences Meeting and Exhibit*, (Reno, Nevada, USA), 6-9th January 2003.

[76] N. Mohammad and M. Hukam, "Predictions of flows with adverse pressure gradients," in *AIAA/ASME/SAE/ASEE Joint Propulsion Conference and Exhibit*, (Los Angeles, CA, USA), 20-24th June 1999.

[77] M. Rao and H. Hassan, "Modeling turbulence in the presence of adverse pressure gradients," *Journal of Aircraft*, vol. 35, no. 3, pp. 500–502, 1998.

[78] S. Peng, L. Davidson, and S. Holmberg, "A modified low-Reynolds-number $k-\omega$ model for recirculating flows," *Transactions of the ASME, Journal of Fluids Engineering*, vol. 119, no. 4, pp. 867–875, 1997.

[79] D. Wilcox, "Comparison of two-equation turbulence models for boundary layers with pressure gradient," *AIAA Journal*, vol. 31, no. 8, pp. 1414–1421, 1993.

[80] B. Baldwin and H. Lomax, "Thin layer approximation and algebraic model for separated flows," *AIAA Paper 78-257*, 1978.

[81] D. Johnson and L. King, "Mathematically simple turbulence closure models for attached and separated turbulent boundary layers," *AIAA Journal*, vol. 23, no. 11, pp. 1684–1692, 1985.

[82] B. Baldwin and T. Barth, "A one equation turbulence transport model for high reynolds number wall-bounded flows," Tech. Rep. TM-102847, NASA, 1990.

[83] P. Spalart and P. Allmaras, "A one-equation turbulence model for aerodynamic flows.," Tech. Rep. AIAA-92-0439, American Insititute of Aeronautics and Astronautics, 1992.

[84] J. Hinze, *Turbulence*. New York, NY: McGraw-Hill, 2nd ed., 1975.

[85] H. Tennekes and J. Lumley, *A First Course in Turbulence*. Massachusetts, USA: MIT Press, 1972.

[86] H. Schlichting and K. Gersten, *Boundary Layer Theory*. Berlin, Germany: Springer-Verlag, 8 ed., 2003.

[87] D. Wilcox, *Turbulence Modelling for CFD*. La Canada, California, USA: DCW Industries, 2 ed., 2004.

[88] F. Lien and M. Leschziner, "Assessment of turbulent transport models including non-linear RNG eddy viscosity formulation and second moment closure," *Computers and Fluids*, vol. 23, no. 8, pp. 983 1004, 1994.

[89] M. Gibson and B. Launder, "Ground effects on pressure fluctuation in the atmospheric boundary layer," *Journal of Fluid Mechanics*, vol. 86, pp. 491–511, 1978.

[90] S. Fu, B. Launder, and M. Leschziner, "Modeling strongly swirling recirculating jet flow with Reynolds-stress transport closure," in *Sixth Symposium on Turbulent Shear Flows,*, (Toulouse, France), 1987.

[91] B. Launder, "Second moment closure:present...and future?," *International Journal of Heat and Fluid Flow*, vol. 10, no. 4, pp. 282–300, 1989.

[92] B. Launder, "Second moment closure and its use in modelling turbulent industrial flows," *International Journal for Numerical Methods in Fluids*, vol. 9, pp. 963 985, 1989.

[93] K. Hanjalic and B. Launder, "A Reynolds stress model of turbulence and its application to thin shear," *Journal of Fluid Mechanics*, vol. 52, no. 4, pp. 609–638, 1972.

[94] B. Launder, G. Reece, and W. Rodi, "Progress in the development of a Reynolds-stress turbulence closure," *Journal of Fluid Mechanics*, vol. 68, no. 3, pp. 537–566, 1975.

[95] B. Launder and D. Spalding, *Lectures in Mathematical Models of Turbulence*. London, England: Academic Press, 1972.

[96] M. Fogiel, *Handbook of Mathematical, Scientific, and Engineering Formulas, Tables, Fuctions, Graphs, Transforms*. New Jersey, USA: Research and Education Association, 2001.

[97] W. Reynolds, "Fundamentals of turbulence modeling and simulation," Tech. Rep. 755, Lecture Notes for Von Karman Institute, Agard Report, 1987.

[98] T. Shih, W. Liou, A. Shabbir, Z. Yang, and J. Zhu, "A new $k-\epsilon$ eddy viscosity model for high Reynolds number turbulent flows," *Computers and Fluids*, vol. 24, no. 3, pp. 227–238, 1995.

[99] D. Wilcox, "Simulation of transition with a two-equation turbulence model," *AIAA Journal*, vol. 32, no. 2, pp. 247–255, 1994.

[100] D. Driver, "Reynolds shear stress measurements in a separated boundary layer," *AIAA Paper*, vol. 91-1787, 1991.

[101] M. Wolfshtein, "The velocity and temperature distribution in one-dimensional flow with turbulence augmentation and pressure gradient," *International Journal of Heat and Mass Transfer*, vol. 12, pp. 301–318, 1969.

[102] H. Chen and V. Patel, "Near-wall turbulence models for complex flows including separation," *AIAA Journal*, vol. 26, no. 6, pp. 641–648, 1988.

[103] K. Yajnik and R. Gupta, "A new probe for measurement of velocity and flow direction in separated flows," *Journal of Physics, Series E, Science Instrumentation*, vol. 6, no. 82-86, 1973.

[104] D. Bryer and R. Pankhurst, "Pressure probe methods for determining wind speed and flow direction," tech. rep.. HMSO, 1971.

[105] A. Rhagava, K. Kumar, R. Malhotra, and D. Agrawal, "A probe for the measurement of velocity field," *Transactions of the ASME, Journal of Fluids Engineering*, vol. 11, no. 1, pp. 143–146, 1979.

[106] G. Morrison, M. Schobeiri, and K. Pappu, "Five-hole pressure probe analysis technique," *Flow Measurement and Instrumentation*, vol. 9, pp. 153–158, 1998.

[107] M. Gundogdu and M. Carpinlioglu, "A multi-tube pressure probe calibration method for measurements of mean flow parameters in swirling flows," *Flow Measurement and Instrumentation*, vol. 9, pp. 243–248, 1998.

[108] A. Pisasale and N. Ahmed, "A novel method for extending the calibration range of a five-hole probe for highly three-dimensional flows," *Flow Measurement and Instrumentation*, vol. 13, pp. 23–30, 2002.

[109] H. Versteeg and W. Malasekera, *An Introduction to Computational Fluid Dynamics*. Malaysia: Prentice Hall Inc, 1995.

[110] J. Anderson, *Computational Fluid Dynamics*. New York, USA: McGraw Hill, Inc, 1995.

[111] *Fluent 6.1 User's Guide*. Lebanon, NH, 2003.

[112] *Gambit 2 Modeling Guide*. Lebanon, NH, 2001.

[113] S. Kline and McClintock, "Describing uncertainties in single-sample experiments," *Mechanical Engineering*, vol. 75, no. 1, pp. 3–8, 1953.

[114] J. Holman, *Experimental Methods for Engineers*, ch. 2, pp. 41–51. USA: McGraw-Hill, Inc., 1978.

[115] R. Taylor, *An Introduction to Error Analysis.* Sausalito, California, USA: University Science Books, 2 ed., 1982.

[116] H. Coleman and F. Stern, "Uncertainties and CFD code validation," *Transactions of the ASME, Journal of Fluids Engineering*, vol. 119, no. 4, pp. 795 803, 1997.

[117] P. Ligrani, B. Singer, and L. Baun, "Miniature five-hole pressure probe for measurement of three mean velocity components in low-speed flows," *Journal of Physics, Series E, Science Instrumentation*, vol. 22, pp. 868–876, 1989.

Appendices

Appendix A

Data bank contribution

A.1 Wall C_p distribution on both walls

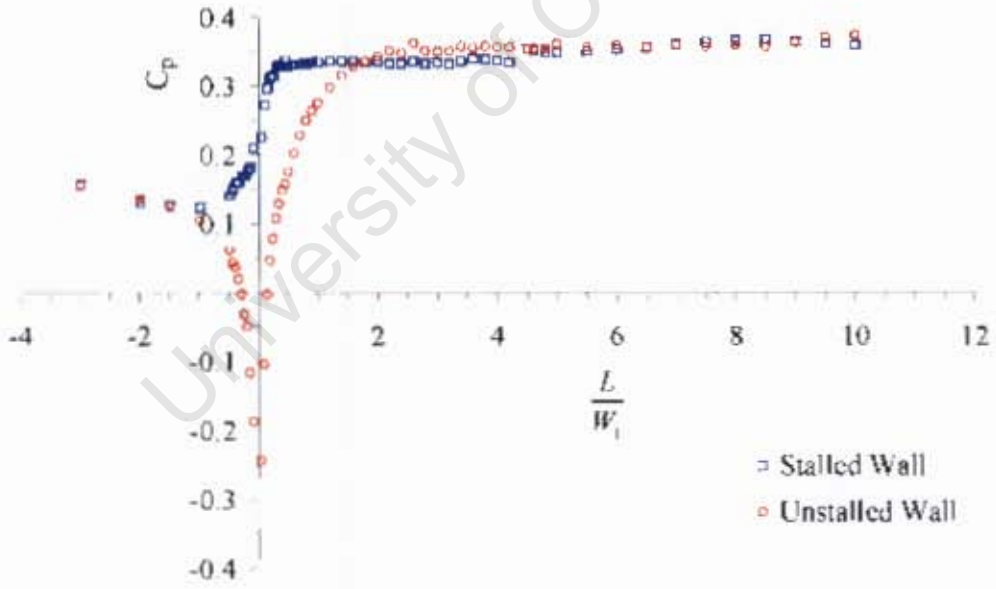

Figure A.1: Coefficient of static pressure for the 30° diffuser

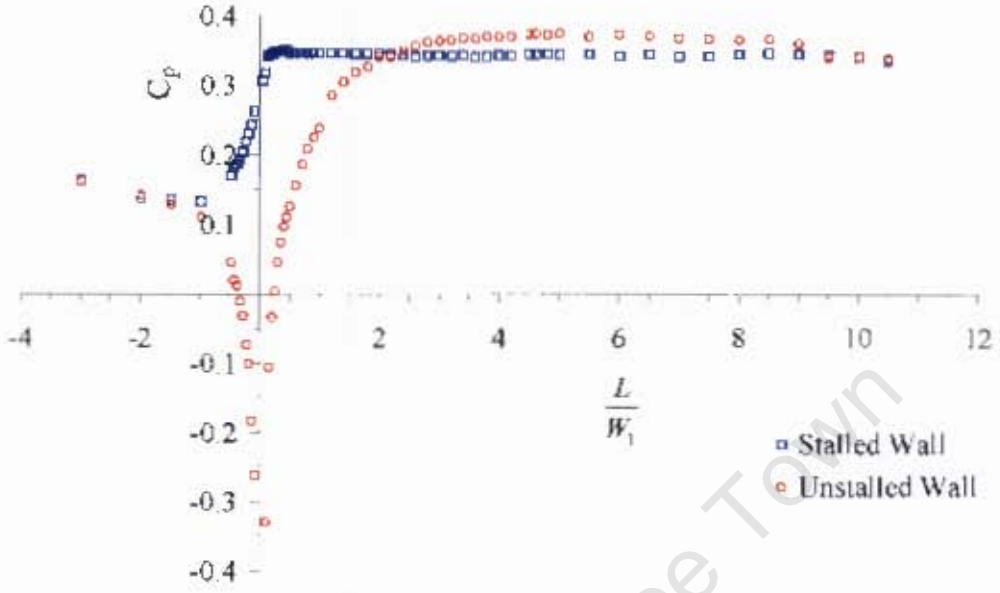

Figure A.2: Coefficient of static pressure for the 40° diffuser

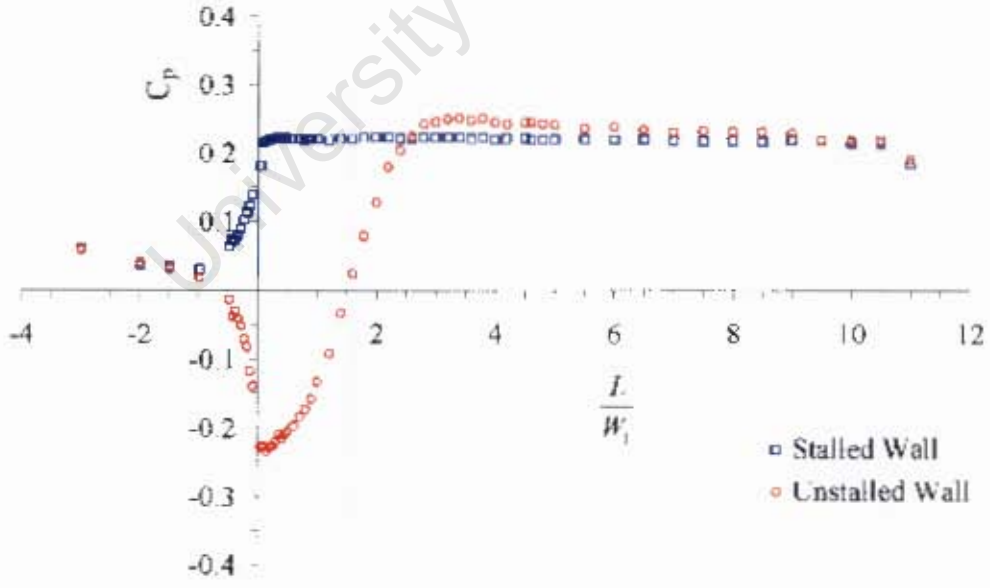

Figure A.3: Coefficient of static pressure for the 50° diffuser

A.2 C_p distribution on unstalled wall

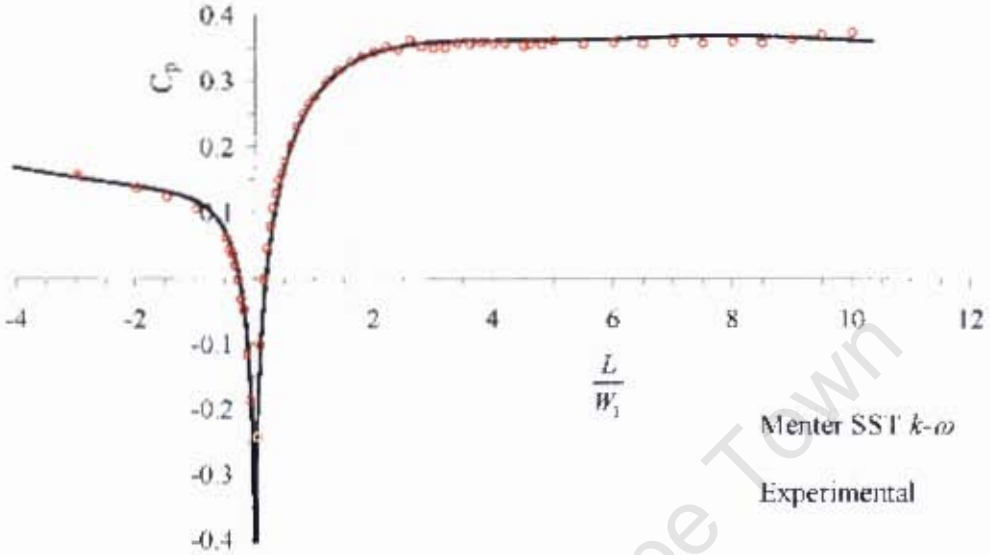

Figure A.4: Experimental and numerical C_p data for the 30° diffuser

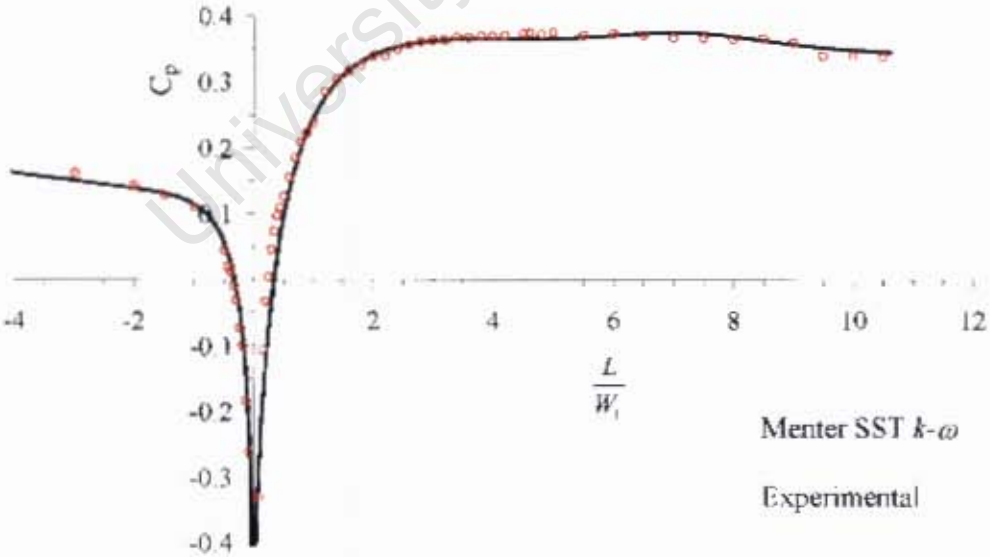

Figure A.5: Experimental and numerical C_p data for the 40° diffuser

A.3 Axial velocity profiles

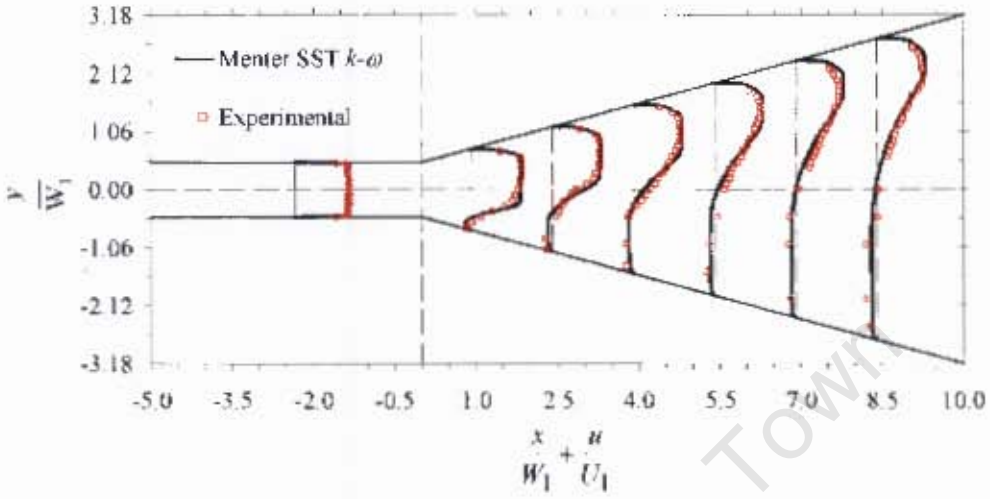

Figure A.6: Axial velocity profiles for the 30° diffuser

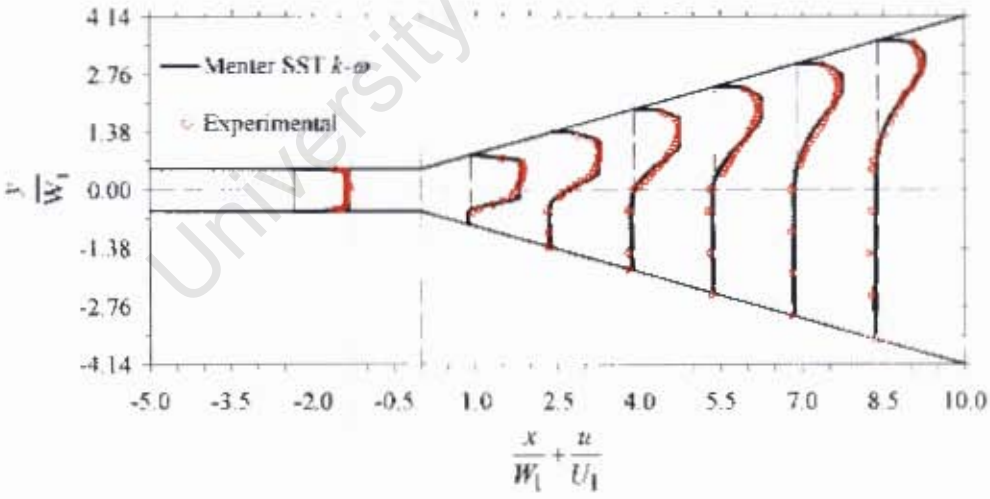

Figure A.7: Axial velocity profiles for the 40° diffuser

A.4 Lateral velocity profiles

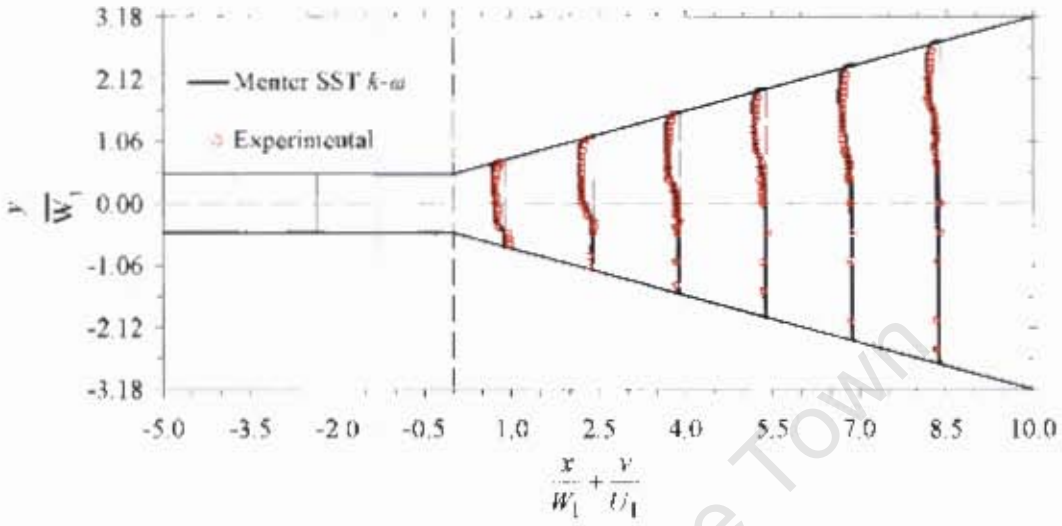

Figure A.8: Lateral velocity profiles for the 30° diffuser

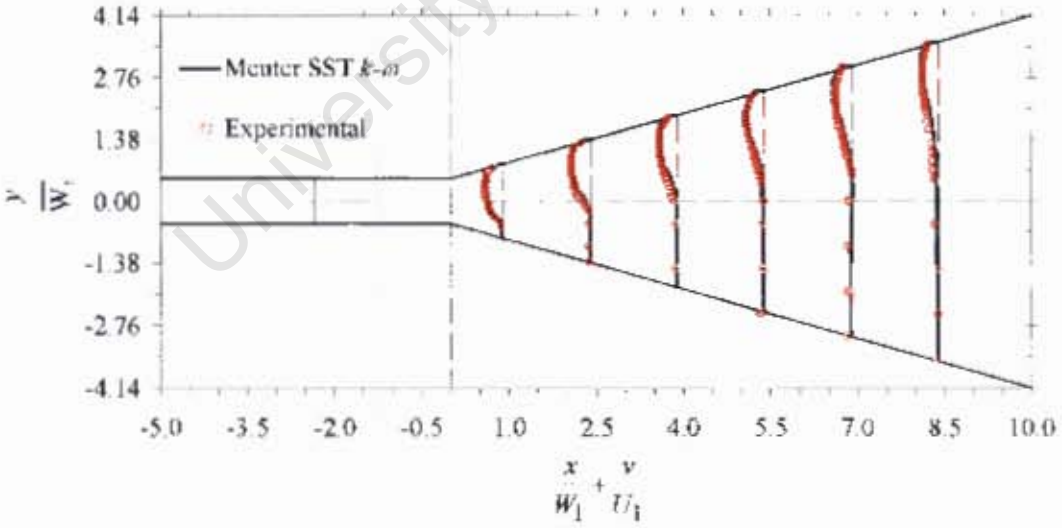

Figure A.9: Lateral velocity profiles for the 40° diffuser

A.5 Static pressure profiles

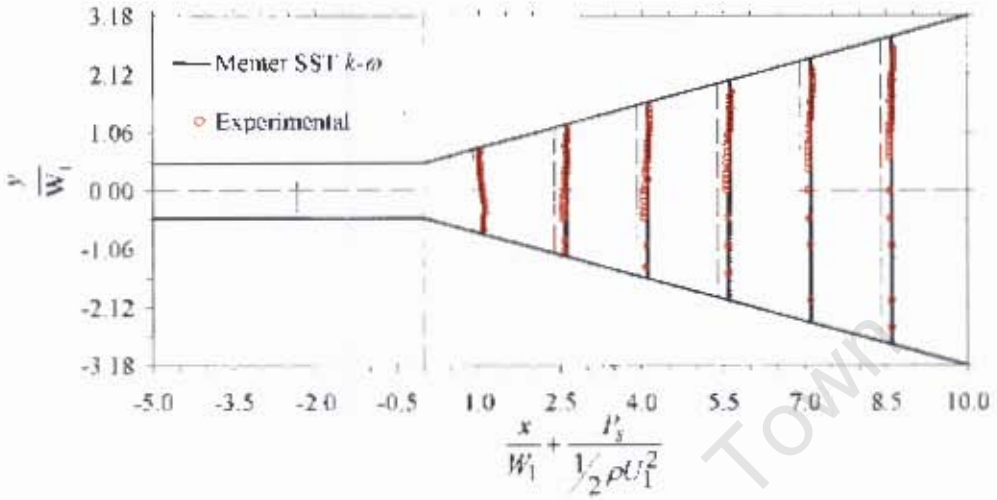

Figure A.10: Static pressure coefficient profiles for the 30° diffuser

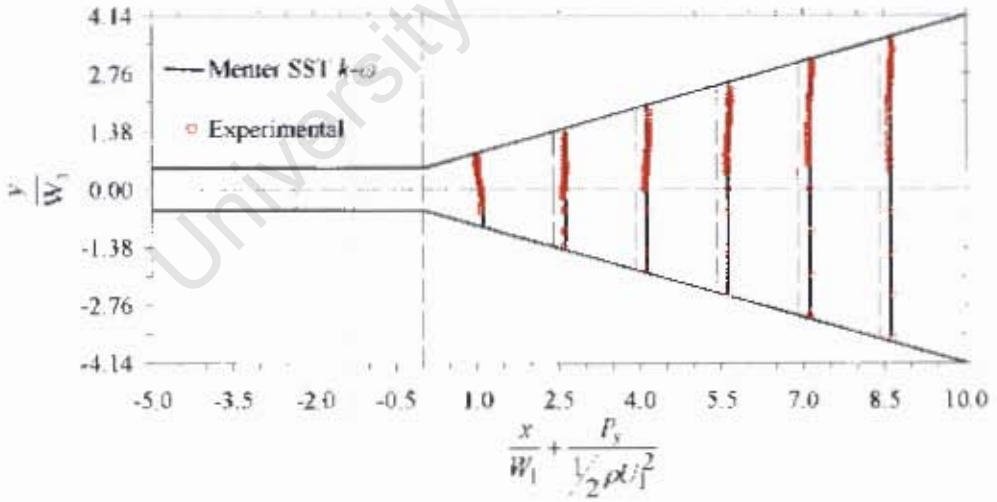

Figure A.11: Static pressure coefficient profiles for the 40° diffuser

A.6 Velocity profiles on the normalized scale

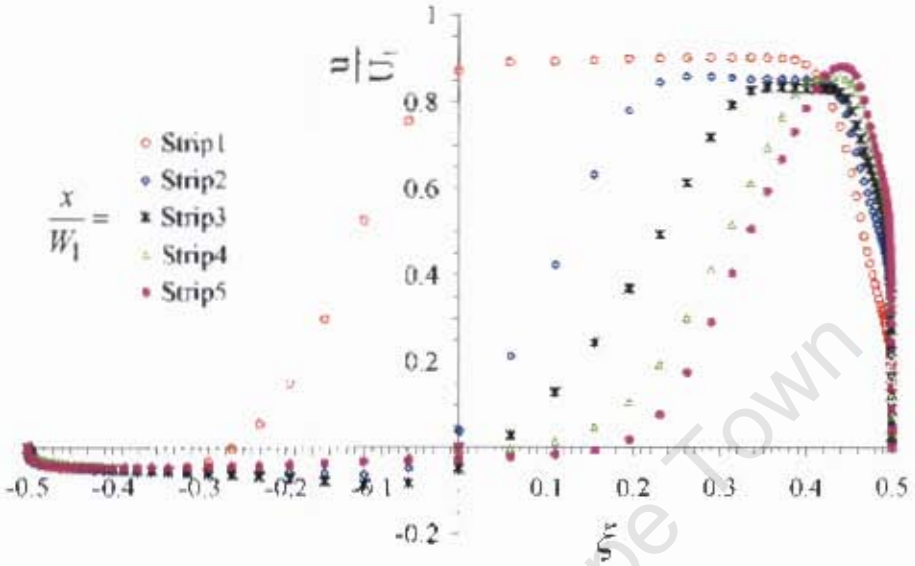

Figure A.12: Normalized velocity profiles for the 42° diffuser

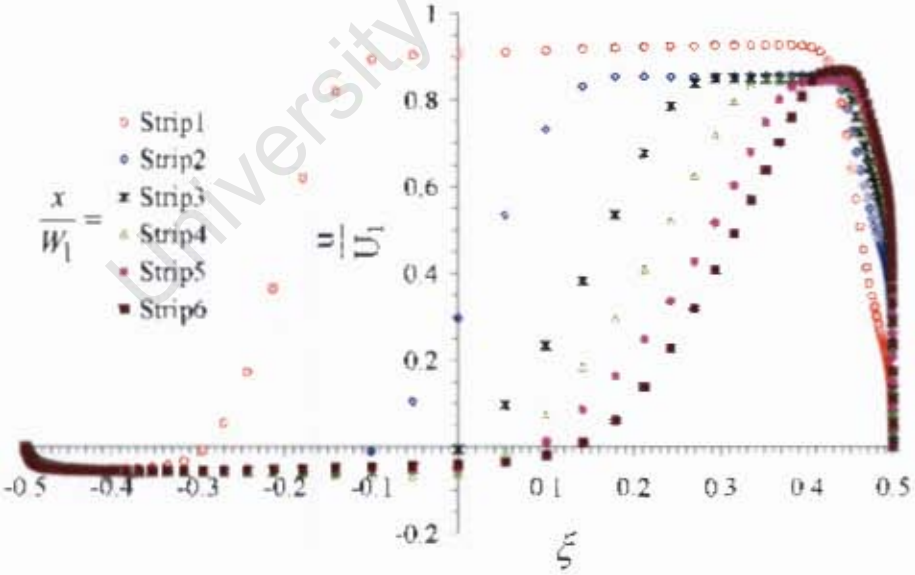

Figure A.13: Normalized velocity profiles for the 40° diffuser

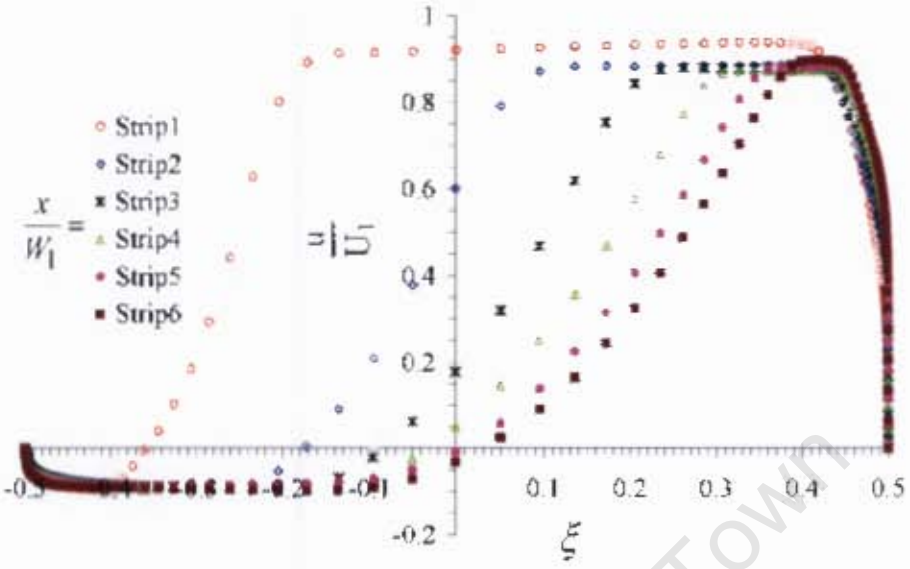

Figure A.14: Normalized velocity profiles for the 30° diffuser

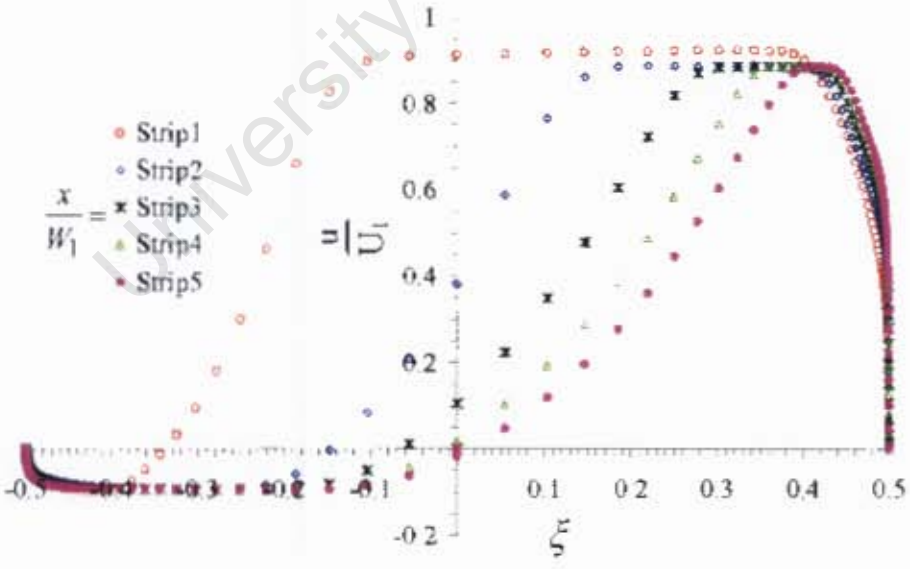

Figure A.15: Normalized velocity profiles for the 28° diffuser

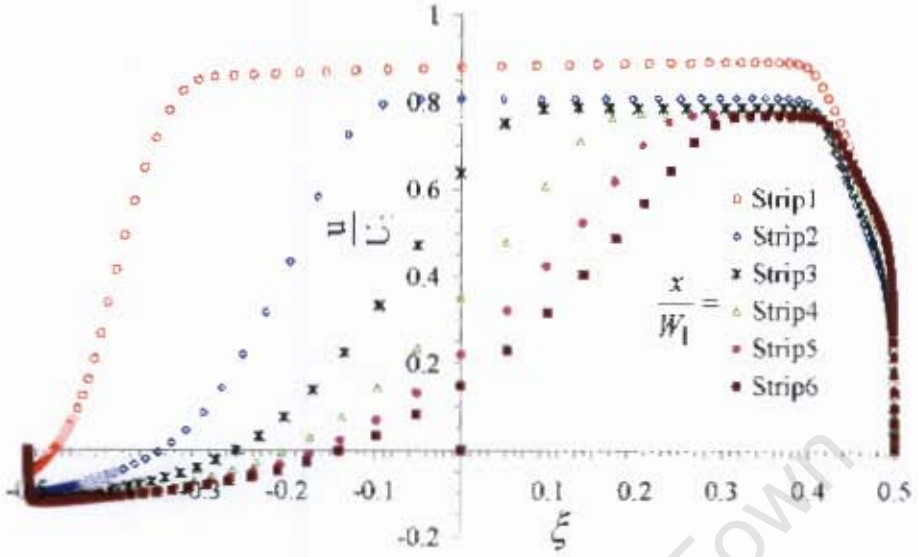

Figure A.16: Normalized velocity profiles for the 20° diffuser

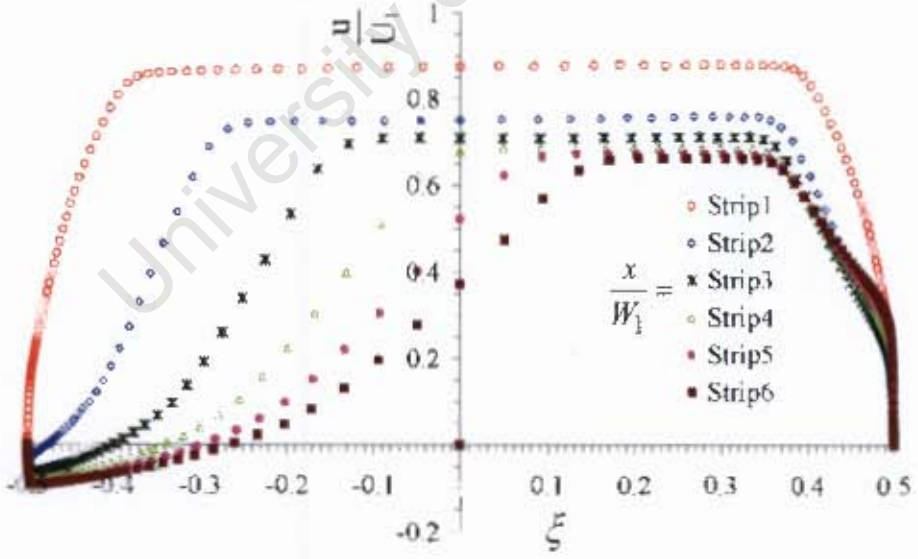

Figure A.17: Normalized velocity profiles for the 15° diffuser

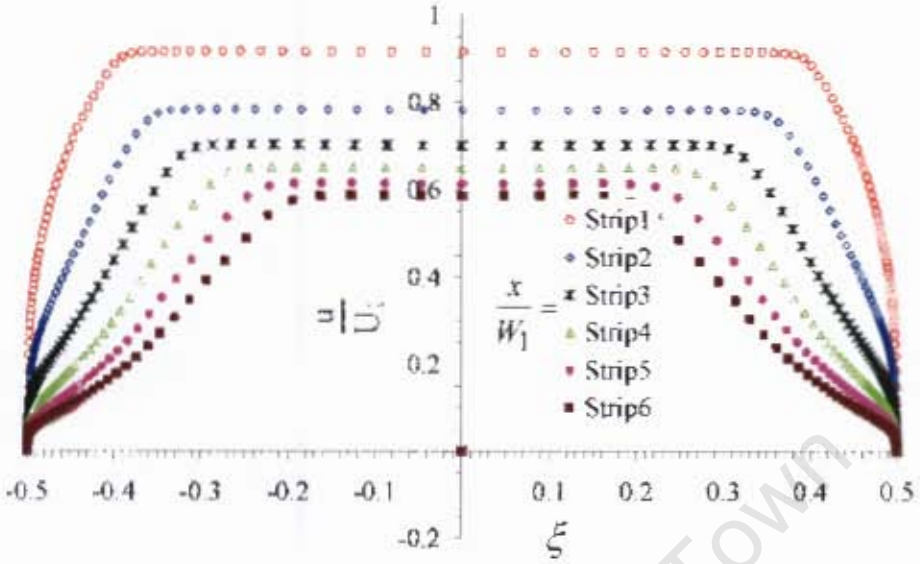

Figure A.18: Normalized velocity profiles for the 10° diffuser

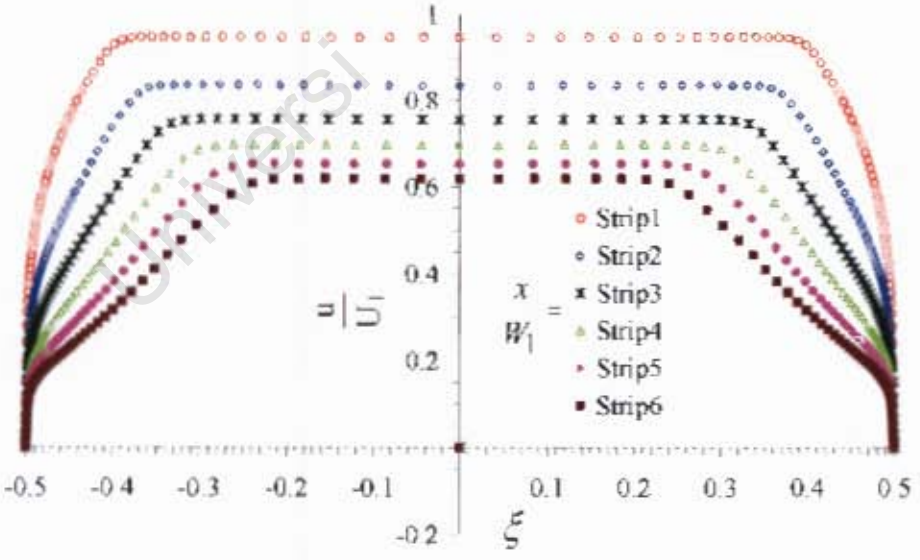

Figure A.19: Normalized velocity profiles for the 7° diffuser

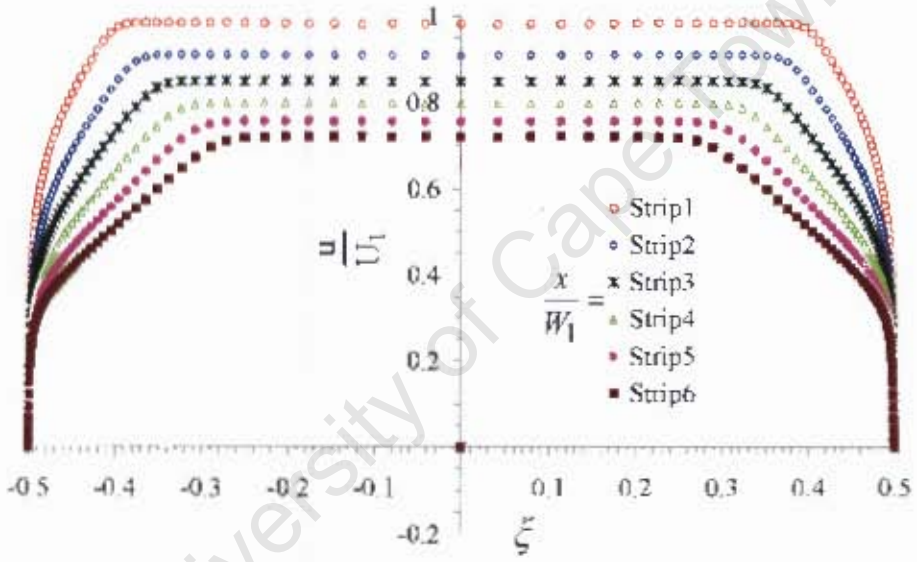

Figure A.20: Normalized velocity profiles for the 4° diffuser

A.7 Skin friction coefficient, C_{fx}

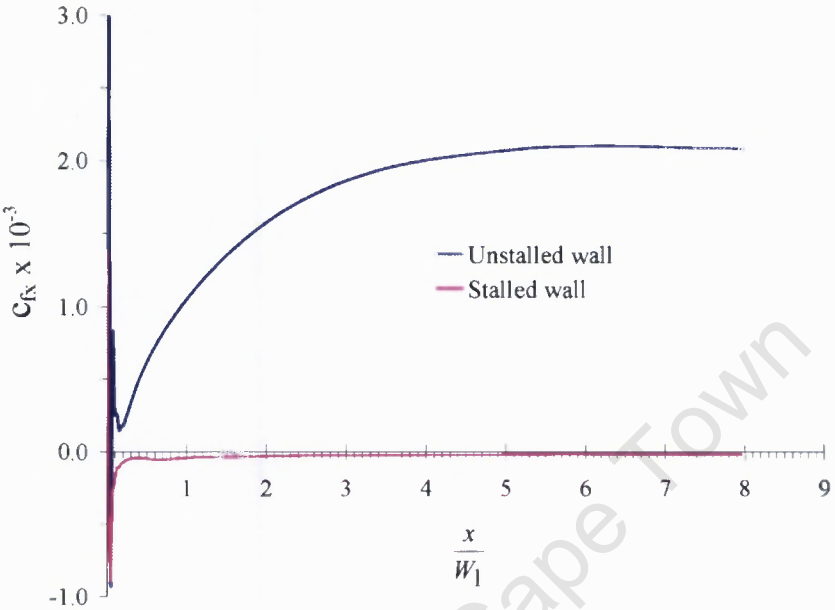

Figure A.21: Skin friction coefficient C_{fx} for the 42° diffuser

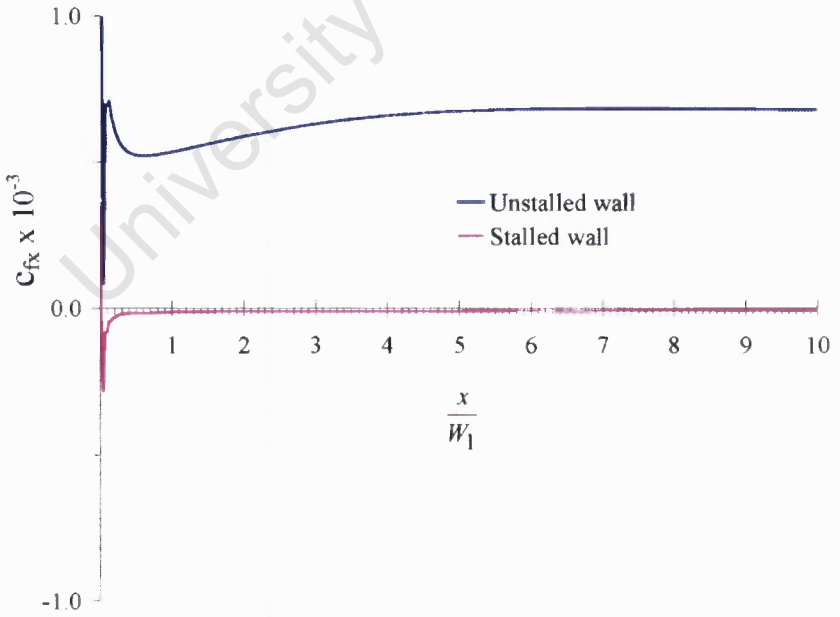

Figure A.22: Skin friction coefficient C_{fx} for the 40° diffuser

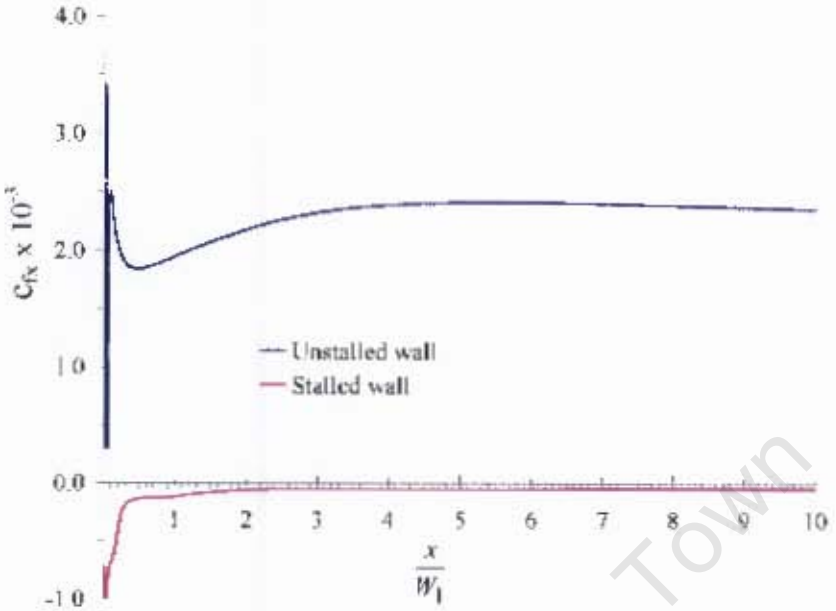

Figure A.23: Skin friction coefficient C_{fx} for the 30° diffuser

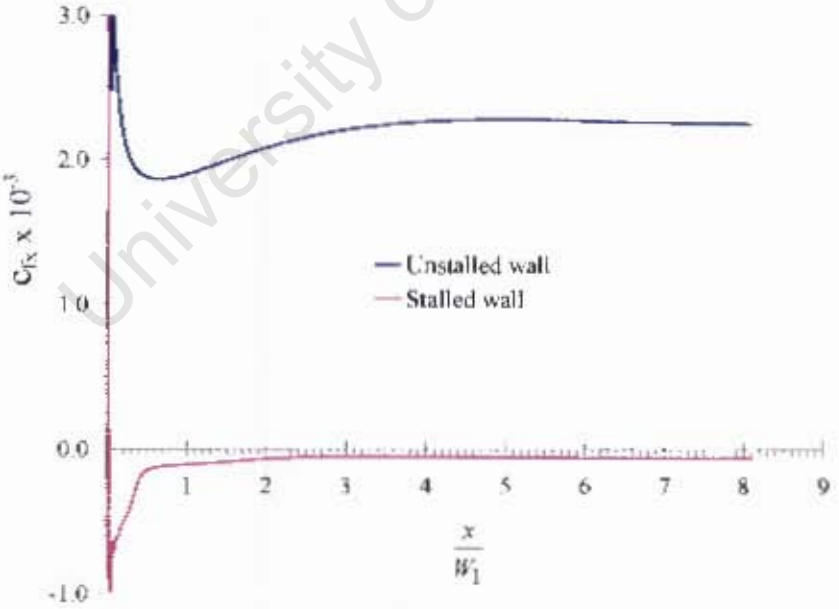

Figure A.24: Skin friction coefficient C_{fx} for the 28° diffuser

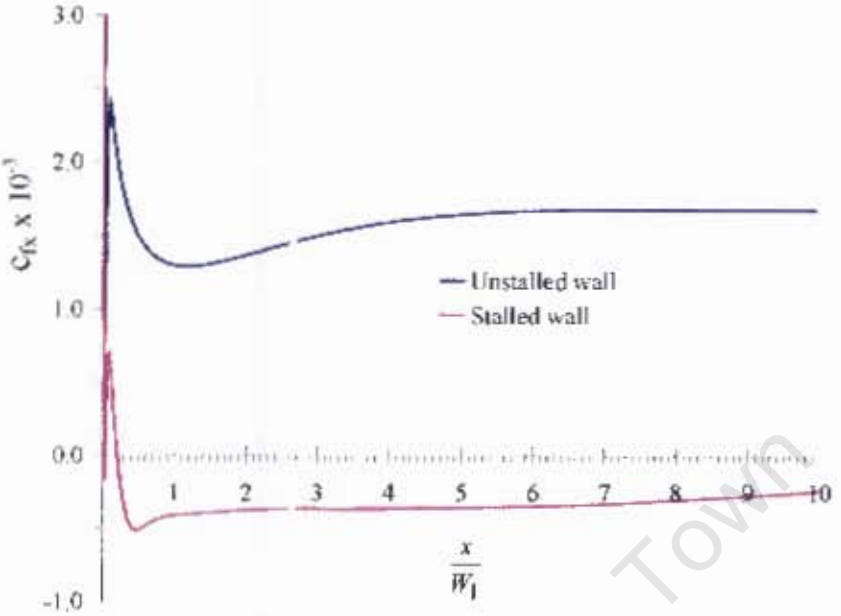

Figure A.25: Skin friction coefficient C_{fx} for the 20° diffuser

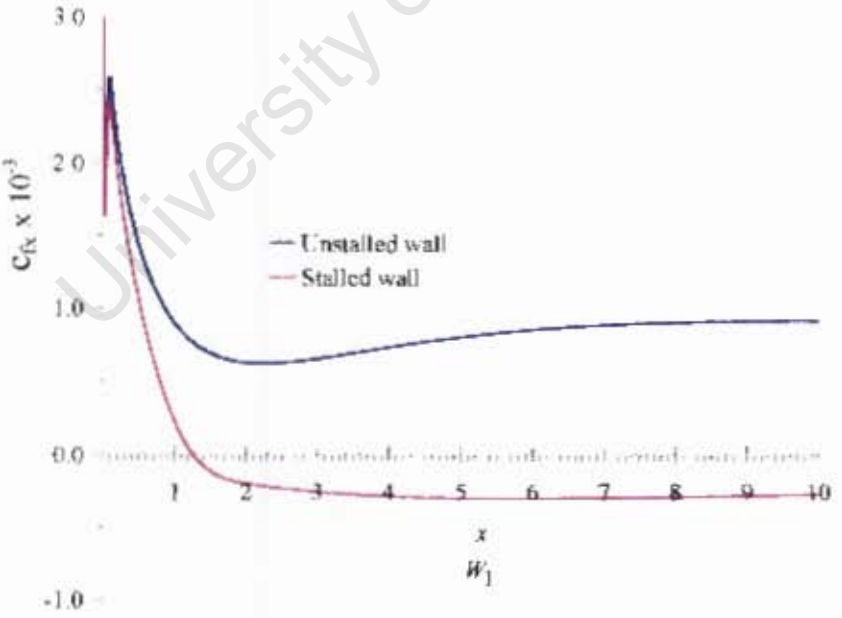

Figure A.26: Skin friction coefficient C_{fx} for the 15° diffuser

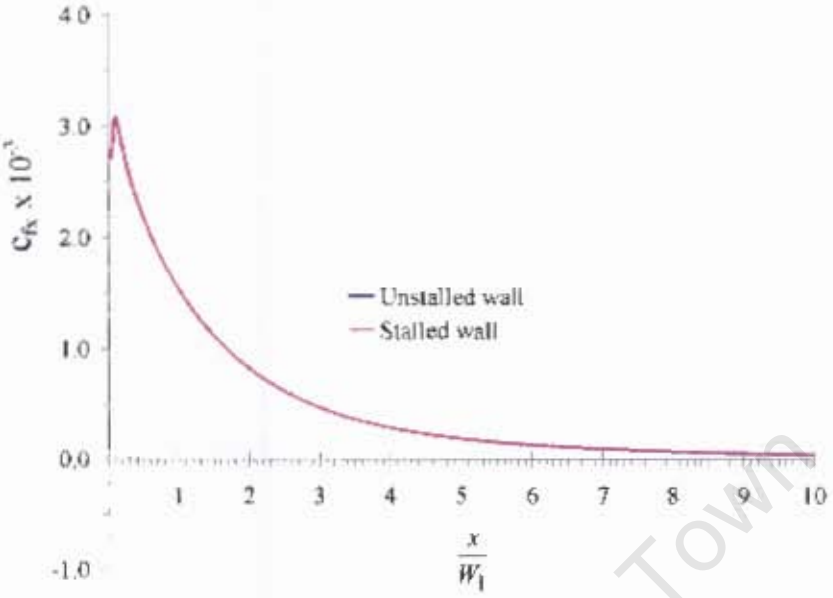

Figure A.27: Skin friction coefficient C_{fx} for the 10° diffuser

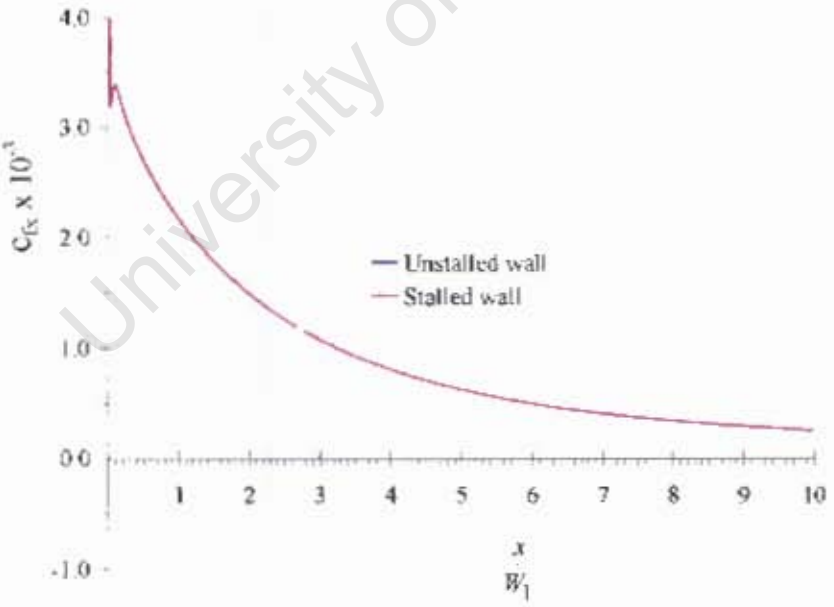

Figure A.28: Skin friction coefficient C_{fx} for the 7° diffuser

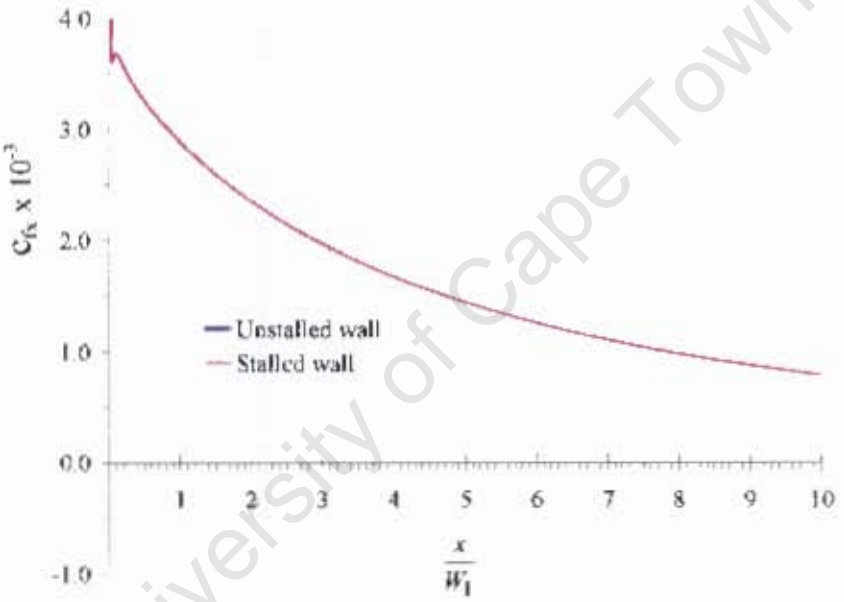

Figure A.29: Skin friction coefficient C_{fx} for the 4° diffuser

Appendix B

Calibration of instruments and data acquisition

B.1 Pressure Transducer

All the pressures were measured by use of an ultra low differential pressure transducer, model DP850V2P5 from Validyne Engineering. To allow for measurements of ultra low pressures, the Validyne transducer uses the variable reluctance method of transduction in its design. With this method over amplification of the sensor signals is not needed, hence contributing greatly to system stability and accuracy. The pressure-sensing element is a stainless steel diaphragm clamped between case halves of the same material in a symmetrical assembly. Pick-off coils embedded in the case halves sensed deflection of the diaphragm in response to applied pressure. Self-contained electronics provided excitation to the pick-off coils and translated diaphragm movement into a 0-5 Vdc output for convenient use.

The transducer's pressure range was 0-2.5 inches of water equivalent to a full range pressure of 623 Pa. The transducer had barbed fittings for 1/4 inch internal diameter hose for the pressure connections. The maximum absolute error of the data acquisition card used to digitize the transducer voltage

signals was 2mV. This corresponded to ±0.25 Pa. Within the uncertainty of the A/D conversion, the resolution of the transducer was ±0.25 Pa. The accuracy of the transducer was specified as ±1.5% full scale (best fit straight line), which included non-linearity, hysteresis and non-repeatability.

Calibration was carried out using a Pitot-static tube with Tee junctions at both the static and total tube connections. Each Tee junction was connected to an inclined alcohol manometer at one outlet and to the transducer at the other. The Pitot-static tube was placed in a low turbulence intensity (0.4%) wind tunnel with variable air velocity. For a given wind speed, the transducer output voltage was read and the corresponding pressure based on the manufacturer's best-fit curve computed. The computations were based on Eqs.B.1 and B.2. The linearity of the manometer reading was found to be within ±1.1% of the manufacturer's specification.

$$P_{\text{tra}} = \frac{(2.5 \times 0.0254 \times \rho_{\text{wat}} \times g) \times V_{\text{tran}}}{5} \tag{B.1}$$

$$P_{\text{man}} = \rho_{\text{man}} \times g \times l \sin\theta \tag{B.2}$$

where P_{tra} and P_{man} were the transducer and manometer differential pressures respectively, ρ_{wat} and ρ_{man} were the water and manometric fluid densities respectively, θ was the inclination of the alcohol manometer and V_{tra} was the transducer voltage. The manometer was inclined at 30°. The specific gravity of the manometric fluid (ethanol) was 0.82. Since the resolution of the manometer scale was 0.5 mm, the maximum possible error expected from human reading errors were within ±0.25 mm. Figure B.1 shows the calibration curve for the transducer.

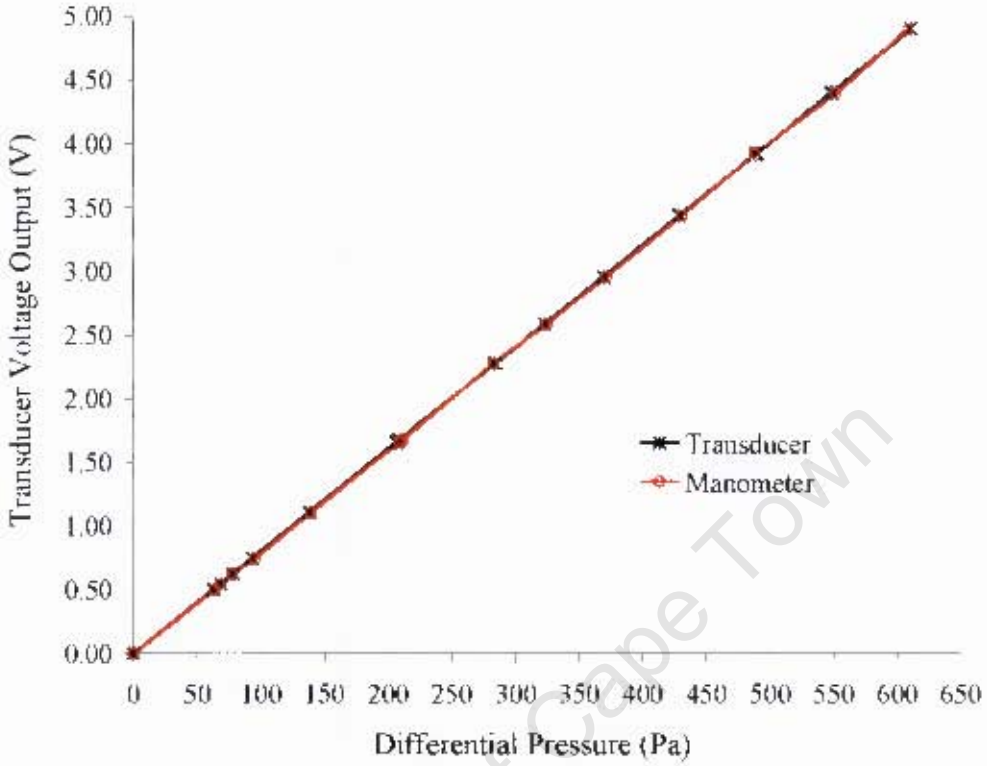

Figure B.1: Pressure transducer calibration curve

B.2 Scanivalve

A pressure sampling scanner model 48J9 Scanivalve from Scanivalve Co-operation was used for measuring multiple pressures in conjunction with the DP850V2P5 transducer. It was designed to use one integral pressure transducer with its zeroing circuit to do the work of 48 transducers and 48 circuits. The transducer was sequentially connected to the various pressure ports via a radial hole in the rotor that terminated at the collector hole. As the rotor rotated, this collector hole passed under the pressure ports in the stator. Each pressure port was ducted from the block to its port in the stator. The rotor was driven by a solenoid, which was controlled by a CTRL2 solenoid controller with a step and home function. The solenoid controller

had an automatic stepping function with speed adjustment. The position of the rotor was tracked using an optical emitter transmitting to an odd/even decoder. The odd/even decoder was a flip-flop counter whose output was an 8-bit BINY number displayed on a screen and a binary digital number that was read through a computer. The sampling rates were user defined allowing a maximum of 200 Hz.

The Scanivalve was tested for internal leakage at manufacture by pumping and sealing each tubulation at 24 inches of mercury (82.5kPa) with a total included volume of 5 cubic centimeters. The acceptable leakage level was a drop of 5 inches (17.2kPa) per hour. This was equivalent to a drop of 20.8% per hour. External leakages at the vinyl tube connections on the Scanivalve pneumatic connector output were checked by use of a DPI 1610 Portable Precision Pneumatic calibrator. From the calibrator, a pressure of 0.5 bar was applied for 10 minutes to each port and the pressure drop over time noted. The maximum pressure drop corresponded to 11.4% drop per hour. This was within the acceptable range. Furthermore, the actual experiments were conducted at pressures well below 0.1 bar. Leakages were further checked using soapy water around the vinyl connections and checking for the formation of any bubbles. No leakages were observed.

B.3 Yaw meter steady state calibration

The calibration of the yaw meter probe was conducted in a low turbulence intensity wind tunnel. It was based on the pressure measurements sensed by the three tubes of the probes over a matrix of yaw angles, which exceeded the flow angles expected in the flow-field to be measured. It was rotated to cover yaw angles ψ, within the range of $-120° < \psi < 120°$ in increments of 2°. The reference probe null direction was selected as the direction of

the centreline of the probe tip in line with the main flow direction when the pressures recorded from the off-center tubes were equal to each other. At this reference direction, $\psi = 0°$. The pressure measured at the central tube of the probe in this reference position was the total (stagnation) pressure of the flow, P_t.

The dynamic pressure in this position was measured by taking the differential pressure between the total pressure and static pressure from a static pressure tapping on the sidewall of the tunnel. The pressures sensed from the tubes of the probe were recorded separately for each yaw angle setting of the probe with respect to the reference position, and the non-dimensional calibration parameters calculated in terms of pressures and resultant flow velocity q similar to the ones specified by Yajnik and Gupta [103], Bryer and Pankhurst [104] and Rhagava,et al. [105] and given in Eqs.B.3 to B.5.

$$f(\psi) = \frac{P_l - P_r}{P_c - P_m} \tag{B.3}$$

$$Q_p = \frac{P_c - P_m}{\rho q^2/2} \tag{B.4}$$

$$S_p = \frac{P_t - P_c}{P_c - P_m} \tag{B.5}$$

where P_l and P_r are the pressures sensed by the off-center tubes, $P_m = (P_l + P_r)/2$, is the mean pressure for the off-center pressures, P_c is the pressure measured by the central tube, and P_t is the local total pressure that would be measured by the probe if it were at null-position.

Morrison et al. [106], Gundogdu and Carpinlioglu [107], and Pisasale and Ahmed [108] have shown that these functions can be established by direct calibration at one Reynolds number then applied to a range of Reynolds

numbers. Calibration of the probe used in this study was done at 15 m/s. When large angles of yaw are sought, the yaw calibration parameter, $f(\psi)$, in this technique tends to produce a singularity when the sign in the denominator changes, meaning that at one point, the value of the denominator is zero and a discontinuity in $f(\psi)$ is obtained as can be seen in figure B.2 in the neighborhood of $\pm 50°$.

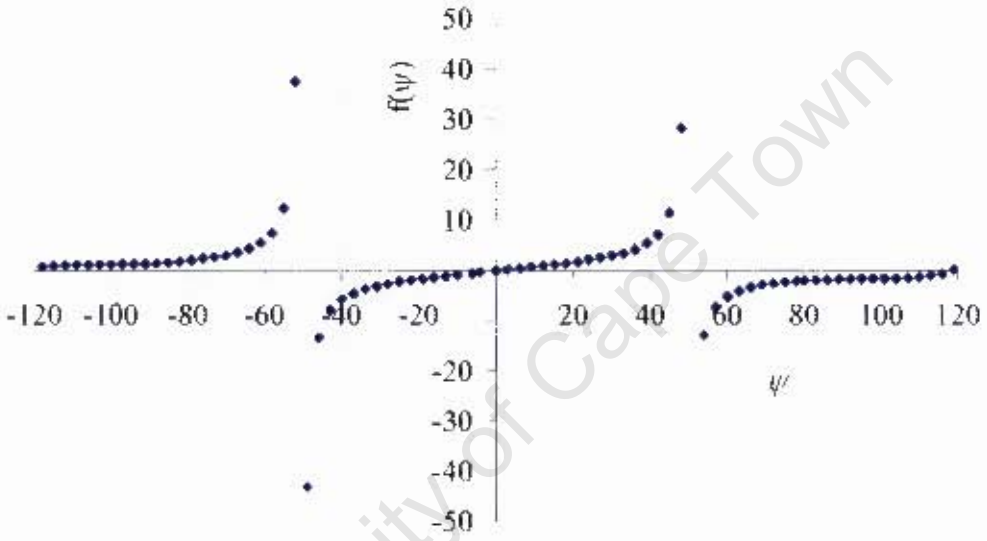

Figure B.2: Yaw angle calibration parameter $f(\psi)$ for $-120° \leq \psi \leq 120°$

In this regard, during measurements, it was ensured that the denominator $P_c - P_m$ always remained positive. This requirement meant that while determining the resultant velocity q, based on the dynamic pressure calibration parameter S_P, the square root of a negative value was never encountered. As can be observed from figure B.2, the pattern seemed to repeat itself after every 90° and hence the chart was truncated to cover $-45° < \psi < 45°$. This observation was also reported by Bryer and Pankhurst [104], and Ligrani et al. [117].

For the large number of measurement points, the chart reading method of the calibration parameters proved to be very tedious. Consequently, the

linear portions of the calibration charts were defined and polynomial descriptions of these portions developed to make the analysis easier through a computer program. Inspection of the $f(\psi)$ versus ψ chart, figure B.3, shows that the linear portion of the curve was between $-1.4 < f(\psi) < 1.26$ which corresponded to $-16° < \psi < 14°$ and is described by Eq.B.6.

$$f(\psi) = 0.0295 + 0.0896\psi \tag{B.6}$$

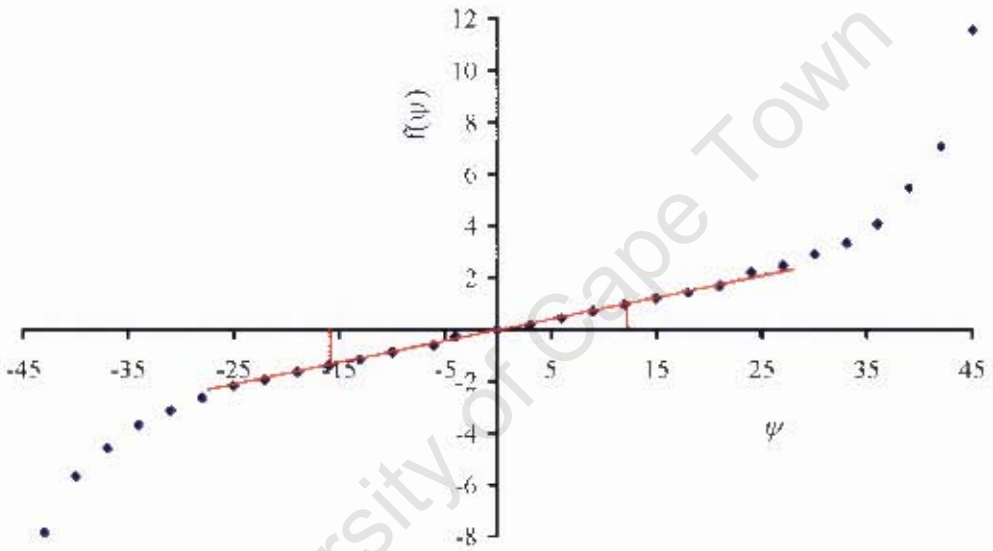

Figure B.3: Yaw angle calibration parameter $f(\psi)$ for $-45° \leq \psi \leq 45°$

Within this region, the dynamic pressure Q_p, and total pressure, S_p, calibration parameters both produce a one-on-one relationship with ψ as can be seen from both figures B.4 and B.5. Both Q_P and S_P within this region were curve fitted using sixth order polynomials given in Eq.B.7.

$$\begin{aligned} Q_P \quad & 0.6544 + (26\psi - \psi^2)\text{x}10^{-4} - (3\psi^3 - \psi^4)\text{x}10^{-6} \\ & - (7\psi^5 + 3\psi^6)\text{x}10^{-9} \\ S_P \quad & -0.0079 - (5\psi - 3\psi^2)\text{x}10^{-4} - (\psi^3 + 5\psi^4)\text{x}10^{-6} \\ & + (20\psi^5 + 4\psi^6)\text{x}10^{-9} \end{aligned} \tag{B.7}$$

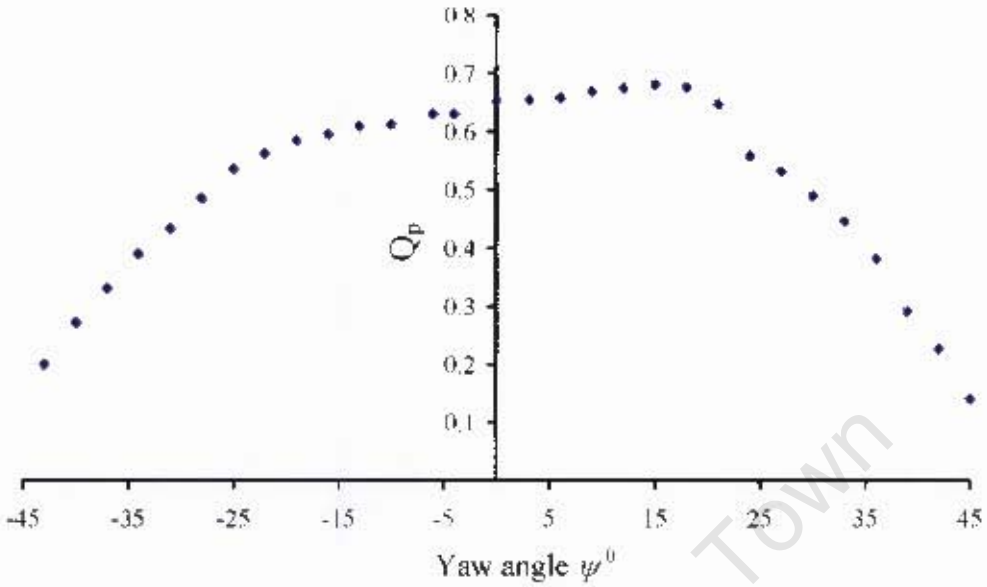

Figure B.4: Yaw angle calibration parameter $f(\psi)$ for $-45° \leq \psi \leq 45°$

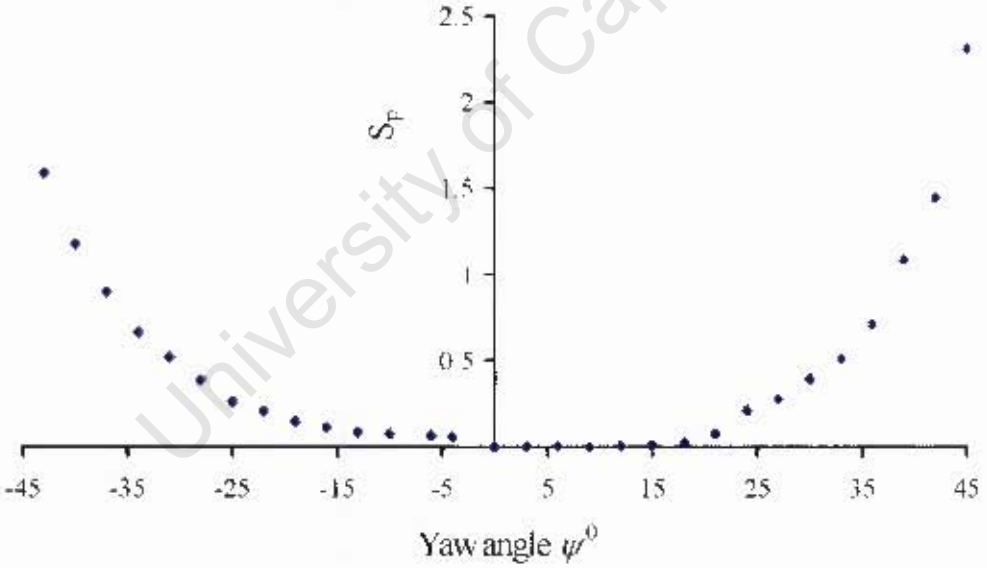

Figure B.5: Yaw angle calibration parameter $f(\psi)$ for $-45° \leq \psi \leq 45°$

To ensure that $P_c - P_m$ remained positive, and $-1.4 < f(\psi) < 1.26$, the values of $f(\psi)$ and $P_c - P_m$ were monitored in real time through the data acquisition software. Whenever the two conditions were not met, the probe

was rotated to a better, but known reference orientation that was read off the protractor. The flow direction and velocity were then established relative to the adjusted probe orientation. Finally, the flow direction was transformed so that it was referenced to the geometric null-probe direction.

At a given probe location, the pressures from the three tubes were read and $f(\psi)$ calculated according to Eq.B.3. With $f(\psi)$ known, the flow yaw angle ψ, was calculated from Eq.B.6. Finally, from the curve fitting polynomials, Q_P and S_P were established from the calculated value of ψ. Since P_c and $P_c - P_m$ at this location are known, the local magnitudes of the resultant velocity q and total pressure P_t, were evaluated from Eqs.B.4 and B.5, respectively. Further, the local static pressures were established by subtracting the dynamic pressure $\frac{1}{2}\rho q^2$, from the total pressure. Equation B.8 shows the evaluation of the velocity components u and v with respect to the x and y directions, respectively.

$$\begin{aligned} u &= q\cos\upsilon \\ v &= q\sin\psi \end{aligned} \tag{B.8}$$

After calibration, the probe was mounted in the test section and set at a known yaw angle relative to the axial direction of the diffuser. At an inlet duct velocity of 15 m/s, the three pressures from the three tubes of the yaw meter were read, and the flow angle ψ and resultant velocity q determined using the calibration equations. While still at the same probe location, the probe was rotated until the null position was obtained. The flow angle was read off the yaw meter protractor and the flow velocity determined from the differential pressure measured between center tube which would now be measuring P_t and the averaged wall static pressures.

Using this procedure, the error introduced by using the calibration equations instead of the null-reading technique were established. This process

was repeated at several locations within the test section as shown in table B.1. The average error obtained in using the calibration charts as opposed to the null reading method in measuring the flow angle was 0.81°. This was acceptable considering that the resolution of the protractor was 1°. The rms error in velocity measurement was 1.37%.

Table B.1: Testing for the accuracy of the yaw meter probe

Location, y/W_1	Normalized velocity u/U_1		Flow direction $\upsilon°$	
	Equations	Null-reading	Equations	Null-reading
4.10	-25.68	-25.00	0.72	0.71
4.00	-25.29	-25.00	0.73	0.72
3.80	-26.00	-25.00	0.72	0.72
3.70	-25.81	-25.00	0.71	0.72
3.60	-25.10	-24.00	0.71	0.70
3.50	-25.61	-25.00	0.69	0.69
3.40	-25.35	-24.00	0.67	0.68
3.30	-24.90	-24.00	0.65	0.65
3.20	-24.65	-24.00	0.63	0.63
3.10	-24.39	-22.50	0.60	0.60
3.00	-23.61	-24.00	0.57	0.56

B.4 Constant temperature anemometer

Inlet velocity profiles and turbulence intensities were measured by use of a TSI constant temperature linearized anemometer (CTA) model 1054B. The sensor was a 5-micron platinum coated tungsten wire model 1212-T1.5. It was welded to a pair of L-shaped gold plated stainless steel needles that were mounted on a probe support. With this arrangement, the sensor was upstream of the probe, resulting in minimal flow disturbance by the probe

support. The probes were provided with a plug-type connector to fit into a probe support, thus providing an electrical connection to the anemometer electronics. The probe support was connected to the anemometer through a 1.9 m long tri-axial cable. The sensor was set to operate on a 5:1 bridge ratio with a control resistance of 64Ω. Figure B.6 shows the dimensions of the probe used. The probe support was 0.5 m long. The anemometer had a frequency response of up to 10 kHz. Based on the manufacturer's specification, the linearizer voltage output was accurate to within 0.5%.

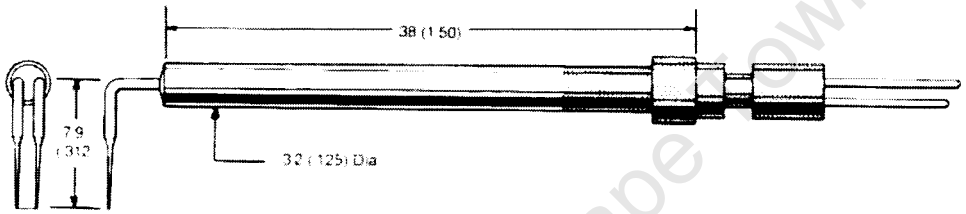

Figure B.6: The L-shaped hot-wire probe

The anemometer was calibrated in a low turbulence intensity (0.4%) calibration jet against a Pitot-static tube whose dynamic (differential) pressure was processed through the DP850V2P5 pressure transducer. Equation B.9 shows the linearized equation used for velocity measurements. Based on this equation, the calibration data was linear to within ±0.6%.

$$\tilde{u} = 3.2\tilde{E}_{\text{lin}} \tag{B.9}$$

where $\tilde{u}$ and $\tilde{E}_{lin}$ were the air instantaneous velocity and CTA linearizer outputs, respectively. The rms fluctuating velocity, u' was calculated according to Eq.B.10. Hence, the turbulence intensity could be established.

$$u' = \sqrt{\frac{1}{N}\sum_{i=1}^{N}\left(\tilde{u}_i - \frac{1}{N}\sum_{1}^{N}\tilde{u}_i\right)^2} \tag{B.10}$$

where N was the number of readings sampled at a frequency of 10 KHz for 3 seconds. Three sets of readings were taken in time steps of 10 seconds. The

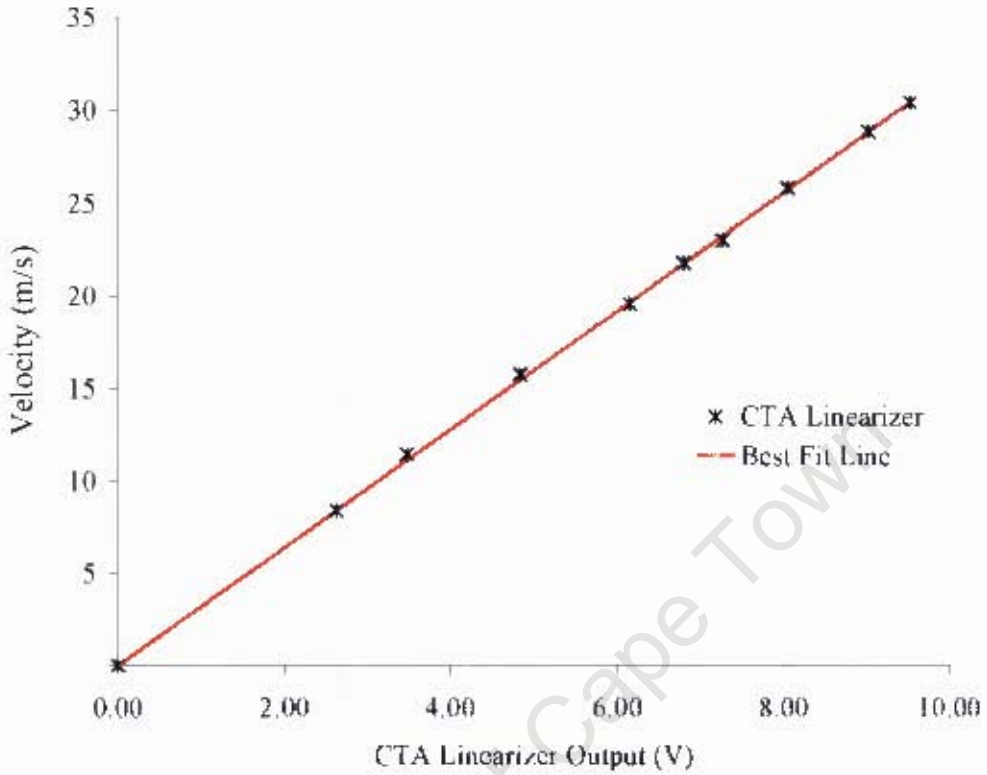

Figure B.7: CTA linearizer calibration curve

mean and the rms fluctuating velocities, and the turbulence intensities were then calculated from the resulting arrays before discarding the arrays ready for the next position.

The calibration was checked each time before any measurements were carried out. Figure B.7 shows the calibration curve used at all times during this study.

B.5 Data acquisition

The fundamental task of all measurement systems is the measurement and generation of real-world physical signals. Measurement devices help in acquiring and sometimes analyzing the measurements taken. Usually, the pri-

mary parameter measured is of no physical meaning until it is processed. Examples of such parameters are voltages and currents. Data acquisition enables the conversion of these physical signals into digital formats and their transfer into a computer and subsequent processing into their final physically meaningful form.

The voltage signals from the pressure transducer and CTA were digitized through an Eagle plug-in PCI 730 data acquisition board (DAQ). The board had a 32-bit PCI bus architecture which was PCI 2.2 compatible and with a 14-bit analogue input resolution. The board was powered at +5 Vdc at 1.3A. The analogue input range was set at ±5 V. The maximum sampling rate was 100 kHz with a maximum output absolute error of ±2 mV. The board had an internal IDC40 connector for digital I/O, through which the Scanivalve solenoid controller and O/E decoder were interfaced to the computer.

The board was supported by a powerful application program interface (EDRE) through which the physical instruments could be controlled from the National Instruments' LabVIEW software by creation of virtual instruments (VIs) to imitate the physical instruments. These VIs interfaced/translated information between a LabVIEW graphic user interface and the physical instruments via the PCI 730 board.

B.6 LabVIEW coding

National Instrument's LabVIEW is a software that is designed to communicate with computer hardware such as data acquisition, vision, and motion control devices and GPIB, PXI, VXI, RS-232, and RS-485 instruments. It is a graphical programming language that uses icons instead of lines of text to create applications. In contrast to text-based programming languages, where instructions determine program execution, LabVIEW uses dataflow

programming, where the flow of data determines execution.

LabVIEW programs are called virtual instruments, or VIs, because their appearance and operation imitate physical instruments. Every VI uses functions that manipulate input from a front panel and display that information or move it to other files or other computers. Virtual instrumentation can be used to create a complete and customized system for test, measurement, and industrial automation by combining different hardware and software components.

In this research, two VIs and five sub-VIs (equivalent to subroutines in line text programming) were created. Through these VIs, control, acquisition and processing of the voltage signals from the pressure transducer and CTA was done in accordance with the data flow logic shown in figure 3.10. The processed data was then saved to an Excel spreadsheet for further analysis.